University of South-Eastern Norway
Faculty of Technology, Natural Sciences and Maritime Sciences

Master's Thesis

Study programme: Master of Science in Micro and Nano Systems Technology

Autumn 2020

Fredrik Sommerfelt Grønvold

Optical Gyroscope Concept using Coupled Resonator Optical Waveguides: Simulation and Fabrication

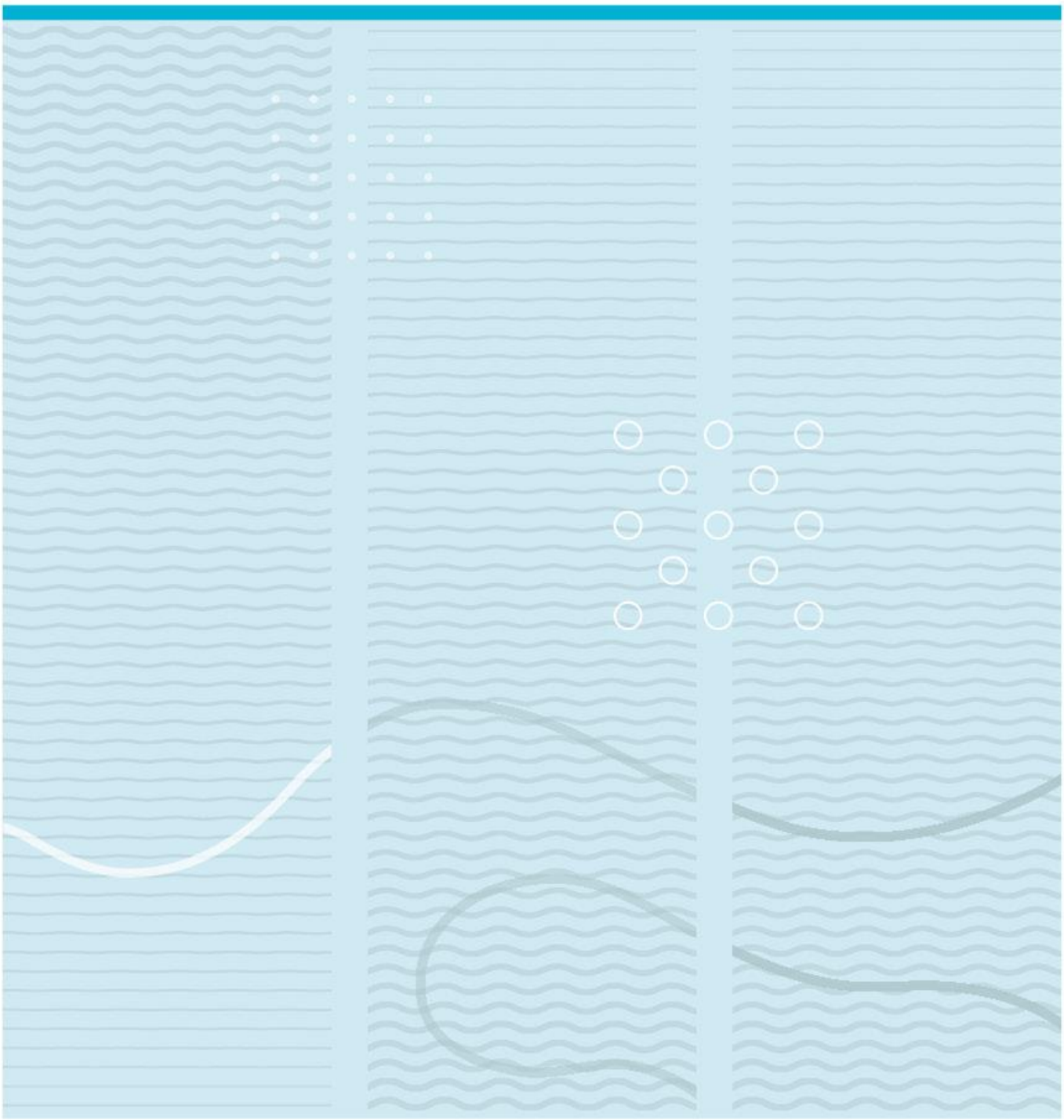

University of South-Eastern Norway
Faculty of Technology, Natural Sciences and Maritime Sciences
Department of Microsystems.
Raveien 215
NO-3184 Borre, Norway

http://www.usn.no

Summary

Coupled Resonator Optical Waveguides (CROW) have shown great potential as optical gyroscopes, achieving sensitivity of navigation grade performance. However, they are only superior to single ring resonators when the loss is small. In this thesis finite difference frequency domain (FDFD) computational tools for determining the propagation mode and constant were developed in MATLAB and expanded upon to include anisotropic materials. The methods show good relation to the literature and to other numerical methods like finite element modelling with COMSOL. The tools can still be developed further to increase accuracy and scope.

The fabrication of waveguides, resonators and CROW were done using a maskless photolithographic process with the PicoMaster 150PM laser writer. The process however, suffered from over-development and fabrication optimisation issues. Future work should either try to optimise the fabrication process or use other methods to fabricate the waveguides.

Preface

I would like to express my deepest gratitude to my supervisor Professor Muhammad Nadeem Akram. I am truly grateful to have been given the opportunity to work with him. I would also like to thank Professor Dag Werner Breiby from NTNU for his assistance and support with this thesis and I would like to extend my thanks and gratitude to the USN IMST Lab, the Department of Microsystems, the head engineers Thomas Martinsen and Thai Anh Tuan Ngyuyen, and researcher Pai Lu for their help with the practical aspects of this thesis. I would like to give an extra thanks to assistant professor Zekija for her patience, her invaluable help, and her guidance at the cleanroom laboratory. The fabrication in this thesis was conducted only in the month of October since the lab closed earlier this year due to COVID-19. To say that without her help the practical experiments in this thesis would not exist, is an understatement.

Finally, I would like to thank my family and friends who supported me through this endeavour.

Borre, 19.11.2020

Fredrik Sommerfelt Grønvold

Contents

1 Introduction

Today one will find gyroscopes everywhere, in mobile phones, cars, planes, ships etc. and they are an integral part of inertial navigation system (INS), guidance, and control systems for aircrafts, ships and vehicles [1], [2]. Optical gyroscopes have the significant advantage over other gyroscopes in that they are not affected by gravitational acceleration, have a low reaction time, with a high accuracy and reliability [1].

Optical gyroscopes are based on a relativistic phenomenon known as the Sagnac effect which was demonstrated by French physicist Georges Sagnac in 1913 [3]. The Sagnac effect is a phase difference between two counterpropagating beams induced by the rotation of the inertial space (see Figure 1-1) [3].

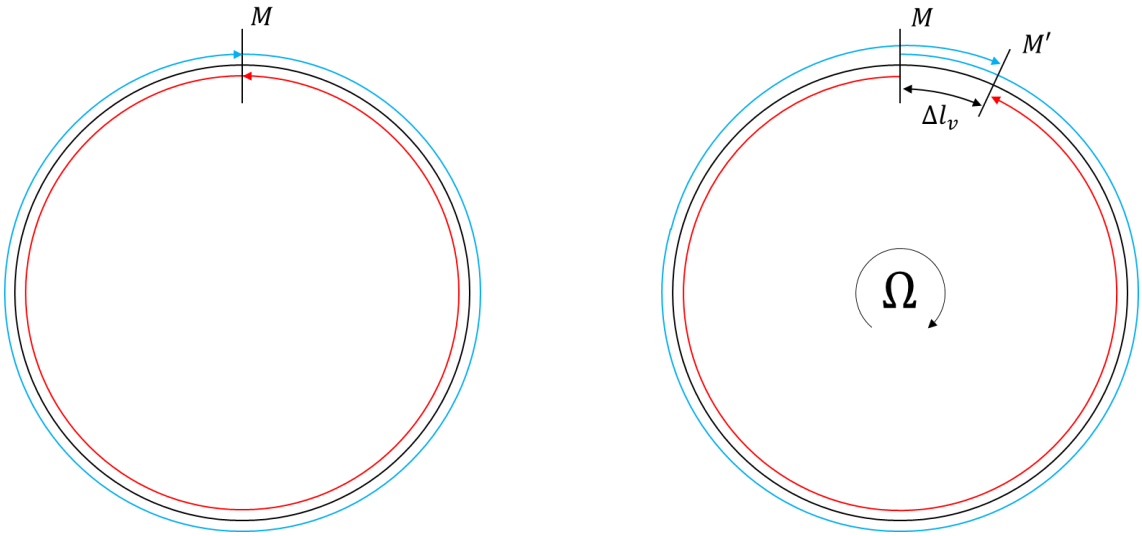

Figure 1-1: When rotation around the axis perpendicular to the plane of the propagation beams occur, the two counterpropagating beams experience different path lengths, inducing a phase shift.

The phase difference due to the Sagnac effect is given by:

$$\phi_S = \frac{4\pi\omega\Omega R^2}{c^2} \qquad (1\text{-}1)$$

Where ϕ_s is the phase shift, Ω is the angular rotation of the plane, ω is the angular frequency of the propagating beams, and R is the radius [3], [4]. The phase shift in (1-1) is dependent on the area enclosed by the path of the propagating beams.

Due to its relativistic nature, the Sagnac effect can also be interpreted as a frequency or doppler shift [3]. The Sagnac effect is not affected by the medium through which the beams propagate, as the Fizeau drag compensates for the effect of the refractive index [3].

The most common optical gyroscopes, the fibre optic gyroscope (FOG) and the ring laser gyroscope (RLG), exploit either the phase or the frequency interpretation of the Sagnac effect [1].

The FOG was introduced in 1976 by Vail and Shorthill and is considered a passive sensing system and can be divided into two types, the Interferometric FOG (IFOG) and the Resonant FOG [2]–[4]. The IFOG operates on sensing the phase shift generated by the Sagnac effect, while Resonant FOG (RFOG) operates with the frequency shift sensing method [5]. The phase sensing is based of measuring the power variation derived from the interference between the two counterpropagating beams in the fibre [5]. FOG with sensitivity of $0.01\ deg/h$ has been developed and sensitivity of $0.0003\ deg/h$ has been demonstrated [1]. FOG reach more than 50% of the tactical performance grade market and it is expected that they will overtake the RLGs in the future [2].

RLG was introduced in 1963 by Macek and Davis and considered to use an active sensing configuration [3], [4]. RLGs have the highest market share for high performance applications such as submarine navigation, which requires a bias stability between $0.0001 - 0.01\ °/h$ [2]. RLGs with sufficient sensitivity to measure the earth's rotation has been reported [2]. Nevertheless, RLGs have the issue of mode locking, where the counterpropagating beams couple together and oscillate at the same frequency, preventing the sensing of low rotation rates [3]. Methods to reduce the effect are for example mechanical ditcher and magneto-optics biasing [2].

Despite all their advantages, the RLG and the FOG have two major drawbacks, namely, their size and weight. RLGs can weight several kilograms and FOGs can use meters up to kilometres of optical fibre [4].

Although MEMS gyroscopes are widespread in handheld devices such as mobile phones and sensitivity has been improving over the years, MEMS gyroscopes still cannot satisfy the tactical grade requirements due to their bias stability of $5 - 30\ °/h$ [2].

This has opened up a field of research into integrated optical gyroscopes with micro photonic resonators. Integrated optics have the advantage that they can use the same

semiconductor fabrication process as MEMS, with a theoretical sensitivity exceeding that of MEMS [6]. However, unlike MEMS they do not have any moving parts and so the fabrication process is simplified [6]. One prominent integrated optical gyroscope is the Coupled Resonator Optical Waveguide (CROW) [5], [6]. CROW is a slow light device made up of an array of high-quality factor (Q) ring resonators coupled together through evanescent fields [4], [5]. Although CROW devices are usually phase sensing, the light propagation in the CROW has been used to develop frequency sensing gyroscopes [5]. In 2012, C. Sorrentino et al. were able to demonstrate a CROW gyroscope with inertial grade sensitivity by periodically modulating the coupling coefficient between the high Q resonators [4]. Nevertheless, it has been shown that CROW gyroscopes only offer superior sensitivity over a single resonator with equivalent area when the losses are small [6]. There are several sources of loss in an optical gyroscope configuration as seen in Figure 1-2**,** where are coupling losses between the waveguide and the laser or light source, there is intrinsic material loss, bending loss, and there is loss due to scattering from the surface roughness.

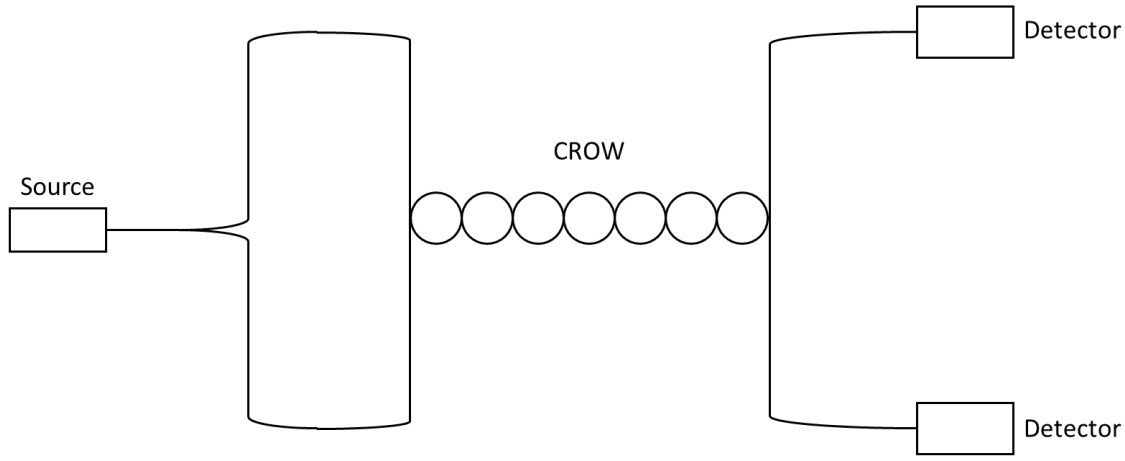

Figure 1-2: Simplified CROW gyroscope configuration.

2 Waveguide Theory

2.1 Waveguide principle

In its most fundamental form, a waveguide consists of a core and a cladding where the core has a higher refractive index than the cladding. This difference in refractive index allows for the confinement and propagation of electromagnetic waves.

When working with waveguides, it is common to express the electric and magnetic field in with the phasor expression.

Considering Maxwell's curl equations in phasor notation:

$$\nabla \times \vec{E} = -j\omega\mu\vec{H} \qquad (2\text{-}1)$$

$$\nabla \times \vec{H} = j\omega\varepsilon\vec{E} \qquad (2\text{-}2)$$

2.1.1 Planar Slab Waveguide

The planar slab waveguide is the simplest form of a waveguide and forms the basis for more complex waveguides [7], [8]. It consists of three dielectric layers as seen in Figure 2-1, where the slab is infinite in the $y - z$ plane and with different refractive index such that $n_f > n_s > n_c$.

In a slab waveguide the electric field has two possible polarisations, perpendicular to the $x - z$ plane in what is called a transverse electric (TE) polarisation, and parallel or in the $x - z$ plane in what is called transverse magnetic (TM) polarisation [8].

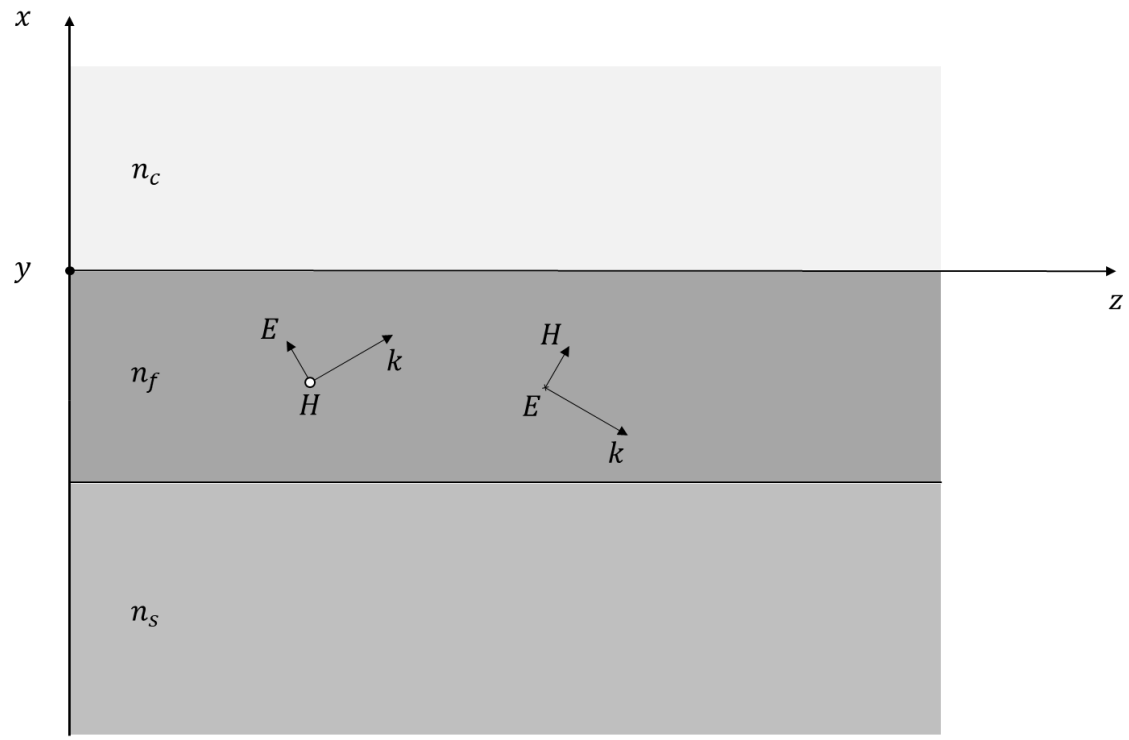

Figure 2-1: The slab waveguide consists of a cladding, film and substrate with different refractive index.

For the TE case, E_y is independent of y because the slab extends infinitely in the y direction. It is also assumed that there is no amplitude variation in the z direction. The electric field can then be expressed as

$$E_y(x,z) = E_y(x)e^{-j\beta z} \tag{2-3}$$

Where β is referred to as the longitudinal wavevector.

2.1.1.1 Mode and Field expression

Inserting (2-4) into the wave equation will yield the Helmholtz equation:

$$\frac{\partial^2 E_y}{\partial x^2} + (k_0^2 n_i^2 - \beta^2)E_y = 0 \tag{2-4}$$

Where n_i refers to the layer at which the electric field is in. Using the general s solution to the Helmholtz equation and applying the boundary conditions at the interfaces between the layer allows the TE field to be written as:

$$E_y(x) = \begin{cases} Ae^{-\gamma_c x} & 0 < x \\ A\left[cos(\kappa_f x) - \frac{\gamma_c}{\kappa_f} sin(\kappa_f x)\right] & -h < x < 0 \\ A\left[cos(\kappa_f h) + \frac{\gamma_c}{\kappa_f} sin(\kappa_f h)\right] e^{\gamma_s (x+h)} & x < -h \end{cases} \quad (2\text{-}5)$$

Where:

$$\gamma_i = \sqrt{\beta^2 - k_0 n_i} \quad (2\text{-}6)$$

$$\kappa = \sqrt{k_0 n_f - \beta^2} \quad (2\text{-}7)$$

κ is called the transverse wavevector and γ is the attenuation coefficient.

The longitudinal wavevector can be found graphically or numerically by solving the transcendental equation or the characteristic equation for the TE modes of a slab waveguide [8]:

$$\tan(h\kappa_f) = \frac{\gamma_c + \gamma_s}{\kappa_f \left(1 - \frac{\gamma_c \gamma_s}{\kappa_f^2}\right)} \quad (2\text{-}8)$$

The same approach for TM case results in the magnetic field can be plotted by:

$$H_y(x) = \begin{cases} Ae^{-\gamma_c \frac{n_f^2}{n_c^2} x} & 0 < x \\ A\left[cos(\kappa_f x) - \frac{n_f^2}{n_c^2} \frac{\gamma_c}{\kappa_f} sin(\kappa_f x)\right] & -h < x < 0 \\ A\left[cos(\kappa_f h) + \frac{n_f^2}{n_c^2} \frac{\gamma_c}{\kappa_f} sin(\kappa_f h)\right] e^{\gamma_s \frac{n_f^2}{n_s^2}(x+h)} & x < -h \end{cases} \quad (2\text{-}9)$$

The longitudinal wavevector for the TM case can be found by solving the transcendental equation:

$$\tan(h\kappa_f) = \frac{\kappa_f \left(\frac{n_f^2}{n_s^2}\gamma_s - \frac{n_f^2}{n_c^2}\gamma_c\right)}{\kappa_f^2 - \frac{n_f^2}{n_s^2 n_c^2}\gamma_c \gamma_s} \quad (2\text{-}10)$$

The mode number is characterised by how many nodes the field has within the oscillating region. The TE_0 mode has zero nodes, while the TE_1 mode has one node at the centre

of the waveguide (see Figure 2-2). Higher order modes contain less of their power inside the core and are more susceptible to bending loss [8].

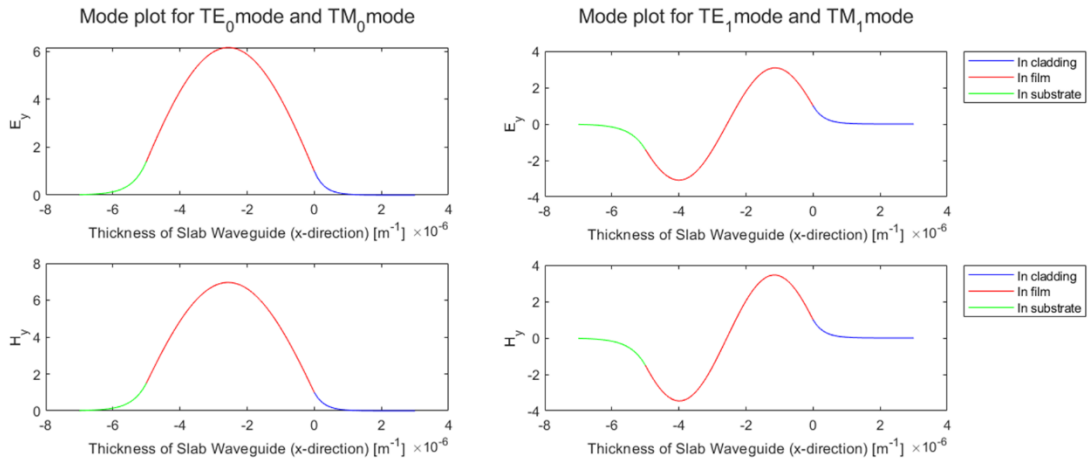

Figure 2-2: The field distribution of two first modes of a slab waveguide for the electric and magnetic field.

2.1.2 Optical Fibre

Optical fibres are circular or cylindrical waveguides and have revolutionized the communications industry [7]. There are two types of fibres, graded index and step index [8]. In a step index fibre, the refractive index profile sees a sudden step increase in the transition from cladding to the core of the fibre as seen in Figure 2-3.

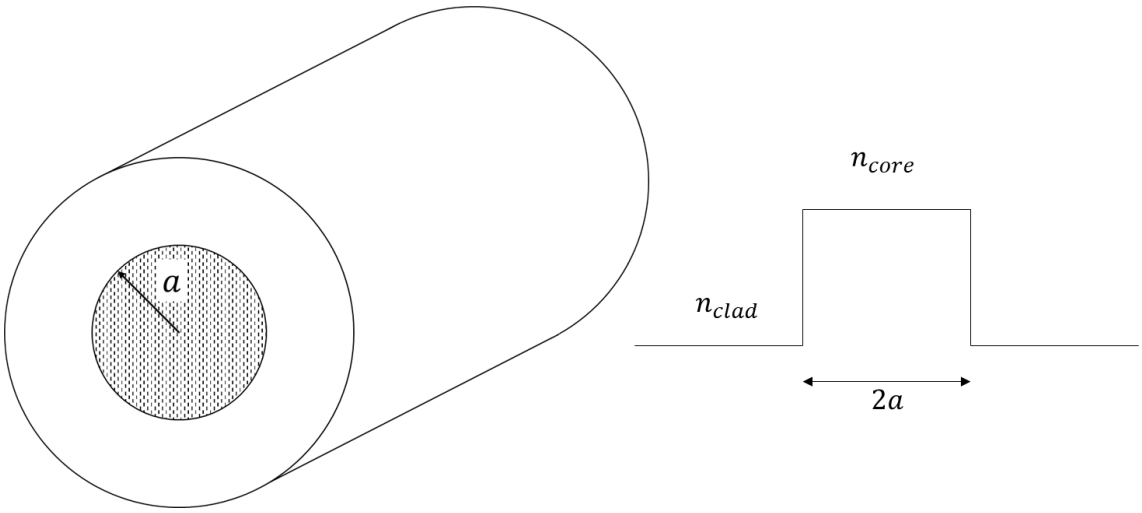

Figure 2-3: Cross-section of a step-index fibre and the refractive index profile.

Deriving the expression for the field distribution in the cylindrical coordinate system will result in the characteristic equation of the step-index fibre [8]:

$$\frac{\beta^2\nu^2}{a^2}\left[\frac{1}{\gamma^2}+\frac{1}{\kappa^2}\right]^2 = \left[\frac{J_\nu'(\kappa a)}{\kappa J_\nu(\kappa a)}+\frac{K_\nu'(\gamma a)}{\gamma K_\nu(\gamma a)}\right]\left[\frac{k_0^2 n_{core}^2 J_\nu'(\kappa a)}{\kappa J_\nu(\kappa a)}+\frac{k_0^2 n_{clad}^2 K_\nu'(\gamma a)}{\kappa K_\nu(\gamma a)}\right] \quad (2\text{-}11)$$

Where J_ν is a Bessel function of the first kind, $J_\nu'(\kappa a) = dJ_\nu(\kappa a)/d(\kappa a)$, K_ν is a modified Bessel function of the second kind, $K_\nu'(\kappa a) = dK_\nu(\kappa a)/d(\kappa a)$, ν is the angular mode number. The solutions to the characteristic equation are numbered with two indices, ν and m, where m is the radial mode number [8].

2.1.2.1 Weakly guiding approximation

If the difference in refractive index for the core and the cladding is very small, then one can use the weakly guiding approximation, also known as the scalar wave approximation [8], [9]. When using this approximation, then $n_{clad} \approx n_{core} = n$ and (2-11) is reduced to:

$$\frac{\beta^2\nu^2}{a^2}\left[\frac{1}{\gamma^2}+\frac{1}{\kappa^2}\right]^2 = \left[\frac{J_\nu'(\kappa a)}{\kappa J_\nu(\kappa a)}+\frac{K_\nu'(\gamma a)}{\gamma K_\nu(\gamma a)}\right]k_0^2 n^2 \quad (2\text{-}12)$$

With the use of some Bessel function identities, (2-12) can be simplified even further to [8]:

$$\kappa \frac{J_{j-1}(\kappa a)}{J_j(\kappa a)} = -\gamma \frac{K_{j-1}(\gamma a)}{K_j(\gamma a)} \tag{2-13}$$

The indices define the mode, with $j = 1$ being TE and TM modes, $j = \nu + 1$ being EH_ν modes, and $j = \nu - 1$ being HE_ν modes. EH and HE are hybrid modes, and HE_{11} is sometimes referred to as the fundamental mode [8]. "Fundamentals of Optoelectronics" by C. R. Pollock is suggested as further reading for a deeper study into modes for step-index fibres [8].

2.1.3 Ring Resonators

A ring resonator is a coupled waveguide with the important characteristic that it behaves as an optical filter, much like a Fabry-Perot resonator [7]. The light in the straight waveguide couples to the ring waveguide through evanescent fields. Considering the index profile of the coupling area in Figure 2-4, where n_w, w_w, n_r, and w_r is the refractive index and the width of the straight waveguide and the ring waveguide.

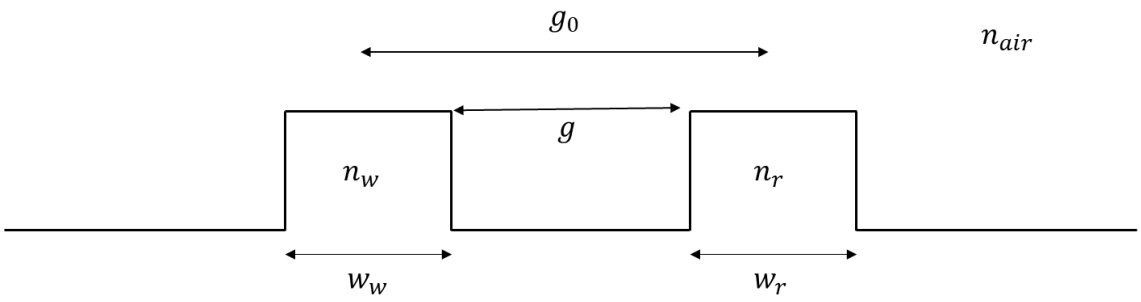

Figure 2-4: The refractive index profile of the coupling area between a straight and a ring waveguide.

The coupling factor between the straight and the ring waveguide is given by [7], [10]:

$$\kappa = \frac{\omega \varepsilon_0 \cos\left(\frac{k_{xr} w_r}{2}\right)}{2 P_w P_r (k_{xw}^2 + \alpha_r^2)} (n_w^2 - n_c^2) \sqrt{\frac{\pi R}{\alpha_r}} e^{\left[\alpha_r \left(\frac{w_r}{2} - g_0\right)\right]}$$
$$\times \left(\alpha_r \cos\left(\frac{k_{xw} w_w}{2}\right) \sinh\left(\frac{\alpha_r w_w}{2}\right) + k_{xw} \sin\left(\frac{k_{xw} w_w}{2}\right) \cosh\left(\frac{\alpha_r w_w}{2}\right)\right) \tag{2-14}$$

However, by using the same value for the following parameters:

$$w_w = w_r = w \tag{2-15}$$

$$n_w = n_r = n_{core} \tag{2-16}$$

Then the following variables can be simplified to:

$$P_w = P_r = \frac{n_{eff} k_0}{2\omega\mu_0}\left(\frac{w}{2} + \frac{1}{k_0\sqrt{n_{eff}^2 - n_{air}^2}}\right) \tag{2-17}$$

$$\alpha_{xw} = \alpha_{xr} = \alpha = k_0\sqrt{n_{eff}^2 - n_{air}^2} \tag{2-18}$$

$$k_{xw} = k_{xr} = k_x = k_0\sqrt{n_c^2 - n_{eff}^2} \tag{2-19}$$

This simplifies coupling equation can be to

$$\kappa = \frac{\omega\varepsilon_0 \cos\left(\frac{k_x w}{2}\right)}{2Pk_0^2}\sqrt{\frac{\pi R}{\alpha}}e^{\left[\alpha\left(-g-\frac{w}{2}\right)\right]} \times\left(\alpha\cos\left(\frac{k_x w}{2}\right)\sinh\left(\frac{\alpha w}{2}\right) + k_x\sin\left(\frac{k_x w}{2}\right)\cosh\left(\frac{\alpha w}{2}\right)\right) \tag{2-20}$$

When the circumference of the ring is an integer multiple of the wavelength inside the waveguide to the light passing though the straight waveguide, then the light coupled into the ring starts to resonate and the stored power builds up [11]. Resonance condition for a micro-ring resonator is:

$$n_{eff} 2\pi R = m\lambda_i \tag{2-21}$$

Where n_{eff} is the effective refractive index of the mode of the ring waveguide, R is radius from the centre of the ring to the centre of the waveguide, λ_i is the resonating wavelength, and m is an integer. For a 2D analysis, the n_{eff} is the effective index of the slab waveguide.

When the ring waveguide is resonant, some of the light in the ring couples back to the straight waveguide causing interference. At resonance and critical coupling, the interference is completely destructive and the transmission through the straight waveguide becomes zero [11].

Although ring waveguides are inherently lossy, in practice the losses are usually dominated by scattering from the roughness of the sidewalls [7].

2.2 Boundary conditions

When operating with electromagnetic fields and waves, boundary conditions are very important. This thesis will primarily work with two types of boundary conditions, zero-boundary and Perfectly matched layers (PML). The zero-boundary condition states that the electric and/or magnetic field is zero at the boundary. PML was first introduced by Berenger in 1993 and primarily used to simulate absorbing boundaries without reflecting the electromagnetic waves [12]. This comes in useful when evaluating the leakage loss of a propagating mode [13].

3 Thesis Objective

As stated by D. Kalantarov and C. P. Search, the CROW gyroscope is only superior to a single ring resonator of equal area if the losses in the CROW are low. Thus, for fabricating waveguides for CROW gyroscopes, it is important to know the propagation mode, propagation constant and loss of the waveguide. Single mode operation in CROWs is preferable for two reasons. Firstly, the higher order modes are more susceptible to bending loss since they retain less of their power inside the core than the fundamental mode. Secondly, the resonance response is of a single mode is easier predict, as the resonance from higher modes do not interfere with the response.

This thesis is therefore concerned with the computation of waveguide modes, simulation of ring resonance response, and the fabrication of CROWs. Computation methods such as finite difference frequency domain (FDFD) and finite element method (FEM) will be utilised in the computation and simulation of optical waveguides.

4 Methods

This thesis consists of two main parts. The first part concerns the mode solving of waveguides using simulation tools such as COMSOL Multiphysics and MATLAB. The second part shows the fabrication of waveguides, ring resonators and CROWS.

4.1 Simulation Methods

Two simulation methods were used for solving the mode and for plotting the magnetic and electric field. The first was a mode analysis using finite element modelling (FEM) with COMSOL Multiphysics. The other method was a finite difference frequency domain (FDFD) method, done by solving an eigenvalue equation, for which three types of MATLAB scripts were created. All simulations were done on an Acer Swift 3 with an 8th Gen Intel Core 5i processor running Windows 10 64 bit.

4.1.1 COMSOL

COMSOL Multiphysics is a FEM simulation tool and was used both as a simulation tool and as a reference tool when developing MATLAB scripts. Cross-sectional structures such as microstructure optical fibres (MOF), holey fibres etc. were solved by creating individual 2D COMSOL models using the RF module or with the Wave Optics module.

COMSOL was also used to simulate the wavelength response of a ring resonator using the Wave Optics module including the beam envelop method by modifying the ring resonator tutorial from COMSOL [11]. The ring resonator had a radius of $50\ \mu m$, a gap between the straight and ring waveguide of $300\ nm$, a waveguide width of $450\ nm$. The $n_{core} = 3.42$ and the $n_{clad} = 3$.

4.1.1.1 Mode Solver Application

To streamline the reference process for MATLAB simulations a COMSOL application was created using the Application Builder. The mode solver application was made so as to allow the user to choose between four fundamental waveguide cross-sections, and also to define the geometrical, physical and simulation parameters, as seen in Figure 4-1. The application then computed and plotted the absolute value of the x, y and z components of the electric and magnetic fields, provided the effective refractive index (n_{eff}), the

propagation constant, and the attenuation constant. The user could switch between field plots for the different n_{eff} using a drop-down menu.

The advantages of using a COMSOL application are that it can be used on a computer without COMSOL Multiphysics, and the simulation process is faster than having to create a new simulation model.

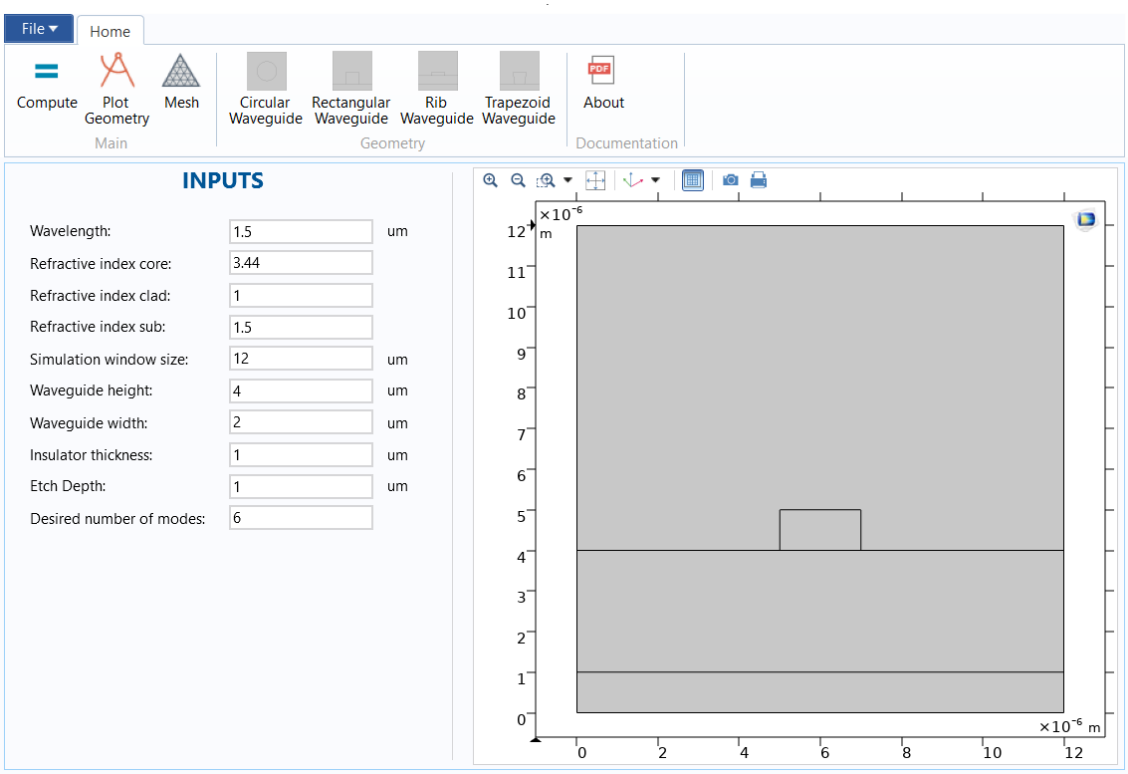

Figure 4-1: The main dashboard of the COMSOL application where the user can specify the parameters of the waveguide cross-section.

4.1.2 MATLAB

The first two self-developed MATLAB scripts were based on Z. Zhu and T. G. Brown's paper "Full-vectorial finite-difference analysis of microstructured optical fibers" [14], and the paper by S. Guo et al. "Loss and dispersion analysis of microstructured fibers by finite difference method" respectively [13]. The first script was a vectoral mode solver with a zero-boundary condition (VMS-ZB), while the second script was a vectoral mode solver with a PML boundary (VMS-PML). The third script built upon the two other scripts by introducing material anisotropy. The three scripts can be found in Appendix 2, Appendix 3, and Appendix 4.

4.1.2.1 Vectoral Mode Solver with a Zero-boundary Condition (VMS-ZB)

The FDFD method proposed by Z. Zhu and T. G. Brown propose uses a two dimensional Yee mesh with the introduction of index averaging [14].

First, Maxwell's equations were considered in their phasor notation after normalising the electric field with the impedance of free space (Z_0):

$$\nabla \times E = -jk_0 H \tag{4-1}$$

$$\nabla \times H = -jk_0 \varepsilon E \tag{4-2}$$

Splitting the electric and the magnetic field into their respective x, y and z components and with the Yee mesh discretization, the field components can be written as:

$$ik_0 H_x = \frac{E_z(j, l+1) - E_z(j, l)}{\Delta y} - i\beta I E_y \tag{4-3}$$

$$ik_0 H_y = i\beta I E_x - \frac{E_z(j+1, l) - E_z(j, l)}{\Delta x} \tag{4-4}$$

$$ik_0 H_z = \frac{E_y(j+1, l) - E_y(j, l)}{\Delta x} - \frac{E_x(j, l+1) - E_x(j, l)}{\Delta y} \tag{4-5}$$

$$-ik_0 \varepsilon_{rx} E_x = \frac{H_z(j, l) - H_z(j, l-1)}{\Delta y} - i\beta I H_y \tag{4-6}$$

$$-ik_0 \varepsilon_{ry} E_y = i\beta I H_x - \frac{H_z(j, l) - H_z(j-1, l)}{\Delta x} \tag{4-7}$$

$$-ik_0 \varepsilon_{rz} E_z = \frac{H_y(j, l) - H_y(j-1, l)}{\Delta x} - \frac{H_x(j, l) - H_x(j, l-1)}{\Delta y} \tag{4-8}$$

These can be expressed as the following matrix equations:

$$-jk_0 \begin{bmatrix} \varepsilon_{rx} & 0 & 0 \\ 0 & \varepsilon_{ry} & 0 \\ 0 & 0 & \varepsilon_{rz} \end{bmatrix} \begin{bmatrix} E_x \\ E_y \\ E_z \end{bmatrix} = \begin{bmatrix} 0 & -j\beta I & V_y \\ j\beta I & 0 & -V_x \\ -V_y & V_x & 0 \end{bmatrix} \begin{bmatrix} H_x \\ H_y \\ H_z \end{bmatrix} \tag{4-9}$$

$$jk_0 \begin{bmatrix} H_x \\ H_y \\ H_z \end{bmatrix} = \begin{bmatrix} 0 & -j\beta I & U_y \\ j\beta I & 0 & -U_x \\ -U_y & U_x & 0 \end{bmatrix} \begin{bmatrix} E_x \\ E_y \\ E_z \end{bmatrix} \tag{4-10}$$

Where:

$$U_x = \frac{1}{\Delta x}\begin{bmatrix} -1 & 1 & & & & \\ & -1 & 1 & & & \\ & & \ddots & \ddots & & \\ & & & \ddots & 1 & \\ & & & & -1 & 1 \\ & & & & & -1 \end{bmatrix}, U_y = \frac{1}{\Delta y}\begin{bmatrix} -1 & & & 1 & & \\ & -1 & & & \ddots & \\ & & \ddots & & & 1 \\ & & & \ddots & & \\ & & & & -1 & \\ & & & & & -1 \end{bmatrix}$$

$$V_x = \frac{1}{\Delta x}\begin{bmatrix} 1 & & & & & \\ -1 & 1 & & & & \\ & -1 & \ddots & & & \\ & & \ddots & \ddots & & \\ & & & -1 & 1 & \\ & & & & -1 & 1 \end{bmatrix}, V_y = \frac{1}{\Delta y}\begin{bmatrix} 1 & & & & \\ & 1 & & & \\ & & \ddots & & \\ -1 & & & \ddots & \\ & \ddots & & & 1 \\ & & -1 & & \end{bmatrix}$$

The index averaging is done by averaging the dielectric constant:

$$\varepsilon_{rx}(j,l) = \frac{\varepsilon_r(j,l) + \varepsilon_r(j,l-1)}{2} \qquad \textit{(4-11)}$$

$$\varepsilon_{ry}(j,l) = \frac{\varepsilon_r(j,l) + \varepsilon_r(j-1,l)}{2} \qquad \textit{(4-12)}$$

$$\varepsilon_{rz}(j,l) = \frac{\varepsilon_r(j,l) + \varepsilon_r(j-1,l-1) + \varepsilon_r(j,l-1) + \varepsilon_r(j-1,l)}{4} \qquad \textit{(4-13)}$$

Solving the matrix equations for either E_z or H_z results in eigenvalue equations (4-14) and (4-15).

$$P\begin{bmatrix} E_x \\ E_y \end{bmatrix} = \beta^2 \begin{bmatrix} E_x \\ E_y \end{bmatrix} \qquad \textit{(4-14)}$$

$$Q\begin{bmatrix} H_x \\ H_y \end{bmatrix} = \beta^2 \begin{bmatrix} H_x \\ H_y \end{bmatrix} \qquad \textit{(4-15)}$$

Where both P and Q are made up of the sub-matrix sets $\{P_{xx}, P_{xy}, P_{yx}, P_{yy}\}$ and $\{Q_{xx}, Q_{xy}, Q_{yx}, Q_{yy}\}$, it is only necessary to solve one of the eigenvalue equations. The MATLAB script uses the Q matrix.

$$Q_{xx} = -k_0^{-2} V_x U_y U_x \varepsilon_{rz}^{-1} V_y + \left(\varepsilon_{ry} + k_0^{-2} V_x U_x\right)\left(k_0^2 I + U_y \varepsilon_{rz}^{-1} V_y\right) \quad (4\text{-}16)$$

$$Q_{yy} = -k_0^{-2} V_y U_x U_y \varepsilon_{rz}^{-1} V_x + \left(\varepsilon_{rx} + k_0^{-2} V_y U_y\right)(k_0^2 I + U_x \varepsilon_{rz}^{-1} V_x) \quad (4\text{-}17)$$

$$Q_{xy} = -\left(\varepsilon_{ry} + k_0^{-2} V_x U_x\right) U_y \varepsilon_{rz}^{-1} V_x + k_0^{-2} V_x U_y (k_0^2 I + U_x \varepsilon_{rz}^{-1} V_x) \quad (4\text{-}18)$$

$$Q_{yx} = -\left(\varepsilon_{rx} + k_0^{-2} V_y U_y\right) U_x \varepsilon_{rz}^{-1} V_y + k_0^{-2} V_y U_x \left(k_0^2 I + U_y \varepsilon_{rz}^{-1} V_y\right) \quad (4\text{-}19)$$

Solving the eigenvalue equation gives the H_x and the H_y field components. The remaining H_z component can be found from the divergence equation as:

$$H_z = \frac{k_0^2 I + \left(U_x \varepsilon_{ry}^{-1} V_x + U_y \varepsilon_{rx}^{-1} V_y\right)}{j\beta\left(U_x \varepsilon_{ry} H_x + U_y \varepsilon_{rx} H_y\right)} \quad (4\text{-}20)$$

The electric field components are determined by Maxwell's equations.

4.1.2.2 Vectoral Mode Solver with Perfectly Matched Layers (VMS-PML)

The previous script was using a zero-boundary condition and must be modified to simulate absorbing boundaries. Authors Guo et al. use the same approach as Z. Zhu and T. G. Brown [13], [14]. However, to simulate the PML region of the computation window, Guo et al. introduces the PML s parameter [13].

$$s = \begin{bmatrix} \frac{s_y}{s_x} & 0 & 0 \\ 0 & \frac{s_x}{s_y} & 0 \\ 0 & 0 & s_x s_y \end{bmatrix} \quad (4\text{-}21)$$

Where,

$$s_x = 1 - \frac{\sigma_x}{j\omega\varepsilon_0} \quad (4\text{-}22)$$

$$s_y = 1 - \frac{\sigma_y}{j\omega\varepsilon_0} \tag{4-23}$$

The conductivity profile is give as [15]:

$$\sigma_e(\rho) = \sigma_{max}\left(\frac{\rho}{d}\right)^m \tag{4-24}$$

Where d is the thickness of the PML region, m is the power law of the conductivity profile, and ρ is the distance from the outer boundary of the PML. The maximum conductivity is related to R, which is the theoretical reflection coefficient, through [15]:

$$\sigma_{max} = \frac{(m+1)\varepsilon_0 cn}{2d}\ln\frac{1}{R} \tag{4-25}$$

Then the conductivity profile is:

$$\sigma = \frac{(m+1)\varepsilon_0 cn\rho^m}{2d^{m+1}}\ln\frac{1}{R} \tag{4-26}$$

In most cases the theoretical reflection coefficient should be very small. For the MATLAB script the value was adopted from C. -P. Yu and H. -C. Chang to be $R = 10^{-8}$ [15].
The introduction of the PML changes (4-9) and (4-10) to:

$$-jk_0\begin{bmatrix}\varepsilon'_{rx} & 0 & 0\\ 0 & \varepsilon'_{ry} & 0\\ 0 & 0 & \varepsilon'_{rz}\end{bmatrix}\begin{bmatrix}E_x\\E_y\\E_z\end{bmatrix} = \begin{bmatrix}0 & -j\beta I & V_y\\ j\beta I & 0 & -V_x\\ -V_y & V_x & 0\end{bmatrix}\begin{bmatrix}H_x\\H_y\\H_z\end{bmatrix} \tag{4-27}$$

$$jk_0\begin{bmatrix}\mu'_{rx} & 0 & 0\\ 0 & \mu'_{ry} & 0\\ 0 & 0 & \mu'_{rz}\end{bmatrix}\begin{bmatrix}H_x\\H_y\\H_z\end{bmatrix} = \begin{bmatrix}0 & -j\beta I & U_y\\ j\beta I & 0 & -U_x\\ -U_y & U_x & 0\end{bmatrix}\begin{bmatrix}E_x\\E_y\\E_z\end{bmatrix} \tag{4-28}$$

Where:

$$\varepsilon'_{rx} = \frac{s_y}{s_x}\varepsilon_{rx} \tag{4-29}$$

$$\varepsilon'_{ry} = \frac{s_x}{s_y}\varepsilon_{ry} \tag{4-30}$$

$$\varepsilon'_{rz} = s_y s_x \varepsilon_{rz} \tag{4-31}$$

$$\mu'_{rx} = \frac{s_y}{s_x}\mu_{rx} \tag{4-32}$$

$$\mu'_{ry} = \frac{s_x}{s_y}\mu_{ry} \tag{4-33}$$

$$\mu'_{rz} = s_y s_x \mu_{rz} \tag{4-34}$$

This results in the sub-matrices for the Q matrix changing to:

$$\begin{aligned} Q_{xx} = {} & \varepsilon'_{ry} U_y \varepsilon'^{-1}_{rz} V_y + V_x \mu'^{-1}_{rz} U_x \mu'_{rx} + k_0^2 \varepsilon'_{ry} \mu'_{rx} \\ & + k_0^{-2} V_x \mu'^{-1}_{rz} \{U_x U_y - U_y U_x\} \varepsilon'^{-1}_{rz} V_y \end{aligned} \tag{4-35}$$

$$\begin{aligned} Q_{yy} = {} & \varepsilon'_{rx} U_x \varepsilon'^{-1}_{rz} V_x + V_y \mu'^{-1}_{rz} U_y \mu'_{ry} + k_0^2 \varepsilon'_{rx} \mu'_{ry} \\ & + k_0^{-2} V_y \mu'^{-1}_{rz} \{U_y U_x - U_x U_y\} \varepsilon'^{-1}_{rz} V_x \end{aligned} \tag{4-36}$$

$$\begin{aligned} Q_{xy} = {} & -\varepsilon'_{ry} U_y \varepsilon'^{-1}_{rz} V_x + V_x \mu'^{-1}_{rz} U_y \mu'_{ry} \\ & + k_0^{-2} V_x \mu'^{-1}_{rz} \{U_y U_x - U_x U_y\} \varepsilon'^{-1}_{rz} V_x \end{aligned} \tag{4-37}$$

$$\begin{aligned} Q_{yx} = {} & -\varepsilon'_{rx} U_x \varepsilon'^{-1}_{rz} V_y + V_y \mu'^{-1}_{rz} U_x \mu'_{rx} \\ & + k_0^{-2} V_y \mu'^{-1}_{rz} \{U_x U_y - U_y U_x\} \varepsilon'^{-1}_{rz} V_y \end{aligned} \tag{4-38}$$

4.1.2.3 Vectoral Mode Solver with Anisotropic Waveguide Material

Due to the stresses induced in the wafer from material deposition, the dielectric constant may not be entirely uniform for the x, y and z direction. Building upon the previous mode solver MATLAB scripts, a new script was created with an induced anisotropic behaviour because of a mismatch between the y component and the x and z component of the dielectric constant. By expressing the dielectric value as a function of position, this script can also be used to simulate graded index fibres [8].

This script was then compared to a COMSOL model of the step-index fibre described 4.1.2.4.1 with components of the dielectric constant being defined in the settings for the wave equation node. The ratio of the x, y and the z component of the dielectric constant for a material and its dielectric constant used for this analysis can be found in Table 4-1.

Table 4-1: Ratio of the x, y and z components of the dielectric constant and the dielectric constant.

DIELECTRIC COMPONENT	RELATIVE VALUE
$\varepsilon_{rx}/\varepsilon_r$	1
$\varepsilon_{ry}/\varepsilon_r$	0.98
$\varepsilon_{rz}/\varepsilon_r$	1

4.1.2.4 Comparison

The first two scripts were then used to solve for waveguides described in the literature and compared to their findings as well as to the solution from the COMSOL Mode Solver application.

4.1.2.4.1 "Analysis of Vectoral Mode Fields in Optical Waveguides by a New Finite Difference Method" by P. Lüsse et al. [16]

In 1994, P. Lüsse et al. published a paper in which they present a numerical method for finding mode for optical waveguides [16]. To illustrate the accuracy of their numerical model, P. Lüsse et al. compared their results with the analytical solution of a high-index difference step-index optical fibre. The fibre had a core refractive index of $n_{core} = 3.41477$, a cladding refractive index of $n_{clad} = 3.16589$, a radius of $4.5\ \mu m$, and a wavelength of $\lambda = 1.3\ \mu m$ [16]. Using a computational window $20\ \mu m \times 20\ \mu m$ in size with a decreasing mesh size towards the centre where the smallest value was $0.071\ \mu m$. Lüsse et al. were able to get an effective index of $n_{eff} = 3.4130918$ [16].

Building on this they proceeded to analyse the rib waveguide, shown in Figure 4-2, with a wavelength of $\lambda = 1.55\ \mu m$. Using a computational window of $8\ \mu m \times 6\ \mu m$ with a smallest mesh size of $0.013\ \mu m$, P. Lüsse et al. got an effective refractive index of $n_{eff} = 3.388687$ [16].

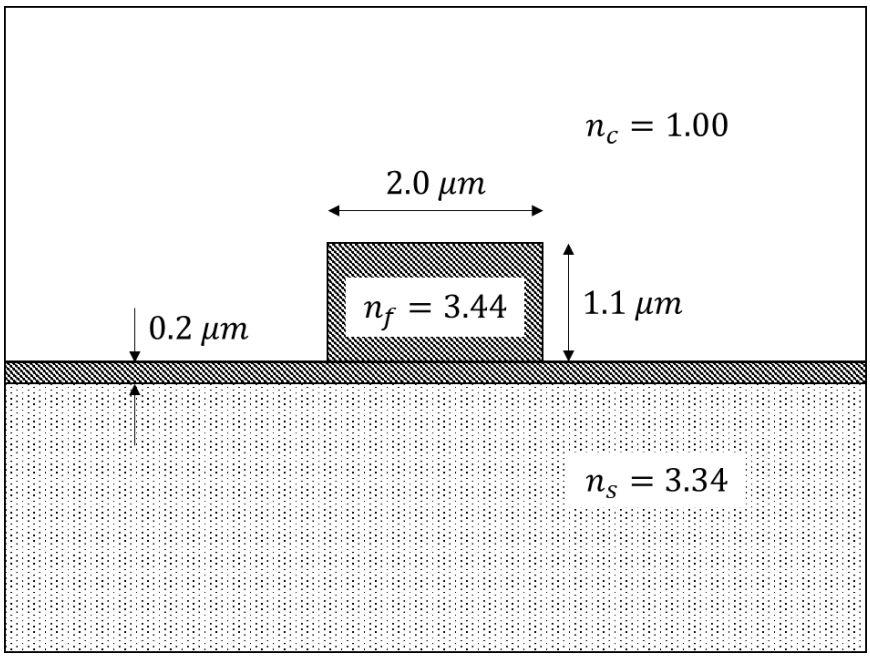

Figure 4-2: Rib waveguide analysed by Lüsse et al. [16].

These two waveguides were analysed using the VMS-ZB MATLAB script and the COMSOL Mode Solver application. For step-index fibre, the MATLAB script had a uniform mesh size of $0.067\mu m$, while COMSOL used a physics-controlled mesh with a mesh size of "Extremely fine". Care was taken to have a symmetrical mesh in the four quarters of the cross-section.

For the rib waveguide, the MATLAB script used a computation window of $5\ \mu m \times 5\ \mu m$, with a uniform mesh size of $0.0167\ \mu m$. The COMSOL model kept the same computational window as Lüsse et al. with an "Extremely fine" physics-controlled mesh.

4.1.2.4.2 "Full-vectoral finite-difference analysis of microstructured optical fibres" by Z. Zhu and T. G. Brown

In the paper by Z. Zhu and T. G. Brown, upon which the VMS MATLAB script is based, the analysis method was used on a step-index fibre and compared with results using the method proposed by P. Lüsse et al. and Huang et al. This step-index fibre had a radius of $3\ \mu m$ with a core refractive index of $n_{core} = 1.45$, an air cladding refractive index of $n_{clad} = 1$, and a wavelength of $1.5\ \mu m$ [14]. Because of the symmetrical properties of the optical fibre, they only computed the first quarter of the cross-section with a computation window of $6\ \mu m \times 6\ \mu m$ and applied a magnetic wall to the left boundary,

an electric wall to the bottom boundary and a zero boundary condition to the remaining boundaries of the computation window [14]. Using a mesh of 120 grids along the x-axis, they get an effective refractive index of $n_{eff} = 1.438613$ [14].

Having analysed the step fibre, they applied the method on a MOF, specifically an air-hole-assisted optical fibre (AHAOF) as seen in Figure 4-3. The medium of the fibre was made up of silica with a refractive index of $n_{clad} = 1.42$, a core of silicon with radius $r_0 = 2\ \mu m$ and a refractive index of $n_{core} = 1.45$. Surrounding the core were air holes spaced with regular $5\ \mu m$ intervals between the centre of each hole with an radius of $r_a = 2\ \mu m$ and a refractive index $n_{air} = 1$ [14].

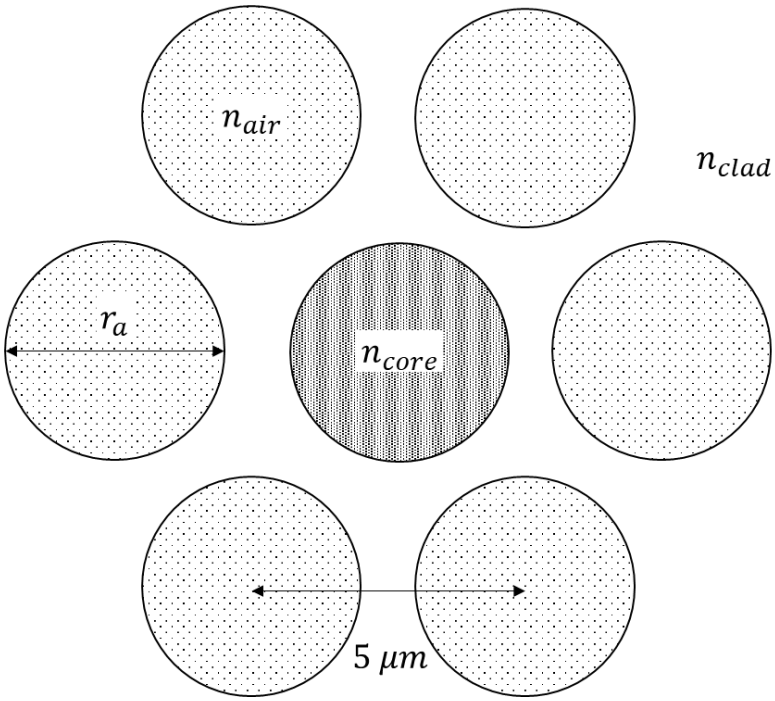

Figure 4-3: MOF analysed by Z. Zhu and T. G. Brown [14].

As with the step-index fibre they only analysed the first quarter of the waveguide cross-section with a computation window of $8\ \mu m \times 8\ \mu m$ and applied a magnetic wall to the left boundary and an electric wall to the remaining boundaries [14]. Using the same number of grids along the x-axis they obtained an effective refractive index of $n_{eff} = 1.4353602$ [14].

When analysing these two waveguides with the VMS MATLAB script, the entire cross-section was analysed with a zero-boundary condition and a uniform mesh of 300 grids along the x-axis. The same approach was used with COMSOL in terms of computation

window with an “Extremely fine” mesh; however, the boundary was defined by default as a PEC. As with the step-index waveguide from P. Lüsse et al., care was taken to keep the mesh symmetrical in the four quarters of the waveguide cross-section.

4.1.2.4.3 “Loss and dispersion analysis of microstructured fibers by finite-difference method” by S. Guo et al.

S. Guo et al. base their FDFD model on the one proposed by Z. Zhu and T. G. Brown, however they modified the model by introducing a PML layer on the boundary [13]. They tested their new method on a photonic crystal fibre (PCF) made of glass with a radial ring of six air holes [13]. The air holes had a radius of $2.5\ \mu m$ and were spaced out by $6.75\ \mu m$ as seen in Figure 4-4. The PCF was analysed at a wavelength of $1.45\ \mu m$, with the refractive index of glass at $n_{clad} = 1.45$. Comparing their results to the multipole method, they proceeded to improve the index averaging with the introduction of a sub-cell mesh [13]. Just like Z. Zhu and T. G. Brown, S. Guo et al. took advantage of the symmetrical properties of the PCF and only computed the first quadrant. They did so by applying a PEC to the left boundary, a PMC to the bottom boundary and a PML layer with a zero-boundary on the remaining two sides of the $10.125\ \mu m \times 10.125\ \mu m$ computation window [13]. The PML layer thickness was 10% of the computation window and had a second-order power law profile [13].

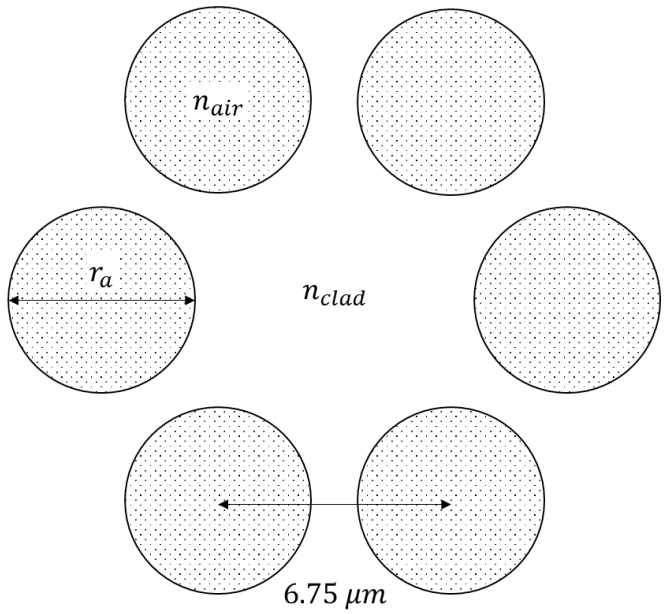

Figure 4-4: PCF analysed by S. Guo et al. [13].

4.2 Design and Fabrication

The waveguides were fabricated using a photolithographic process. A general process procedure can be found in Appendix 1. A complete list of the tools and their model, as used in the fabrication process can be found in Table 4-2, and a list of the chemicals used and their function can be found in Table 4-3. Throughout the fabrication process, the structures were inspected under a Nikon optical microscope. This microscope was not connected to a computer and so no photos were taken from these inspections.

Table 4-2: List of tools and model used in the fabrication process.

TOOL	MODEL
SPIN COATER	SPIN150
PROFILOMETER	DEKTAK 150
MASKLESS ALIGNER	PicoMaster 150PM
DEEP REACTIVE ION ETCHER	PlasmaPro 100 Estrelas
OPTICAL MICROSCOPE	Nikon
UV EXPOSURE	Honle UV technologies UVaCube 100
ULTRASOUND BATH	-

Table 4-3: List of chemicals and their use/property used in the fabrication process.

CHEMICAL	USE/PROPERTY
ACETONE	Wafer cleaning
ISOPROPANOL	Wafer cleaning
S1813	Positive photoresist
MF-319	Photoresist developer
EC SOLVENT	Photoresist solvent

4.2.1.1 PicoMaster PM150 Laser Writer

The photoresist was exposed with the PicoMaster PM150 laser writer, manufactured by 4PICO. Its primary components were the writing module, the step axis and the scan axis as seen in Figure 4-5.

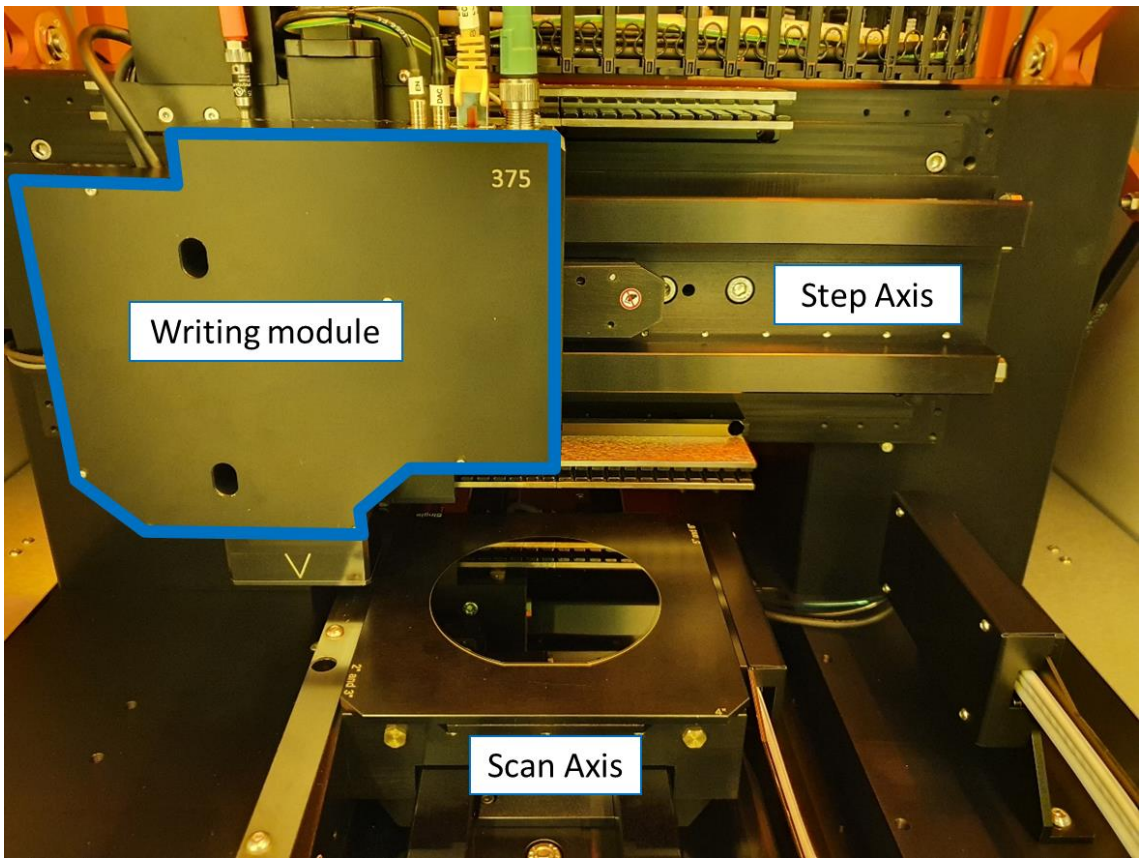

Figure 4-5: The writing module of the PicoMaster and its primary components.

The writing module had a red laser and a blue laser. While the red laser was used to focus the writing module, the blue laser was the one exposing the photoresist and it had three different spot sizes, each with their own depth of focus as seen in Table 4-4.

Table 4-4: Spot size and the corresponding depth of field for the PicoMaster.

RESOLUTION	SPOT SIZE	DEPTH OF FOCUS
HIGH	$280\ nm$	$300\ nn$
MEDIUM	$450\ nm$	$880\ nm$
LOW	$880\ nm$	$2400\ nm$

The laser writer scanned across the wafer as shown in Figure 4-6. It is recommended by 4PICO that the step size on the step axis should be at least 50% of the spot size for optimal performance. The scanning speed, together with the exposure energy, influences the intensity of the laser spot.

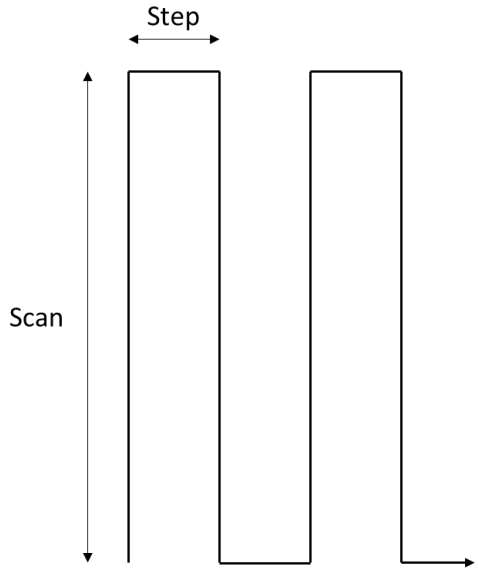

Figure 4-6: The writing movement of the laser across the substrate surface.

4.2.2 Mask Designs

Three mask types of mask designs were made, the straight waveguide, the ring resonator, and the CROW design. The mask designs were created using L-Edit IC v2018 and exported as GDSII files before being loaded on the PicoMaster.

4.2.2.1 Straight Waveguides

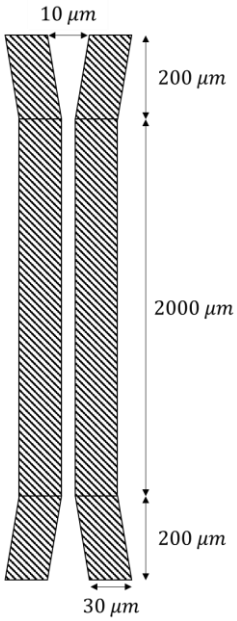

The mask design for the straight waveguide can be seen in Figure 4-7. On either end of the waveguide is a taper that widens out to $10\ \mu m$ over a distance of $200\ \mu m$. Around the waveguide is a clearance area of $30\ \mu m$. These dimensions for the straight waveguide are kept constant throughout all waveguide designs, including the ring resonators and the CROW mask designs.

Figure 4-7:The straight waveguide mask design. Not to scale.

4.2.2.2 Ring resonators

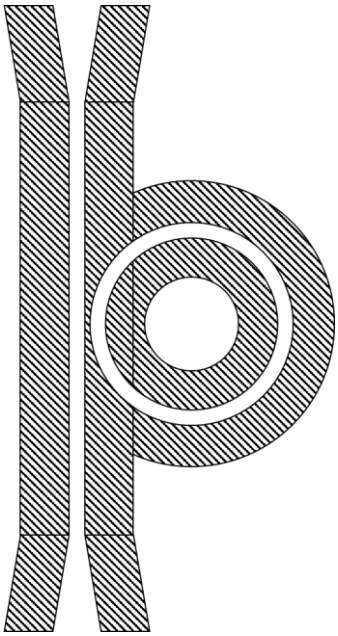

The mask design for the ring resonator in Figure 4-8 can be seen as a continuation of the straight waveguide design. The straight waveguide parameters were kept constant with a waveguide width of $2\ \mu m$, taper length of $200\ \mu m$, taper end width of $10\ \mu m$ and over-all length of $2400\ \mu m$. The variable parameters for the ring resonator design were the outer radius of the ring waveguide and the gap between the ring and the straight waveguide. The width of the ring waveguide and the clearance area around and inside the ring were kept constant at $2\ \mu m$ and $30\ \mu m$ respectively.

Figure 4-8: Ring resonator mask design. Not to scale.

4.2.2.3 CROW

The mask designs for CROW structures were a further development of the ring resonator design in which two types to CROW designs were made. The Type 1 CROW design can be seen in Figure 4-9 and consists of two straight waveguides with coupled resonator waveguide rings between them. Type 1 has a rectangular clearance area around all the resonator rings, keeping the minimum clearance to $30\ \mu m$.

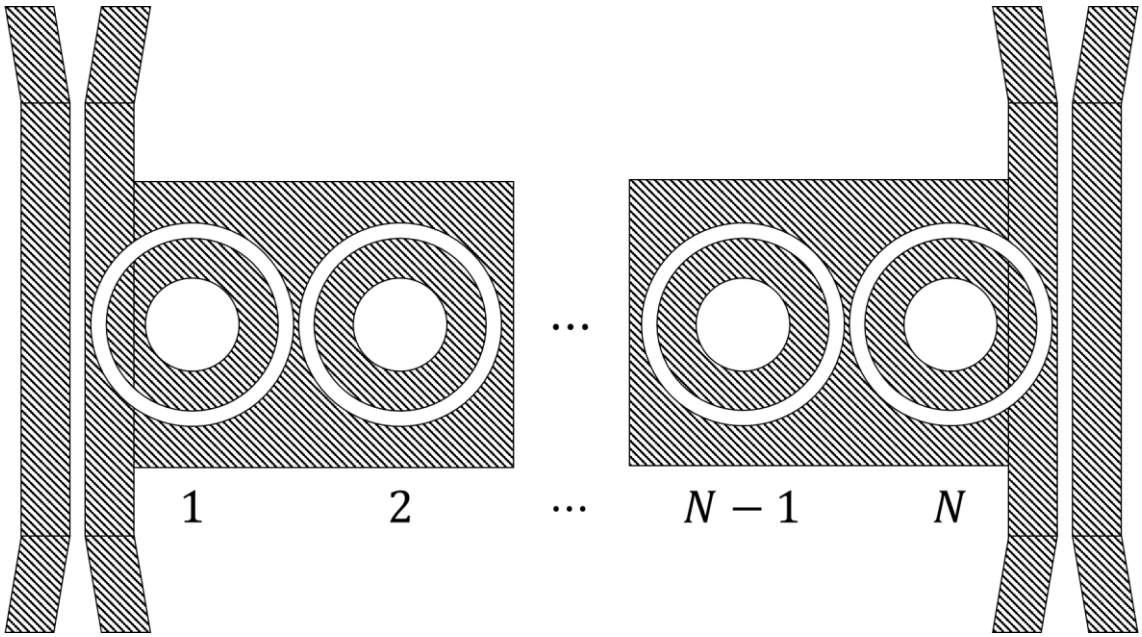

Figure 4-9: CROW design Type 1. The coupled resonators are encased by a clearance box. Not to scale.

The Type 2 seen in Figure 4-10 tries to maintain the $30\ \mu m$ clearance area established by the straight waveguide and the ring resonator design with the use of merges circles.

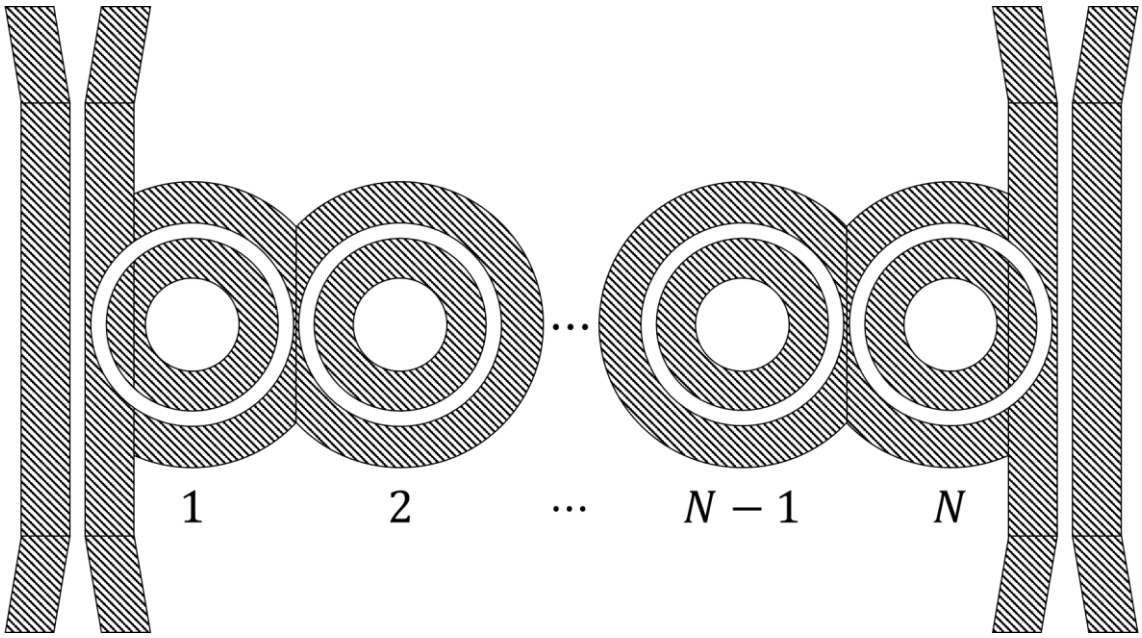

Figure 4-10: CROW design Type 2. The coupled resonators are encased by individually by circular clearance spaces to maintain the $30\ \mu m$ *width. Not to scale.*

The reason for creating two types of design was to investigate the effect the clearance area has on etch depth uniformity, which is related to uniformity of the waveguide height.

4.2.3 Deviations from the fabrication method

The following sections detail what mask design was used on each wafer and when the fabrication process deviated from the method stated in Appendix 1.

4.2.3.1 Wafer 1 and 2

The mask design for the two first wafers were several straight waveguides spaced out by $5\ mm$. On wafer 1 (W1) the waveguide width was $2\ \mu m$, while on wafer 2 (W2) it was $1\ \mu m$. The exposure recipe used was the "Medium Resolution S1813" with a step size of $300\ nm$. Focus was achieved at a Z-adjustment of $0.383\ mm$ with a red laser power of $150\ \mu W$ and $100\ \mu W$ for W1 and W2 respectively.

The remaining photoresist after dry etching was removed by placing the wafers in an ultrasound bath. First in acetone for $10\ min$ and then in isopropanol for $2\ min$. Then they were washed with DI water and blow dried with N (nitrogen) gas.

4.2.3.2 Wafer 3

The mask design used for the third wafer (W3) was a 6×3 grid of ring resonators. After every second column, the gap between the ring waveguide and the straight waveguide would increase from $200\ nm$, to $300\ nm$, to $500\ nm$. While row increased the diameter of the ring waveguide by $50\ \mu m$, starting at $100\ \mu m$.

Focus was found to be stable across the mask area on the wafer when the red laser power was $150\ \mu W$. The Z position was approximately $382\ \mu m$.

It was decided to remove the remaining photoresist without the use of an ultrasound bath. After $30\ min$ of washing with acetone, isopropanol, and DI water there was no sign that all the remaining photoresist was clearing, so the wafer was cleaned with plasma in cycles. The settings for the plasma cleaner can be seen in Table 4-5. Between each cycle, the wafer was washed with acetone, isopropanol and DI water and inspected with the Nikon microscope. Finally, W3 was exposed with UV light for $150\ s$ with the UVaCube 100 to break the polymer chains in the residual photoresist. After cleaning with acetone, isopropanol and DI water, W3 was considered free from photoresist.

Table 4-5: The plasma cleaning cycle for W3.

CLEANING CYCLE NUMBER	POWER $[W]$	O_2 GAS $[sccm]$	TIME $[min]$
1	100	100	1
2	200	200	1
3	200	200	1
4	400	200	2
5	500	200	2
6	600	200	6

4.2.3.3 Wafer 4

The mask used for wafer 4 (W4) was a 3×5 grid of $1\ \mu m$ straight waveguides evenly spaced out every $5\ mm$.

The focus was found for a red laser power of $150\ \mu W$ and exposure was done with a step size of $300\ nm$.

To remove the photoresist after dry etching, W4 was first exposed with UV light two times for $3\ min$ with a wash of acetone, isopropanol, and DI water in between. Then the wafer was plasma cleaned according to Table 4-6, with a wash of acetone, isopropanol, DI water and blow dried with N gas between each cycle.

Table 4-6: The plasma cleaning cycle for W4

CLEANING CYCLE NUMBER	POWER $[W]$	O_2 GAS $[sccm]$	TIME $[min]$
1	200	200	2
2	600	200	4
2	600	200	6

4.2.3.4 Wafer 5

For wafer 5 (W5) the same mask design was used as for W3. However, for this mask the fabrication grid in L-edit was adjusted to $1\ nm$ as opposed to $250\ nm$ for W3 and another row of $2\ \mu m$ straight waveguides was added above the resonators.

The focus was set with a red laser power of $130\ \mu W$. The exposure was cancelled after $4\ h$ when a "No sum signal detected" error message came on the laser writer display. The immersion development was done in progressively shorter durations down to $5\ s$ as seen in Table 4-7, until the structures were considered fully developed when viewed under a Nikon optical microscope. Between every immersion, the wafer was rinsed with DI water and blow dried with N gas.

Table 4-7: Immersion duration for the photoresist development of W5

IMMERSION CYCLE NUMBER	IMMERSION TIME
1	$20\ s$
2	$10\ s$
3	$5\ s$
4	$5\ s$
5	$5\ s$
6	$5\ s$

Just like with W3 and W4, the photoresist was removed using a combination of UV exposure, plasma cleaning and an acetone, isopropanol, and DI water wash.
Between cycles 3 and 4 of the plasma cleaning, the wafer was exposed to UV light for $3\ min$. In cycle 5 and 6, the wafer was fastened with high temperature tape to prevent it from sliding into one corner of the vacuum chamber when the vacuum was turned on.

Table 4-8: Plasma cleaning cycle for W5.

CLEANING CYCLE NUMBER	POWER $[W]$	O_2 GAS $[sccm]$	TIME $[min]$
1	600	200	6
2	600	200	6
3	600	200	6
4	600	200	6
5	600	200	6
6	600	200	2

4.2.3.5 Wafer 6

The mask used for wafer 6 (W6) was two 3×3 grids of Type 1 and Type 2 CROW designs. The waveguide with was $2\ \mu m$ and the ring radius was $50\ \mu m$. For W6 a new exposure recipe was made with a high-resolution spot size. The exposure energy was kept the same from the medium resolution recipe at $180\ mJ \cdot cm^{-3}$ and the aperture was kept the same.

The focus was found with a red laser power of $140\ \mu W$ and the step size was $120\ nm$.

After dry-etching, W6 was exposed with UV light for $3\ min$ before being washed three times with acetone, isopropanol and DI water and then plasma cleaned according to Table 4-9. The wafer was fastened using high temperature tape to prevent it from sliding inside the vacuum chamber. W6 was washed with acetone, isopropanol and DI water between every cycle.

Table 4-9:Plasma cleaning cycles and parameters for W6.

CLEANING CYCLE NUMBER	POWER $[W]$	O_2 GAS $[sccm]$	TIME $[min]$
1	600	200	6
2	600	200	6
3	600	200	6

4.2.3.6 Wafer 7

The same CROW design as W6 was used for wafer 7 (W7). However, the wafer used was a Si wafer and this time the photoresist was diluted with one-part S1813 and one-part MICROPOSIT EC solvent to create a 50/50 photoresist solution. This was done because the depth of focus when using the high resolution spot size changes from $800\ nm$ to $300\ nm$, and the photoresist thickness using a profilometer was found to be roughly $250\ nm$ with the 50/50 photoresist solution when using the spin coating parameters shown in Appendix 1.

The exposure recipe was changed to reflect this change in photoresist. The exposure energy was changed to $100\ mJ \cdot cm^{-3}$ and the aperture was changed to the high-resolution setting as well.

Focus was found with a red laser power of $140\ \mu W$ at a Z-adjustment of $0.383\ mm$ and the step size was $120\ nm$.

Because of the thin photoresist, W7 was immersed for $10\ s$.

For W7 a two-step Bosch Process was used instead of a four-step process. This was done to ensure that the etching process would not etch through the thin photoresist.

To remove the remaining photoresist, W10 was first exposed to UV light for $3\ min$. Then it was washed twice with acetone, isopropanol and DI water, given one cycle using the plasma cleaner at $600\ W$, $200\ sccm$ of O_2 for $6\ min$ before receiving yet another wash with acetone, isopropanol and DI water. W7 was also taped with high temperature tape to prevent it from sliding.

4.3 Measurements

The fabricated waveguide structures were inspected and measured using two primary tools. First, since the mode behaviour of the light is only affected by the waveguide dimensions and not the etch depth of the wafer, it was only considered necessary to measure the waveguide height. This was done with the Wyko NT9100 interferometer with the VSI setting.

Second, the waveguide was inspected, and the lateral dimensions measured using the Hitachi SU 3500 scanning electron microscope (SEM). To look at the cross-section of the of the waveguide structure and inspect the horizontal effects of the dry-etching process, it was necessary to expose the end of the waveguide taper by dicing the wafer. The dicing was done with the Disco DAD 3220 dicing saw. The lateral dimensions of interest were the gap between the ring and the straight waveguide, as well as the width of the waveguides themselves.

5 Results

5.1 Simulation and computation results

5.1.1 Comparison results

5.1.1.1 Vectoral Mode Solver with Zero-boundary Condition

5.1.1.1.1 “Analysis of Vectoral Mode Fields in Optical Waveguides by a New Finite Difference Method” by P. Lüsse et al. [16]

The step-index fibre described in 4.1.2.4.1 was solved for 4 modes with the VMS-ZB MATLAB script and with the COMSOL mode solver application for the same number of modes. The n_{eff} found by the MATLAB script and COMSOL application are shown in Table 5-1. The fundamental mode plots for MATLAB and COMSOL can be seen in Figure 5-2 and Figure 5-3 respectively.

Table 5-1: The MATLAB and COMSOL effective index for the step-index fibre from P. Lüsse et al.[16].

SOLUTION NUMBER	MATLAB n_{eff}	COMSOL n_{eff}
1	3.41309384363593	3.4130933100341245
2	3.41309384363593	3.41309329785975
3	3.41053138521034	3.4105307446798414
4	3.41051570158344	3.410511843898246

The rib waveguide cross-section (see Figure 5-1) was computed with the MATLAB script and the COMSOL application in the same manner. The n_{eff} from MATLAB and COMSOL are shown in Table 5-2 and the field plots can be seen in Figure 5-4 and Figure 5-5 respectively.

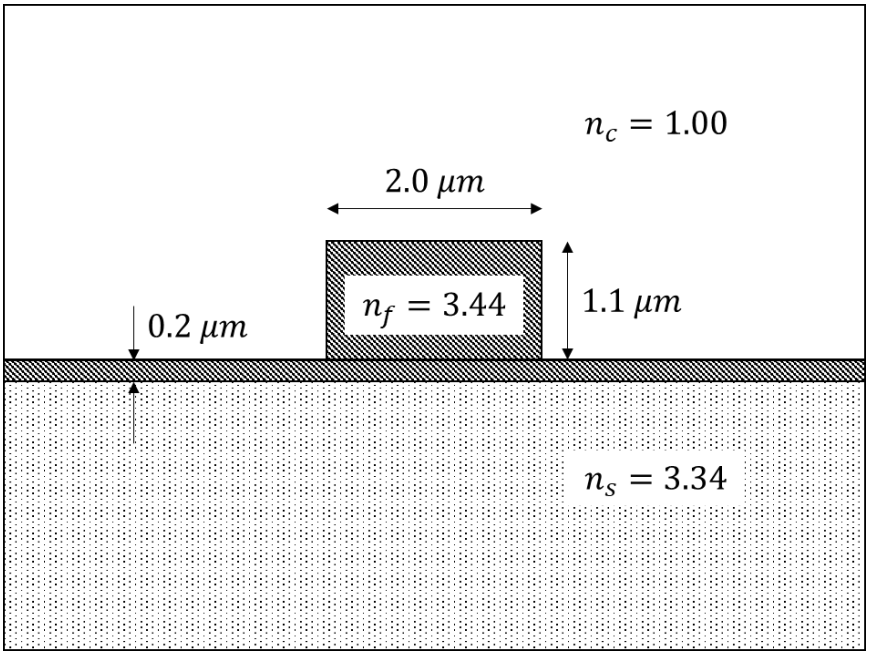

Figure 5-1: Rib waveguide cross-section.

Table 5-2: The MATLAB effective index for the rib waveguide described by P. Lüsse et al.[16].

SOLUTION NUMBER	MATLAB n_{eff}	COMSOL n_{eff}
1	3.38869041018487	3.3887057086577643
2	3.38786636156140	3.3878753240942427
3	3.33368626962421	3.3338507585211796
4	3.32940054231093	3.3326095949702124

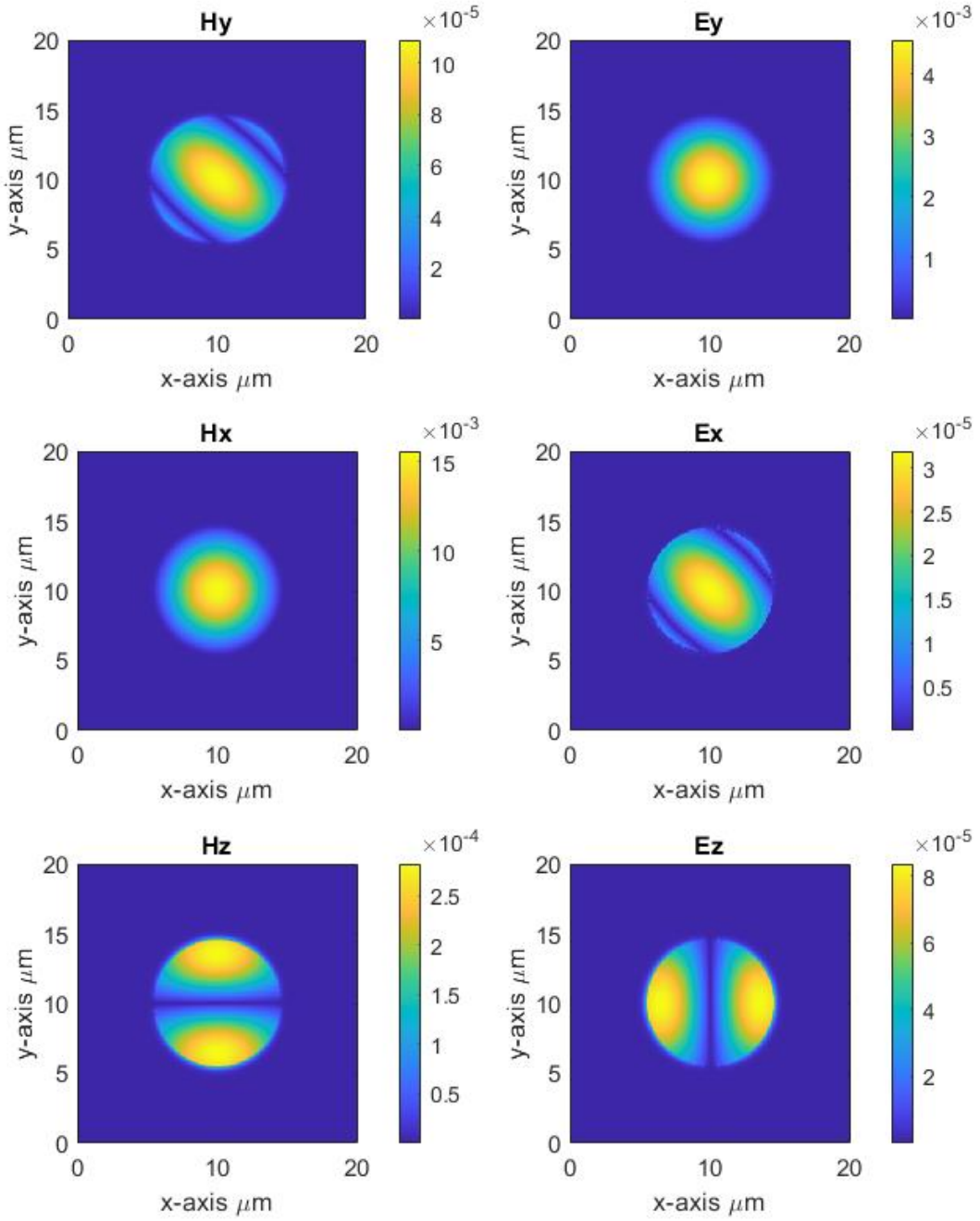

Figure 5-2: The field distribution for the fundamental mode from MATLAB.

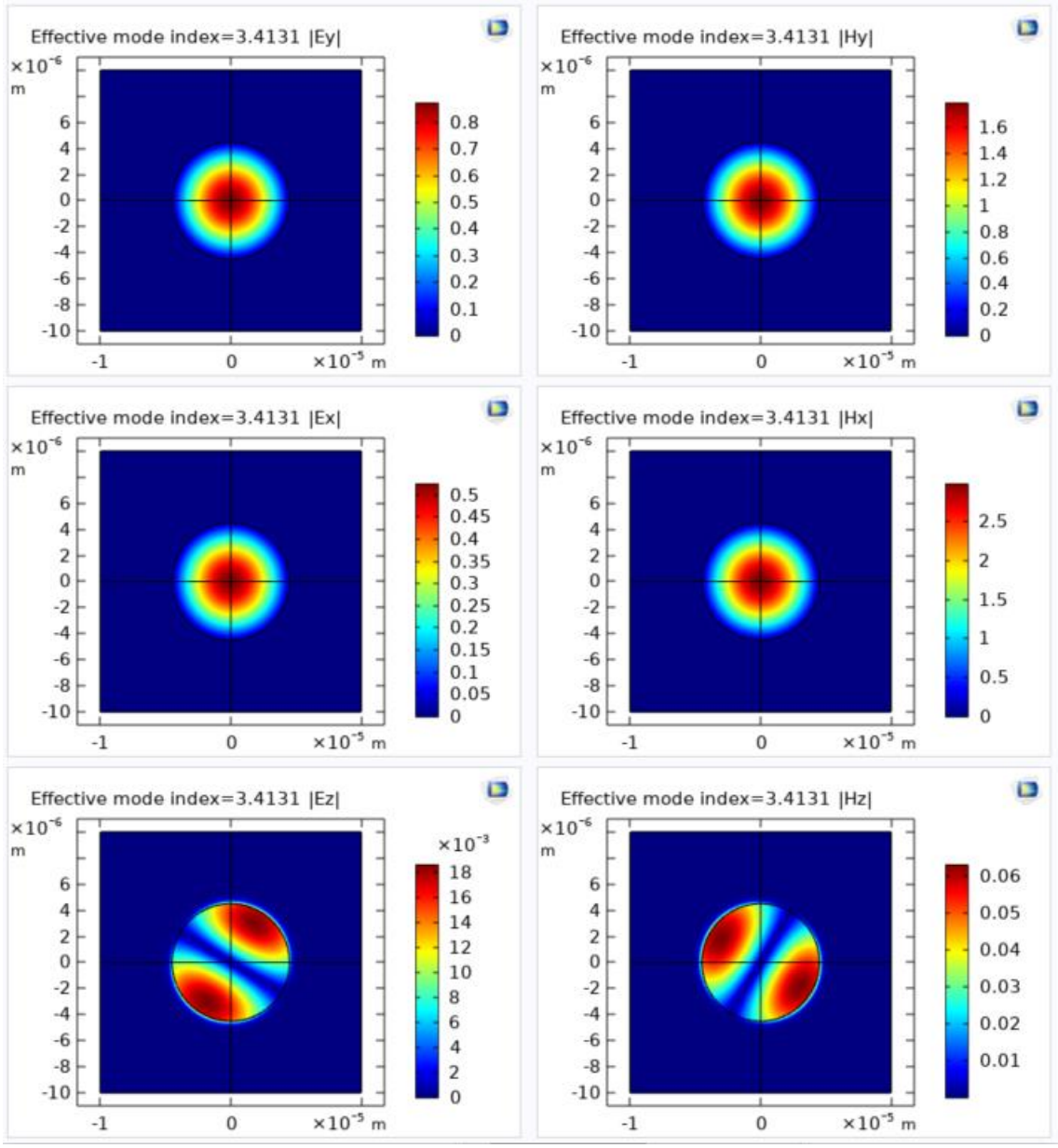

Figure 5-3: The field distribution for the fundamental mode from COMSOL.

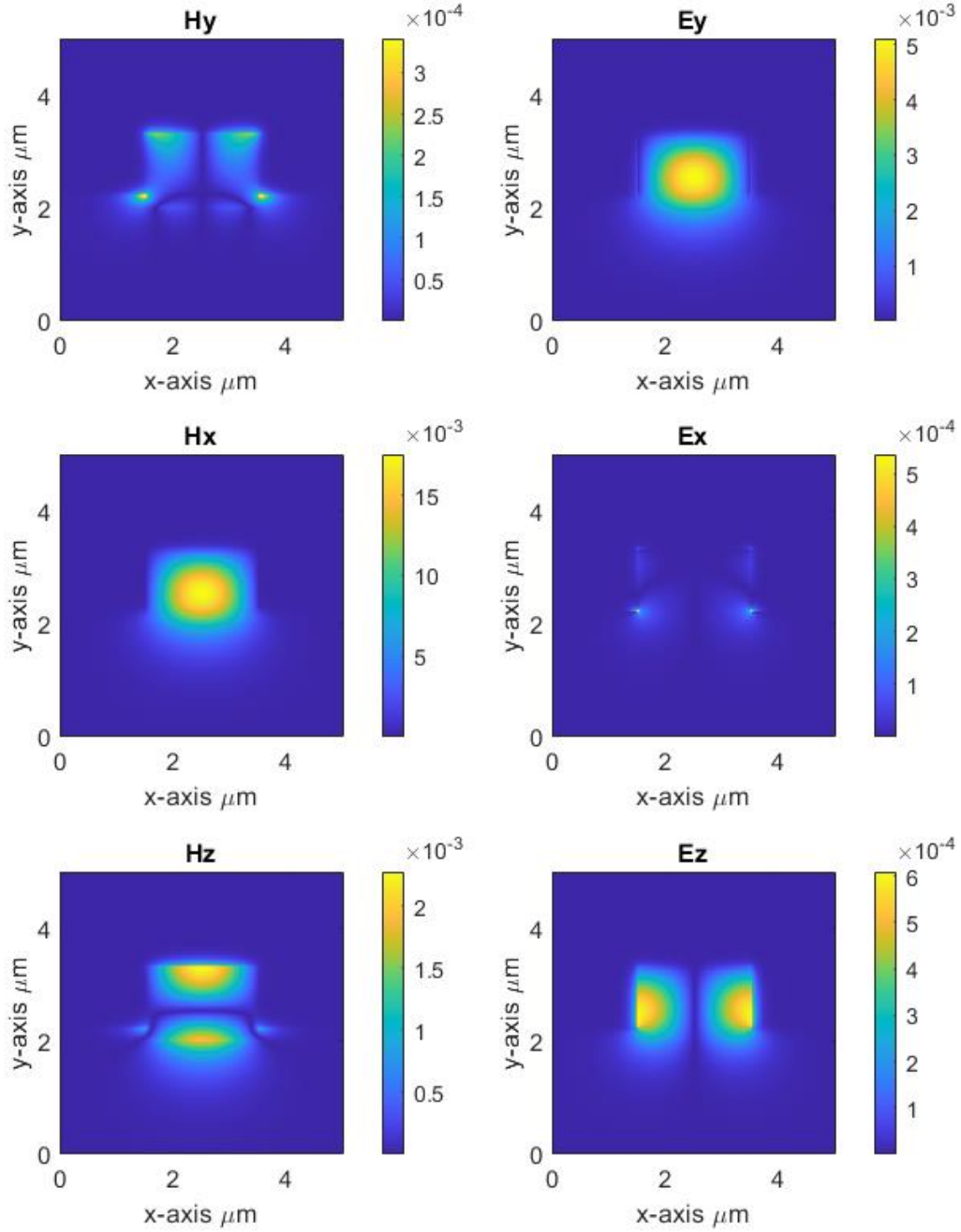

Figure 5-4: The field distribution for the rib waveguide described by P. Lüsse et al. from MATLAB.

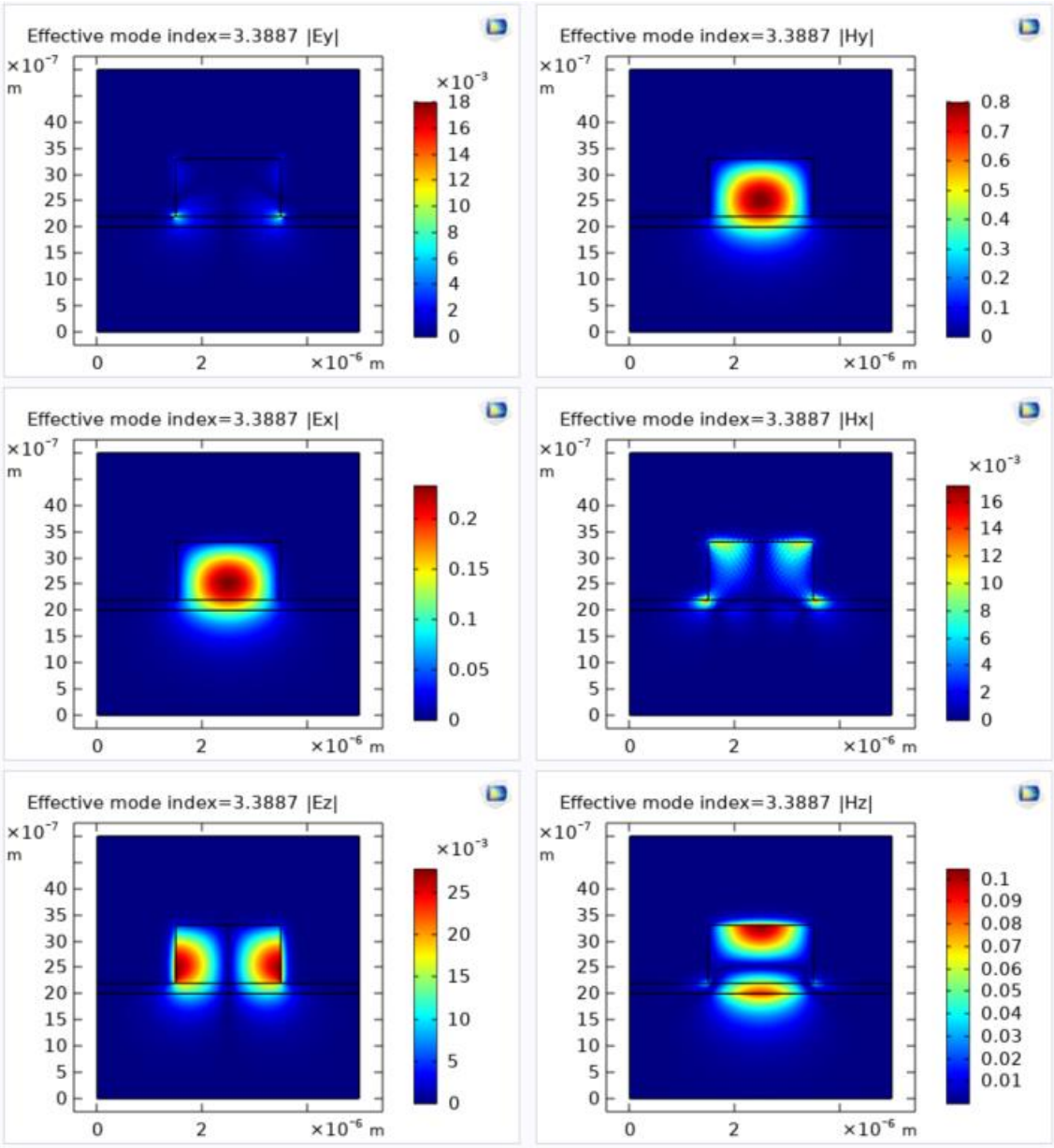

Figure 5-5: The field distribution for the rib waveguide described by P. Lüsse et al. from COMSOL [16].

5.1.1.1.2 “Full-vectoral finite-difference analysis of microstructured optical fibres” by Z. Zhu and T. G. Brown [14]

The step-index fibre and the MOF described in 4.1.2.4.2 were computed for four modes with the VMS with zero-boundary condition MATLAB script and the COMSOL mode solver application. The n_{eff} for the first four modes found by MATLAB and COMSOL for the step-index fibre is shown in Table 5-3 and the field distribution for the fundamental mode from MATLAB and COMSOL are shown in Figure 5-7 and Figure 5-8.

The MOF seen in Figure 5-6, could not be computed with the COMSOL mode solver application and a separate COMSOL model was made. The n_{eff} for the MOF from the MATLAB computation and COMSOL simulation are in Table 5-4, and the field distribution can be seen in Figure 5-9 and Figure 5-10 for MATLAB and COMSOL respectively.

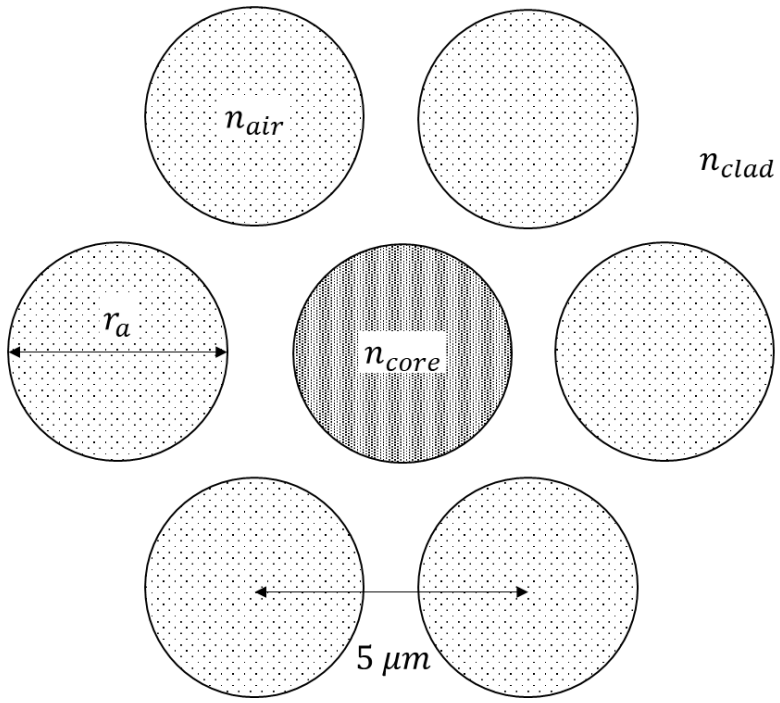

Figure 5-6: MOF cross-section and geometry.

Table 5-3: Effective index from MATLAB and COMSOL for the Step-index fibre described by Z. Zhu and T. G. Brown [14].

SOLUTION NUMBER	MATLAB n_{eff}	COMSOL n_{eff}
1	1.43859736229301	1.4386040581739772
2	1.43859736221840	1.4386040462338674
3	1.42203098571452	1.4220735301656535
4	1.42083649079673	1.420845243053876+3.280E-15i

Table 5-4: Effective index from MATLAB and COMSOL for the MOF described by Z. Zhu and T. G. Brown [14].

SOLUTION NUMBER	MATLAB n_{eff}	COMSOL n_{eff}
1	1.43537751078430	1.4353559700021377
2	1.43537637511320	1.4353558746715407
3	1.41769099522780	1.4149344823878502
4	1.41761896457530	1.4149334318411302

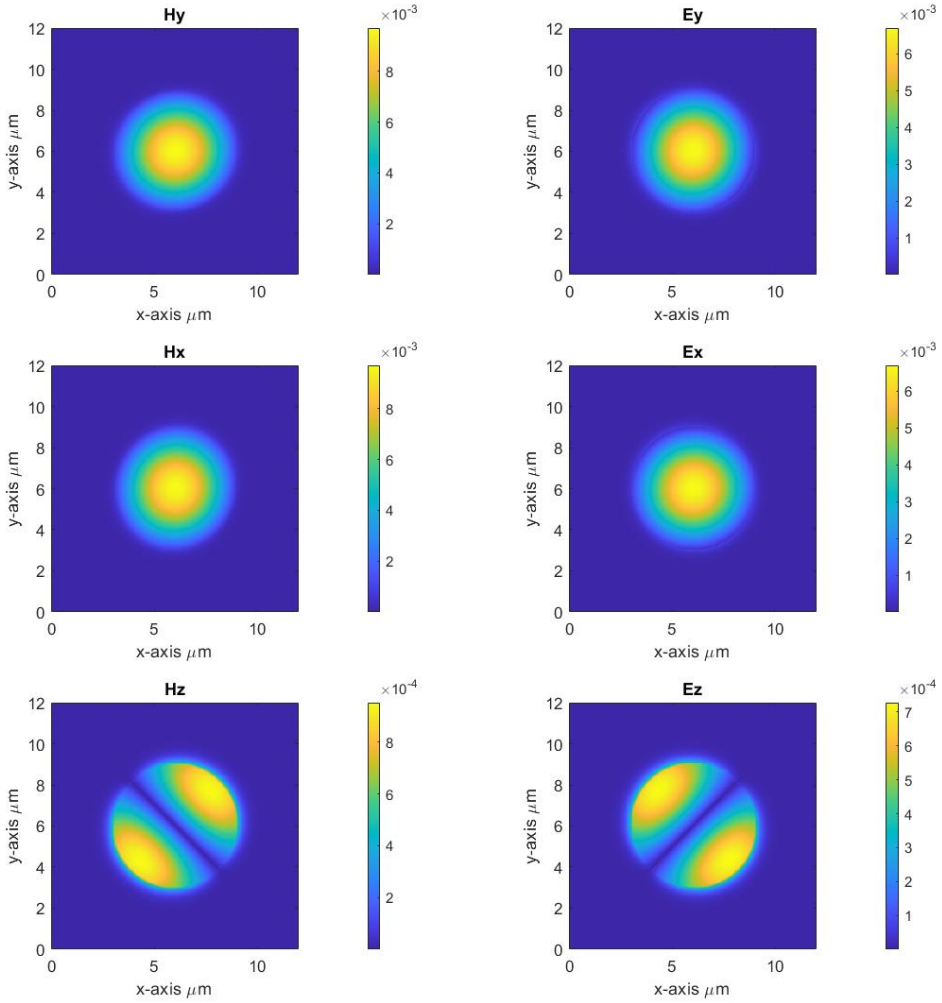

Figure 5-7: Field distribution from MATLAB for the step-index fibre described by Z. Zhu and T. G. Brown [14].

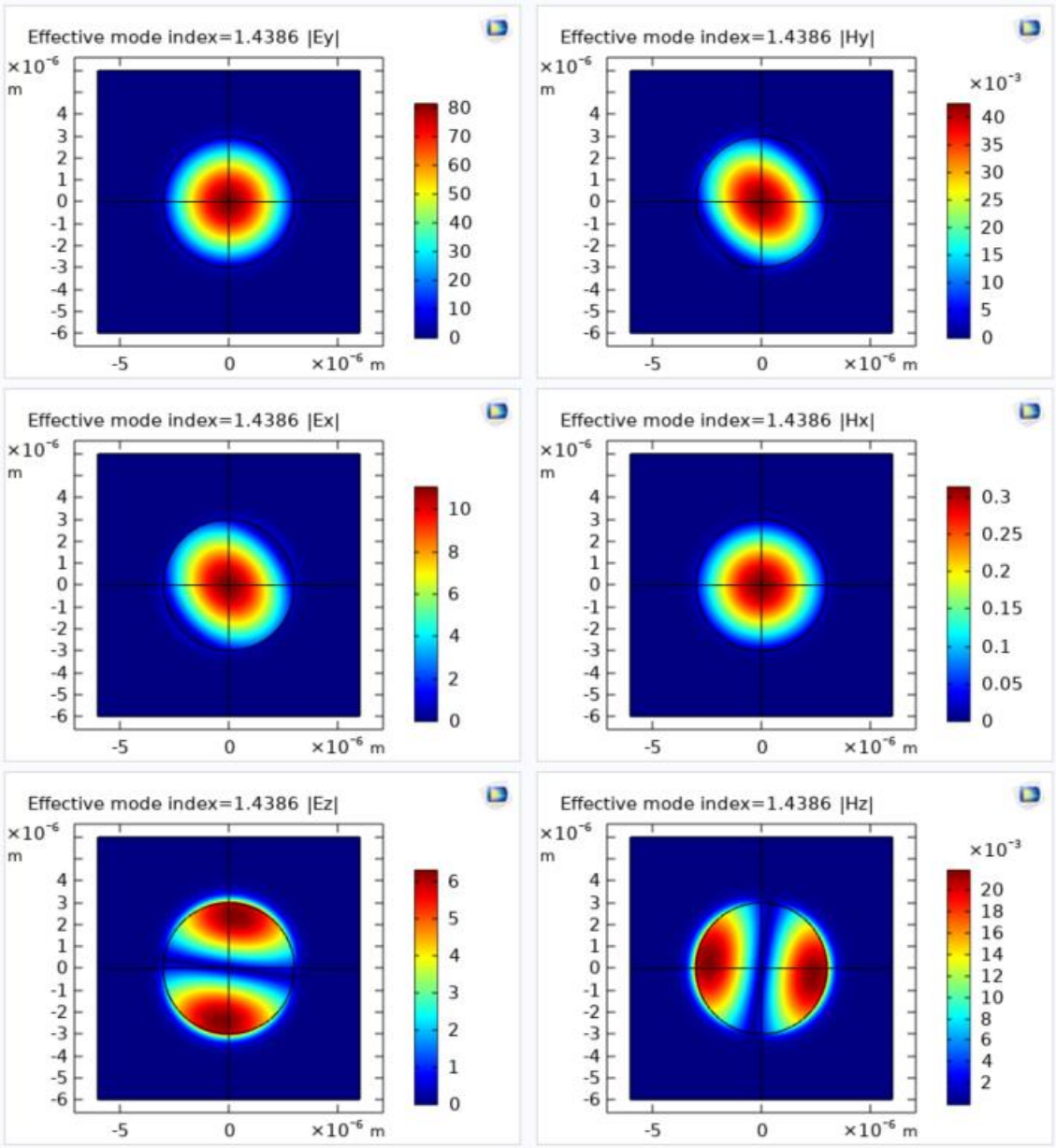

Figure 5-8: Field distribution from COMSOL for the step-index fibre described by Z. Zhu and T. G. Brown [14].

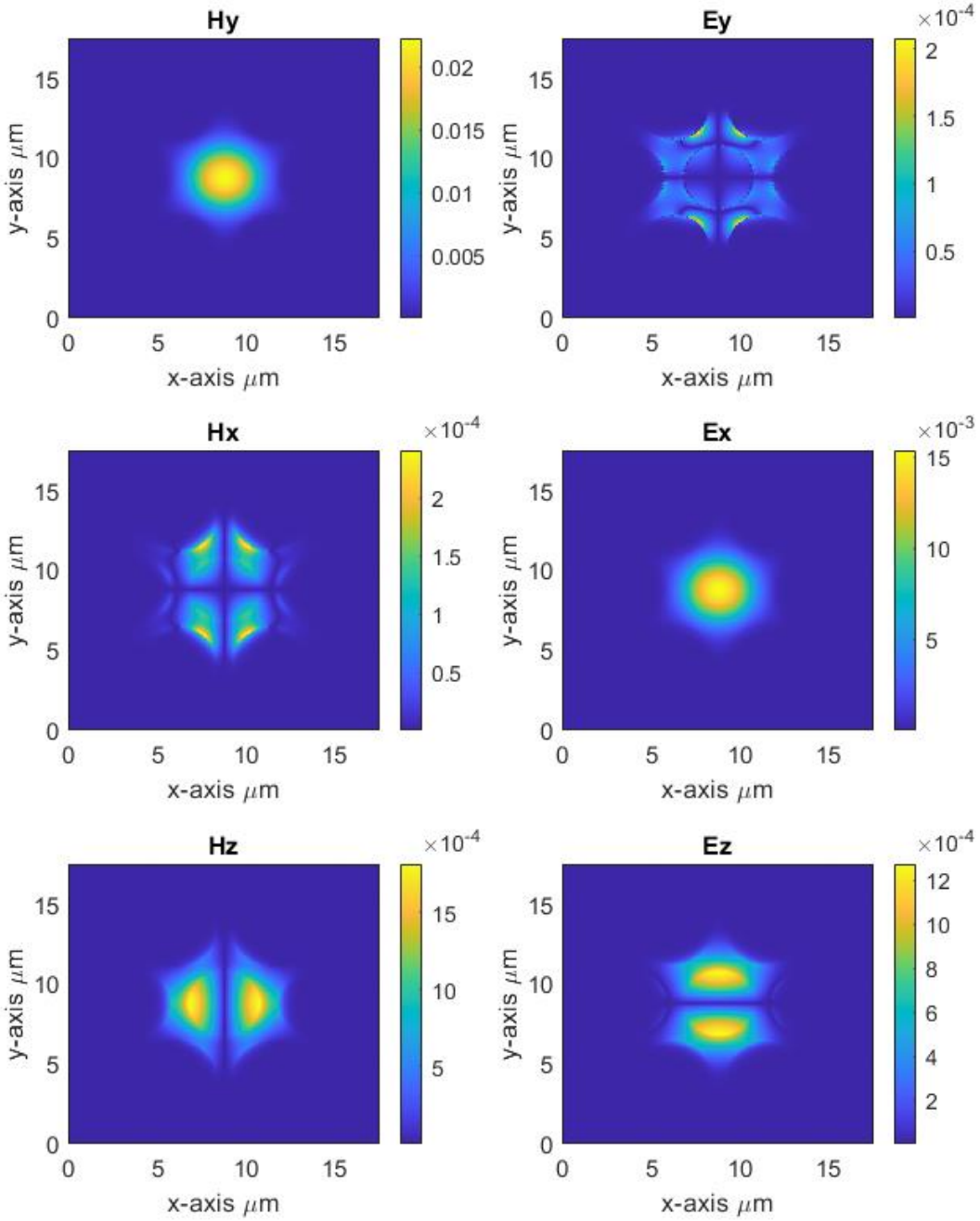

Figure 5-9: Field distribution from MATALB for the MOF described by Z. Zhu and T. G. Brown [14].

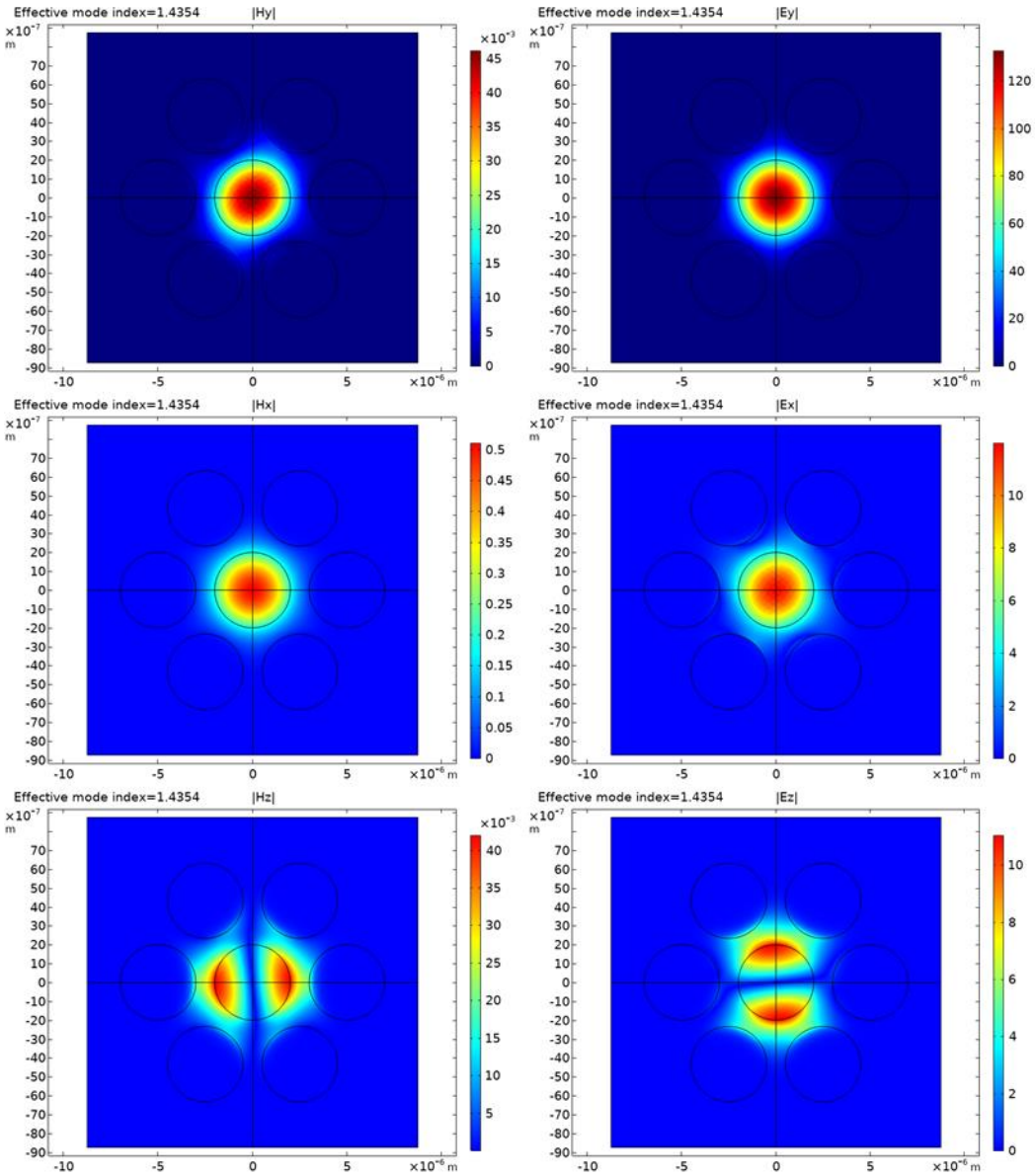

Figure 5-10: Field distribution from COMSOL for the MOF described by Z. Zhu and T. G. Brown [14].

5.1.1.2 Vectoral Mode Solver with PML Boundary

5.1.1.2.1 "Loss and dispersion analysis of microstructured fibers by finite-difference method" by S. Guo et al [13].

The PCF (see described in 4.1.2.4.3 was computed with the VMS-PML MATLAB script and a COMSOL model was made. The n_{eff} from the MATLAB computation and COMSOL are in

Table 5-5 and the field distribution can be seen in Figure 5-12 and Figure 5-13 for MATLAB and COMSOL respectively.

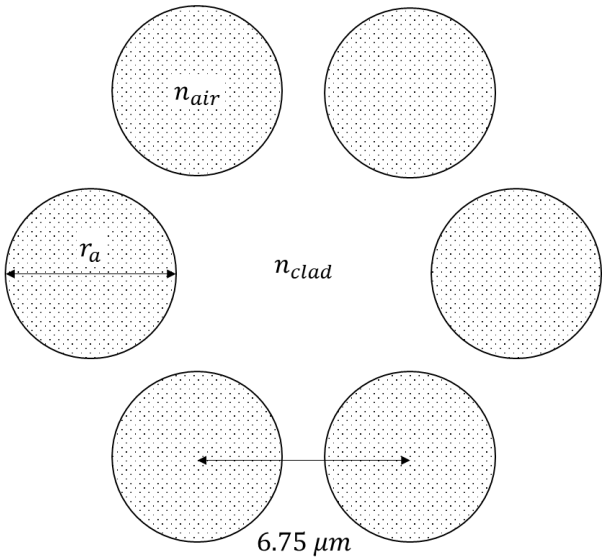

Figure 5-11: PCF cross-section and geometry.

Table 5-5: Effective refractive index from MATLAB and COMSOL for the PCF described by S. Guo et al. [13].

SOLUTION NUMBER	MATLAB (n_{eff})		COMSOL (n_{eff})	
1	1.44539849631293	- 4.837e-08i	1.4453949231175363	-3.478E-8i
2	1.44539898943157	- 4.243e-08i	1.4453944708063522	-3.636E-8i
3	1.44485418659477	-7.767e-04i	1.44705300285876	-9.778E-4i
4	1.44466022639790	- 7.863e-04i	1.4470529910052303	-9.780E-4i

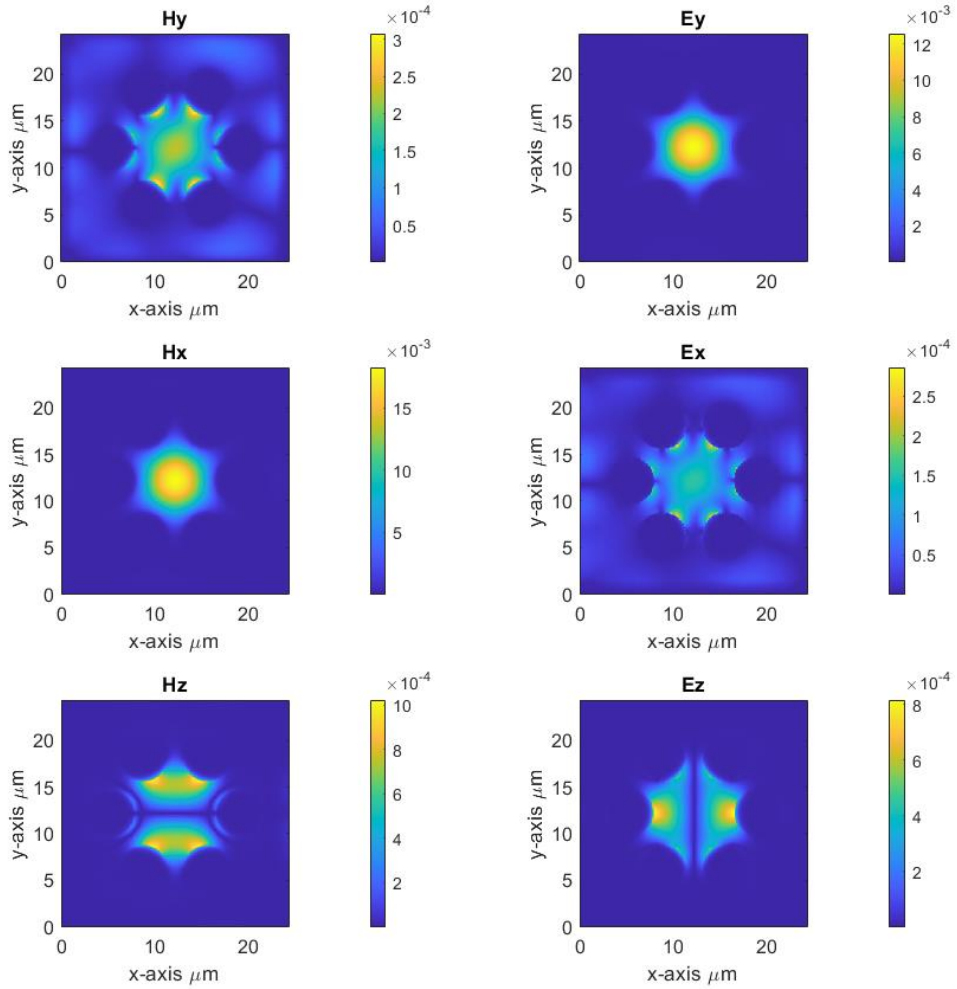

Figure 5-12: Field distribution from MATLAB for the PCF.

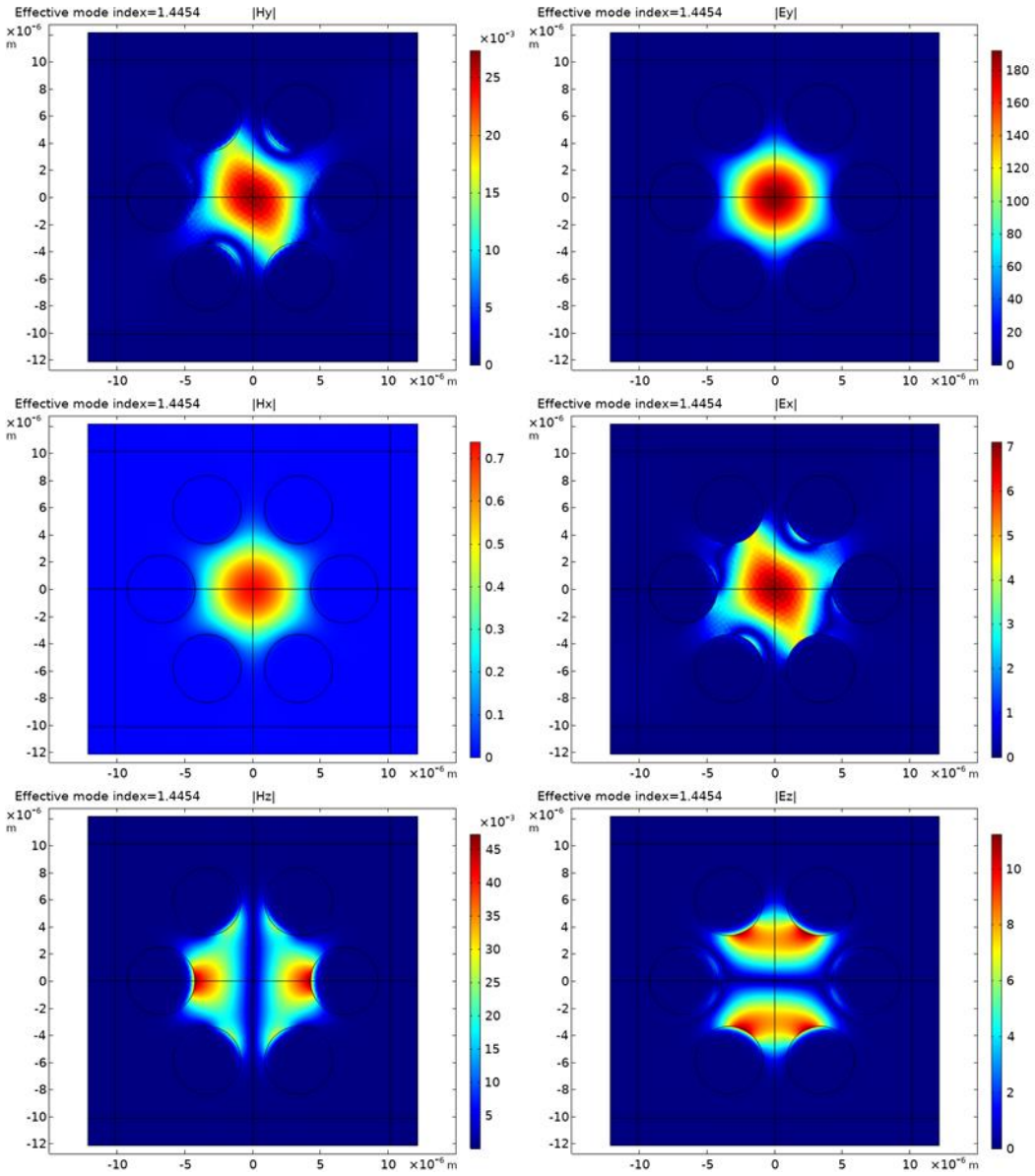

Figure 5-13: Field distribution from COMSOL for the PCF.

5.1.2 Anisotropic Material

The anisotropic behaviour described in 4.1.2.3 was applied to the step-index fibre described by P. Lüsse et al. and computed with the MATLAB script [16]. The same anisotropic waveguide was modelled and computed in COMSOL. The n_{eff} found by the MATLAB script and the COMSOL model are shown in Table 5-6 and the field distribution from MATLAB can be seen in Figure 5-14. The field distribution from COMSOL can be seen in Figure 5-15.

Table 5-6: Effective refractive index from MATLAB and COMSOL for the anisotropic step-index fibre.

SOLUTION NUMBER	MATLAB n_{eff}	COMSOL n_{eff}
1	3.41309379503792	3.413093254673717
2	3.41052108336459	3.4105222064124923
3	3.41050692716056	3.410502057709264
4	3.40712680037353	3.407119225220625

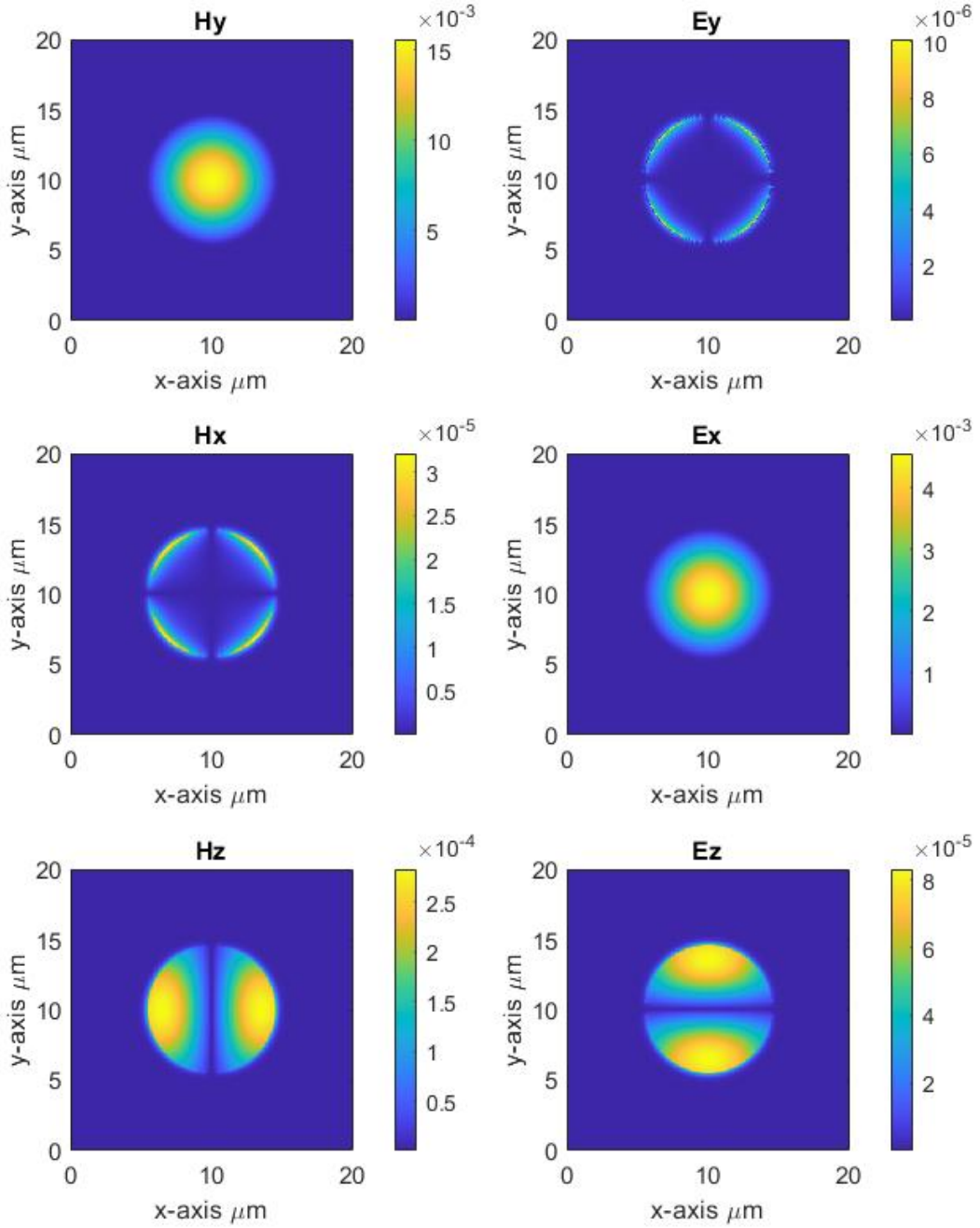

Figure 5-14: The field distribution from MATLAB of the anisotropic step-index fibre.

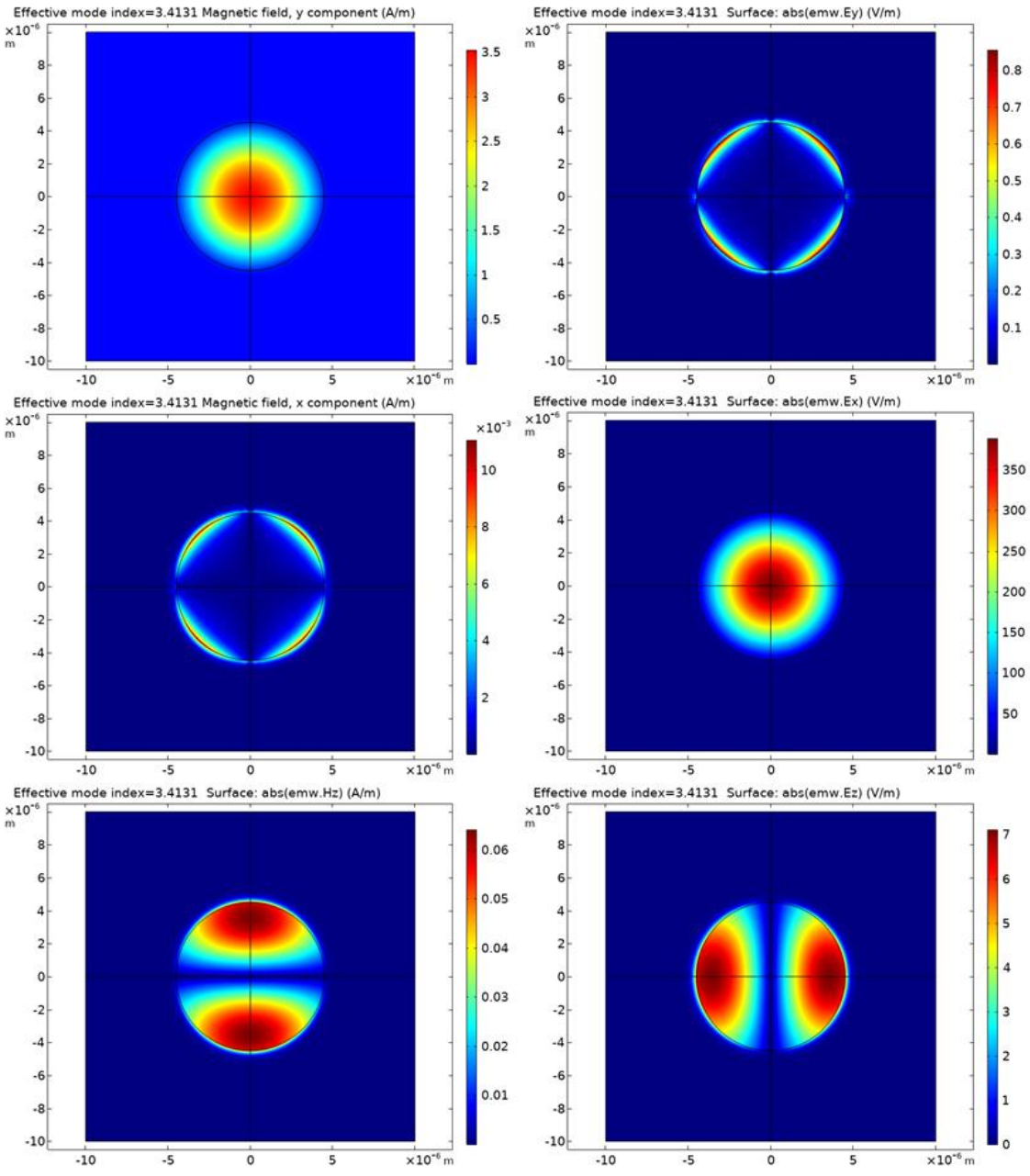

Figure 5-15: Field distribution for the anisotropic step-index fibre from COMSOL.

5.1.3 Ring resonator simulation

Figure 5-16 shows the transmittance response to input wavelength on the ring resonator described in 4.1.1. The theoretical resonance wavelengths were calculated using (2-21) and tabulated in Table 5-7.

Table 5-7: Theoretical resonance wavelengths for the ring resonator.

WAVELENGTH $[\mu m]$
1.5181
1.5161
1.5141
1.5121
1.5101
1.5082
1.5062
1.5042
1.5023
1.5003

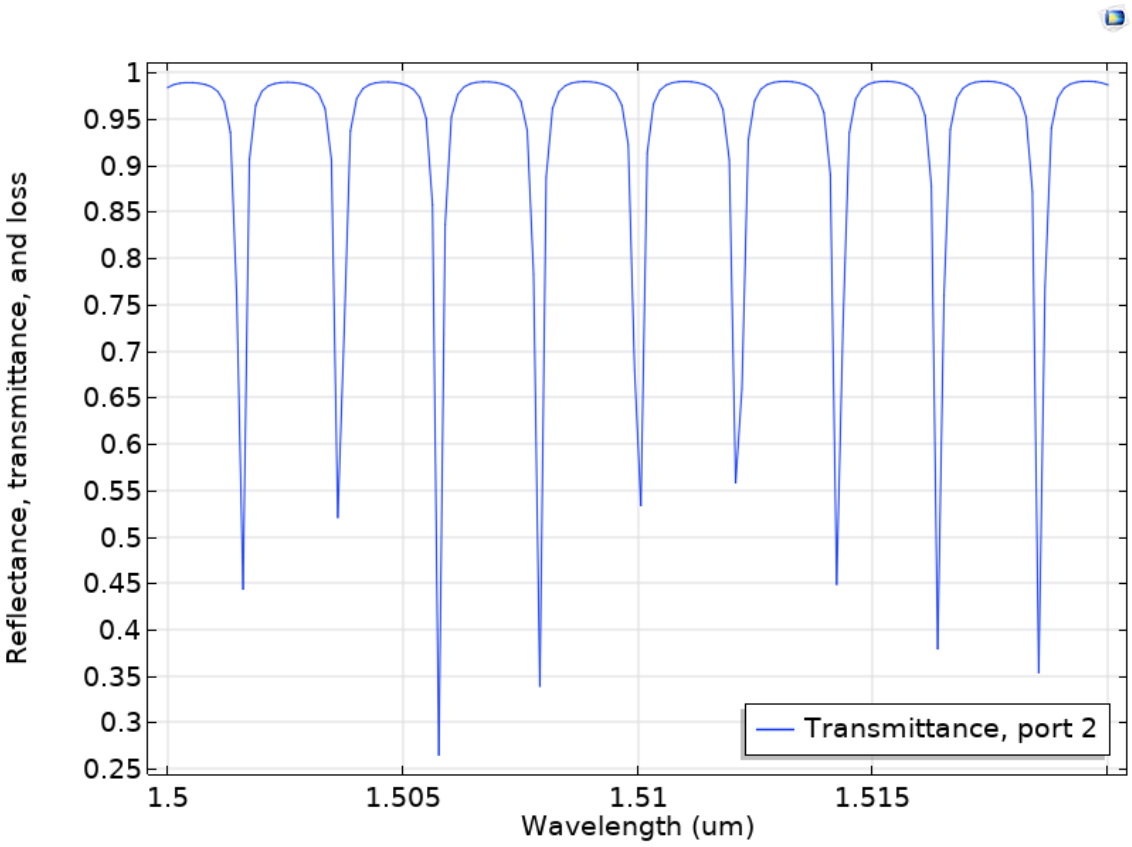

Figure 5-16: Wavelength response of the transmitted light through the ring resonator.

5.2 Fabrication

5.2.1 Straight waveguides

5.2.1.1 Wafer 1 and 2

As can be seen in Figure 5-17, measurements with the interferometer showed that the $1\ \mu m$ straight waveguides on W2 had been destroyed after the photoresist removal. The waveguides on W1 were fine and the wafer was diced before measurements with the SEM.

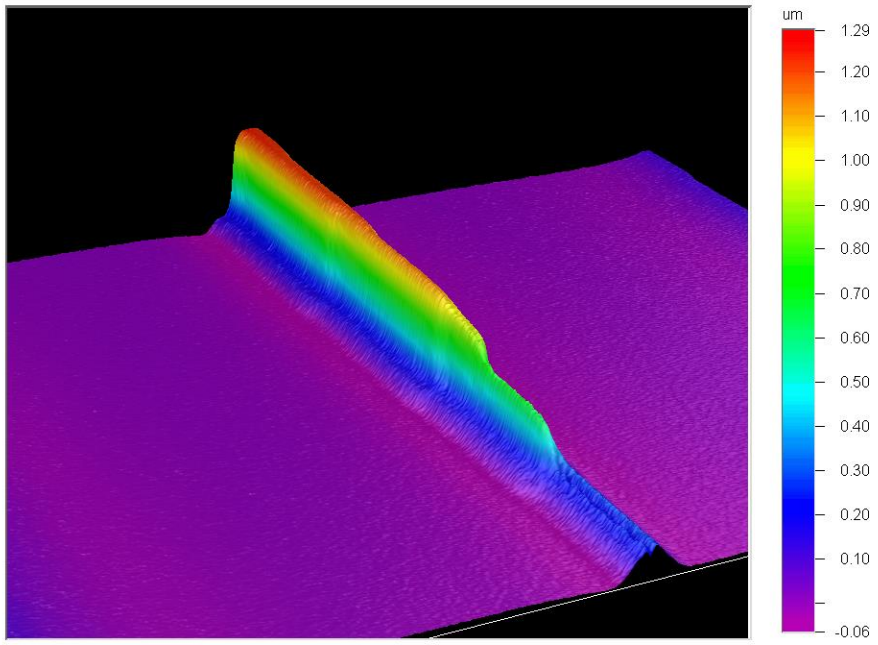

Figure 5-17: The taper area of the $1\ \mu m$ *straight waveguide. Magnification:* 100.47.

The dicing resulted in heavy chipping along the cutting edge even when the speed at which the saw moved across the wafer was reduced, see Figure 5-18.

Figure 5-19 shows the cross-section of the $10\ \mu m$ taper at the end of the waveguide and indicates a relatively square profile, the high contrast lines on the sidewall are from the deep reactive-ion etching (DRIE) process.

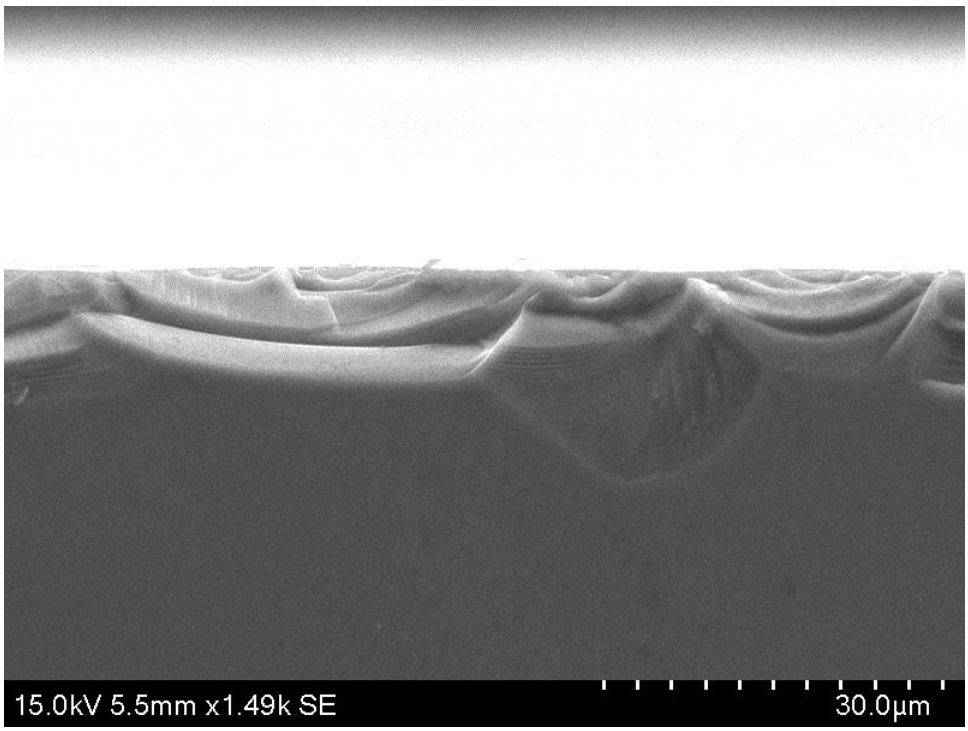

Figure 5-18: Chipping of the cutting edge from dicing with a slowed down cutting speed.

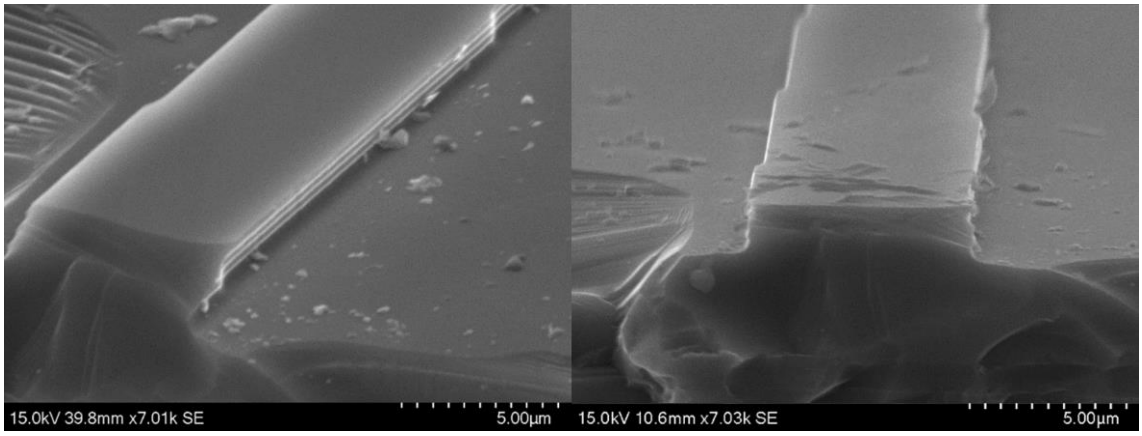

Figure 5-19: Cross-section at the waveguide end. The white lines in the left image on the waveguide wall are a result of the DRIE process.

5.2.1.2 Wafer 4

Measurements from the interferometer indicated that the majority of the waveguides were partially destroyed during the photoresist removal process as seen in Figure 5-20. Apart from the waveguides in column three, no other waveguide recorded a height of more than $0.650\ \mu m$ as can be seen in Table 5-8, which is less than 50% of the estimated etch depth of $1.340\ \mu m$.

Table 5-8: Waveguide heights for W4 measured with the interferometer.

	COLUMN [μm]			
ROW	1	2	3	4
1	0.456	0.566	1.009	0.553
2	0.522	0.564	0.959	0.581
3	0.529	0.533	0.996	0.643
AVG.				

However, inspection with the SEM contradicted the interferometer results since the waveguides seemed to be intact as shown in Figure 5-21. The width of the waveguides was measured between the strong contrast lines, as seen in Figure 5-22.

On average the waveguide width was $0{,}350\ \mu m$, with little variation across the wafer except for the third column. The third column of waveguides had an average width of $0.590\ \mu m$ compared to the other waveguides with a width of $0.270\ \mu m$.

Table 5-9: Waveguide widths for W4 measured with the SEM.

	COLUMN [μm]			
ROW	1	2	3	4
1	0.273	0.257	0.582	0.237
2	0.283	0.301	0.593	0.258
3	0.287	0.287	0.589	0.238
AVG.	0.281	0.282	0.588	0.244

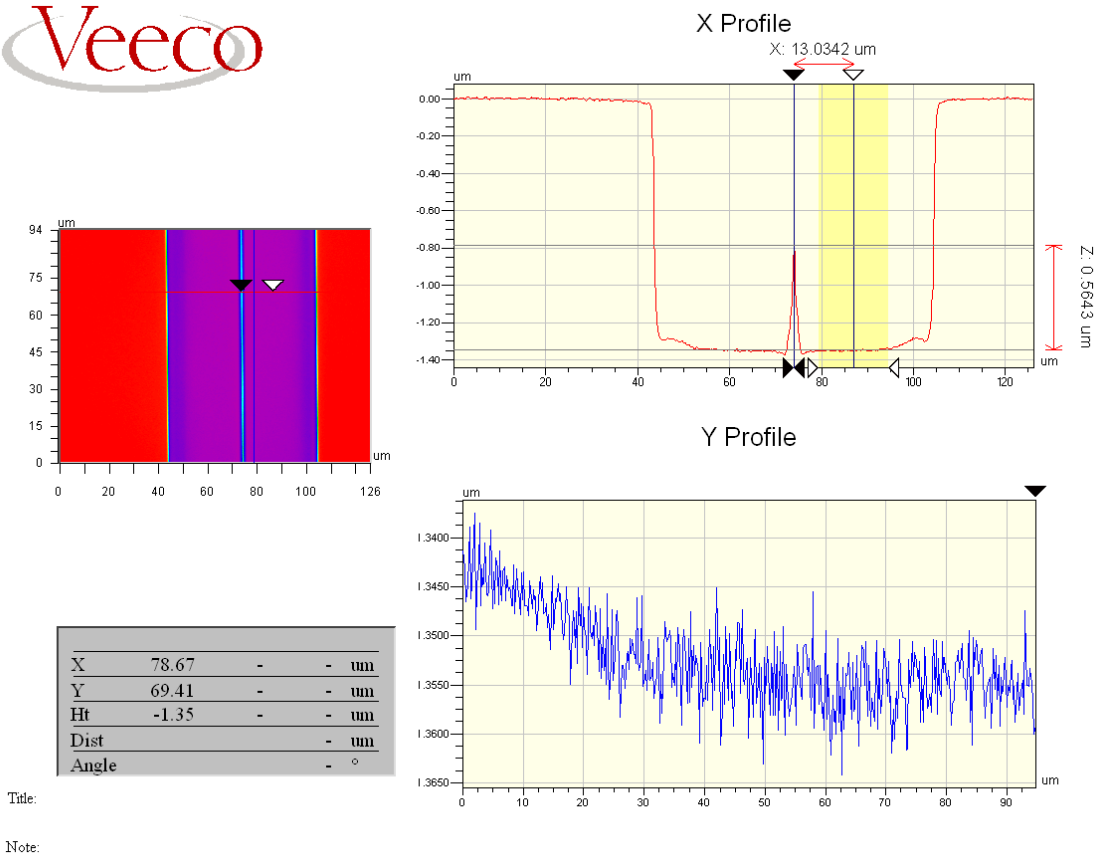

Figure 5-20: Height measurement of the 1 *µm straight waveguide. The height of the waveguide is significantly less than the etch depth.*

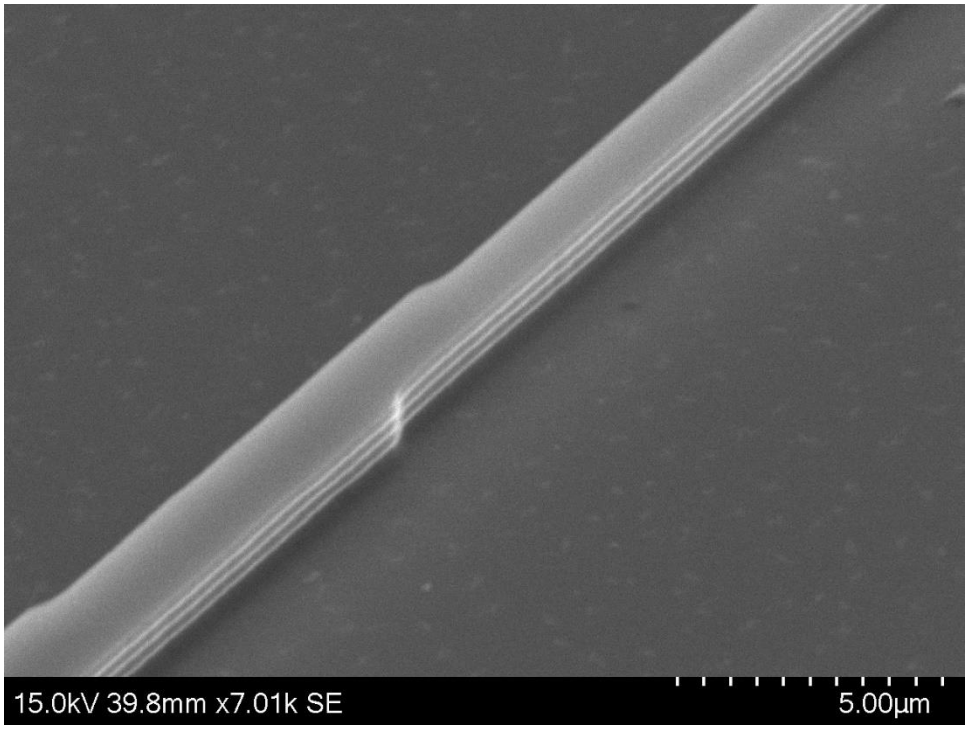

Figure 5-21: The 1 *µm waveguide transitioning into the end taper.*

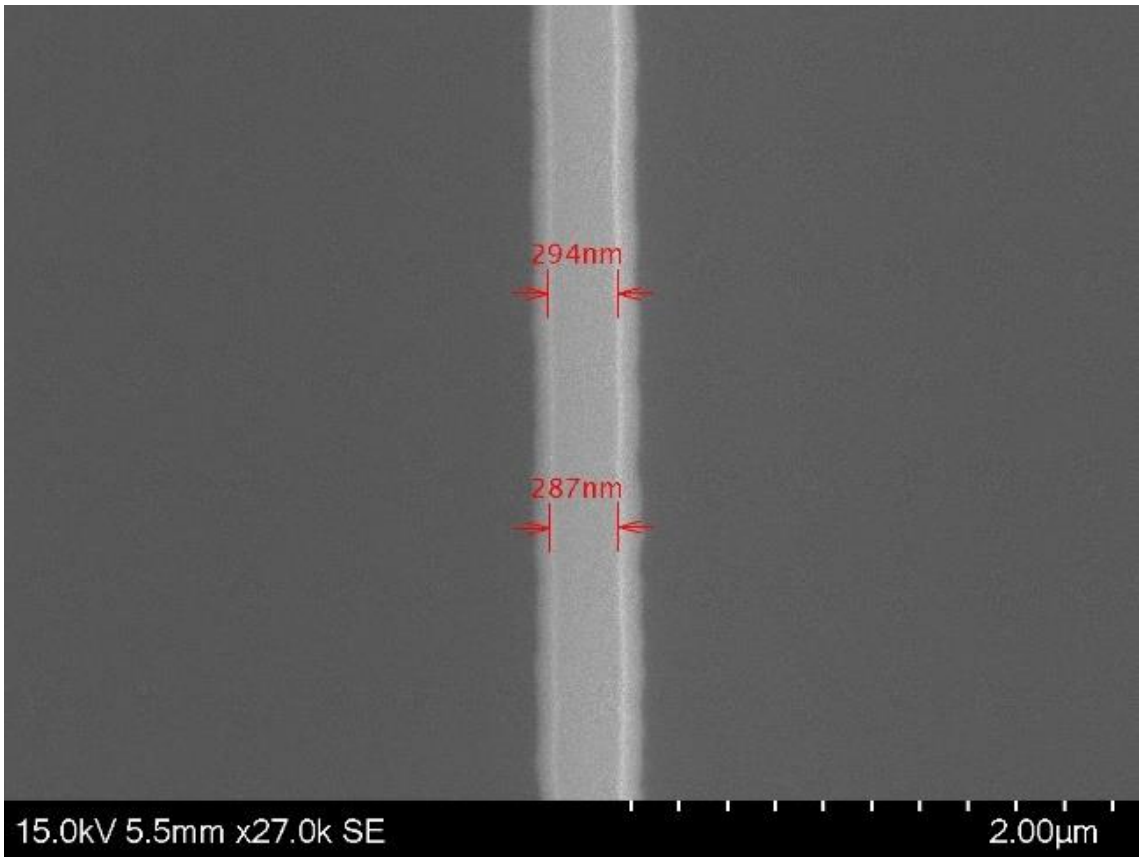

Figure 5-22: The width measurements were done on the strong contrast line.

5.2.2 Ring resonators

5.2.2.1 Wafer 3

The ring waveguides for W3 had polygon shapes instead of a smooth circular shape as can be seen in Figure 5-23. No other measurements were done for this wafer.

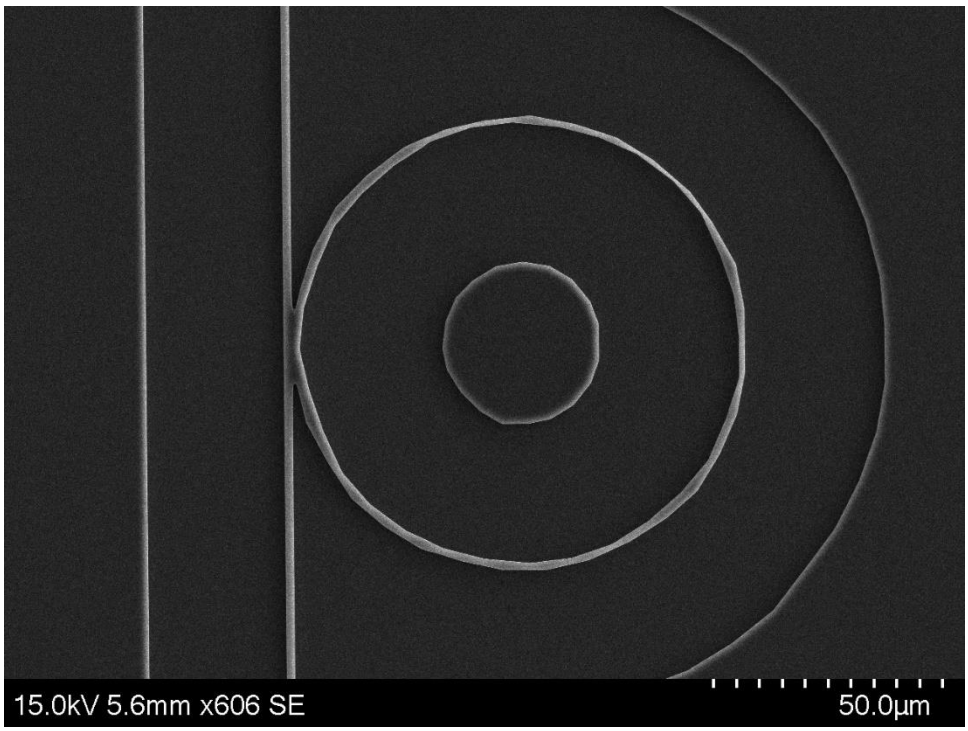

Figure 5-23: The ring waveguides for the ring resonator designs on W3 had uneven polygon shapes instead of a circular shape.

5.2.2.2 Wafer 5

The average height of the $2\ \mu m$ straight waveguides added to the ring resonator mask was $1.25\ \mu m$.

The average height of the ring waveguides was $1.210\ \mu m$, while the height of the straight waveguides was $1.194\ \mu m$.

The ring waveguides for W5 did not suffer from the same issue as W3 as can be seen in Figure 5-24. The gap between the straight waveguide and the ring waveguide was measured with the SEM software as seen in Figure 5-25. In some cases, the gap was not fully developed as seen in Figure 5-26. The same figure shows that the gap between the ring and the straight waveguide becomes less developed for resonators closer to the centre of the wafer. This corresponds to the increase in width for the straight waveguide in the resonators as showed by Figure 5-27.

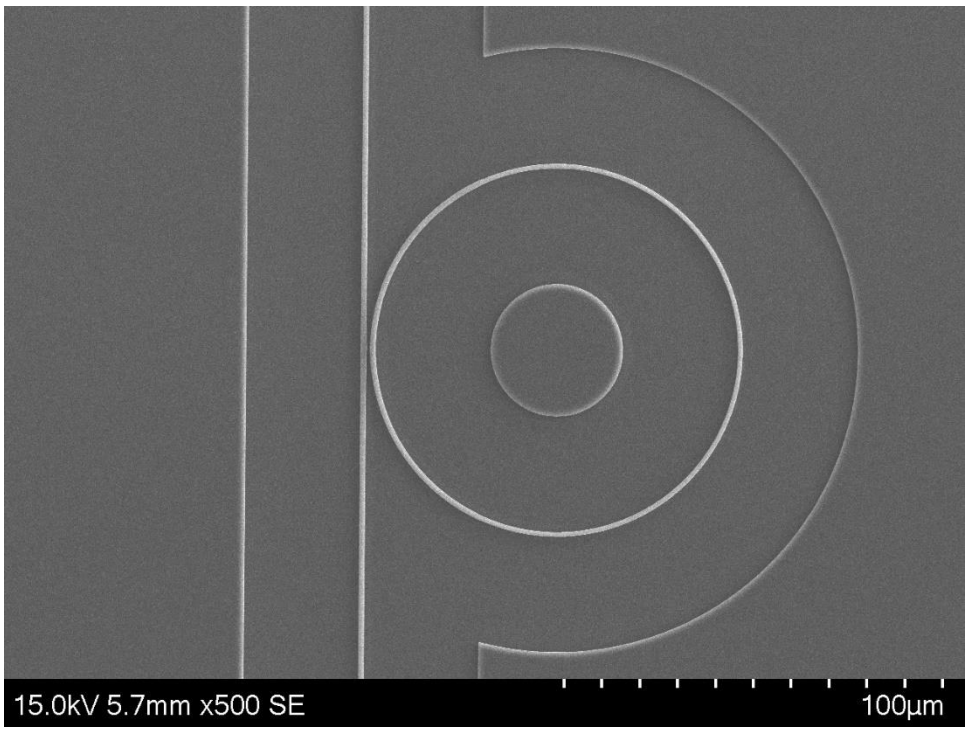

Figure 5-24: Ring resonator on W5 with a radius of 50 *µm.*

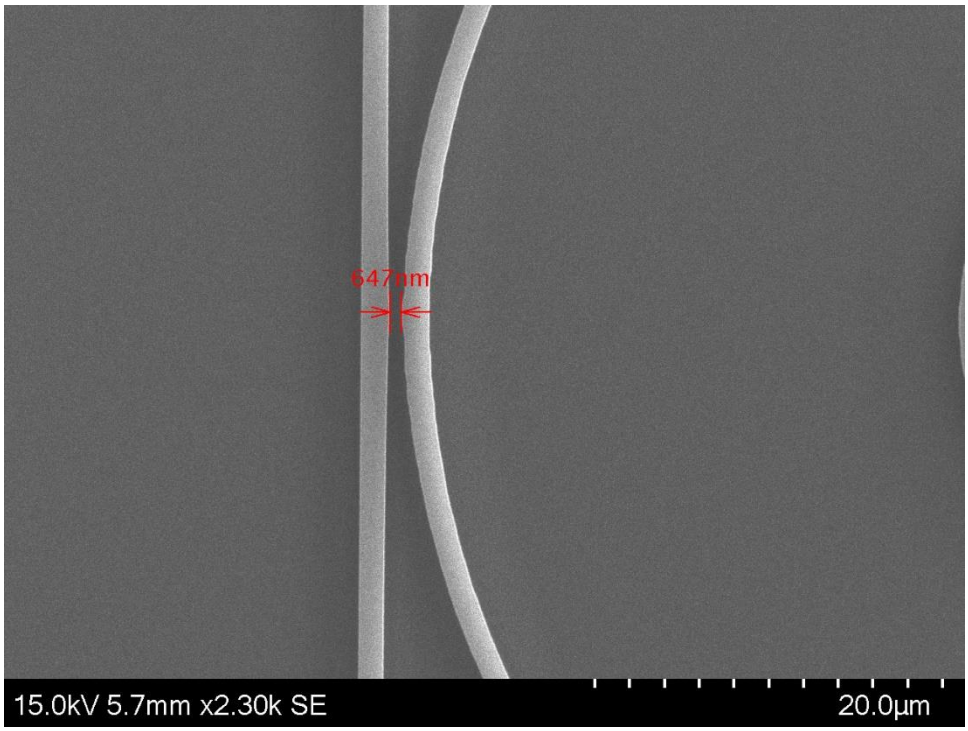

Figure 5-25: Measurement of the gap between the straight and the ring waveguide with the SEM software.

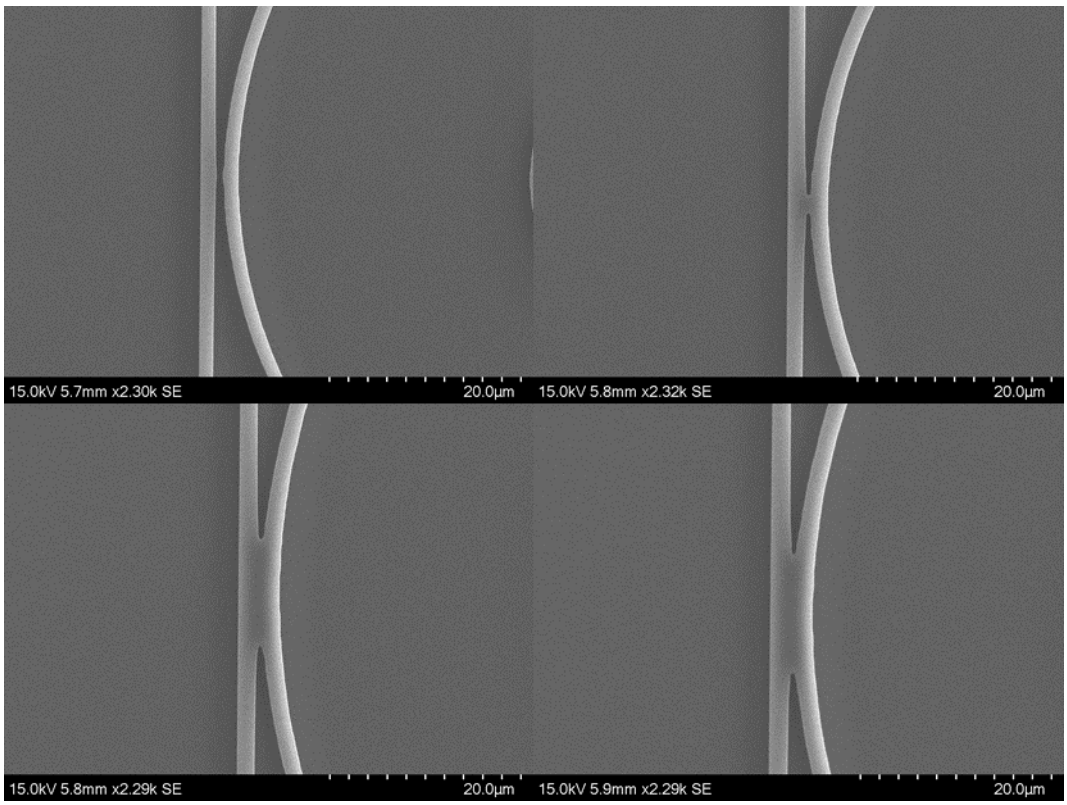

Figure 5-26: From top left down to bottom right, the gap for the first four resonators for row 3. The fourth resonator is closest to the centre of the wafer, while the first is closest to the edge of the wafer.

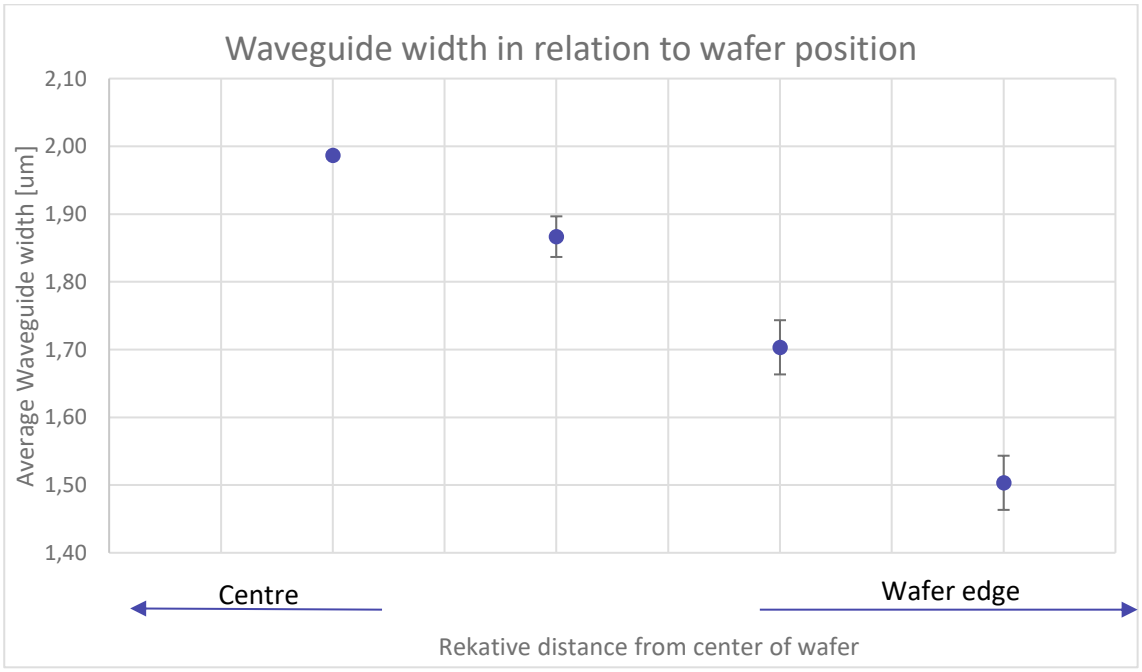

Figure 5-27: The average waveguide width according to the waveguide position on the wafer in relation to the centre and the edge of the wafer.

5.2.3 CROW

5.2.3.1 Wafer 6

Measurements done with the interferometer on CROW design Type 1 showed great variation in height around the ring waveguide as seen in Figure 5-28. The Type 2 CROW design did not suffer from this height variation to the same extent and proceeding measurements were done exclusively on the Type 2.

The overall average waveguide height on W6 was measured to be $1{,}23\ \mu m$. It was observed that, as a general trend, the waveguide on the right-hand side of the gap between two waveguides in the coupling area was taller than the waveguide on the left-hand side (see Figure 5-29). The average height on the right-hand side was $1.291\ \mu m$, while the average height on the left-hand side was $1.201\ \mu m$. Both of these were still taller than the rest of the ring waveguide, the height of which averaged $1.162\ \mu m$.

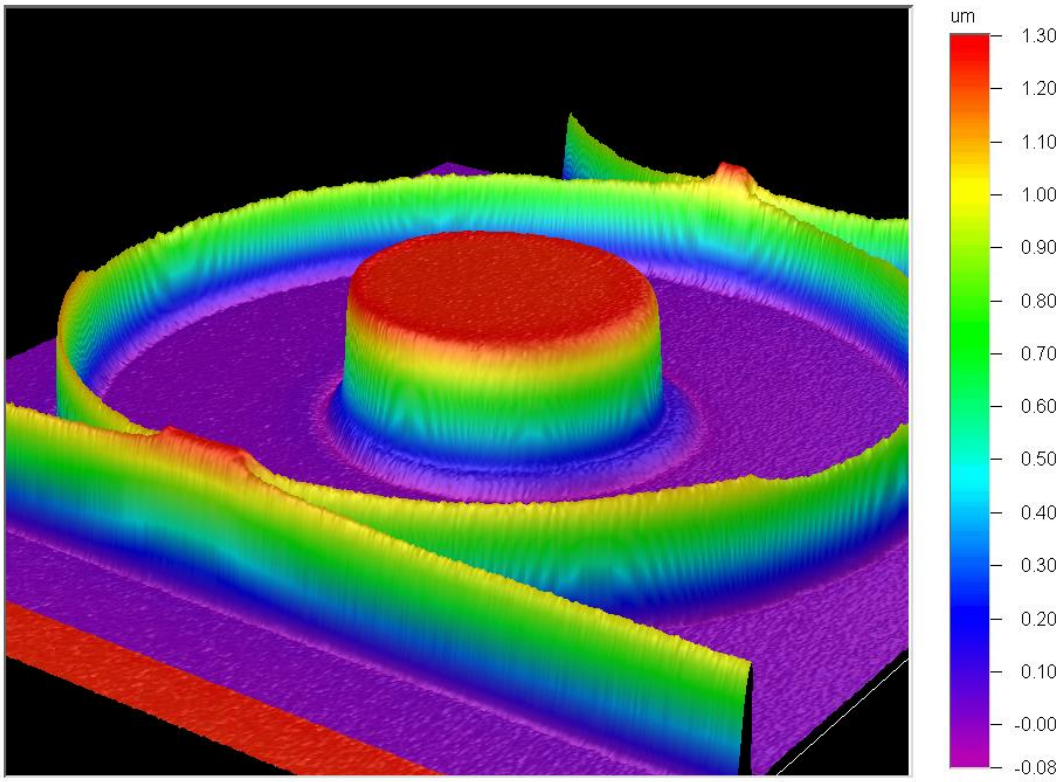

Figure 5-28: 3D representation of the height measurement done with the interferometer for CROW design Type 1.

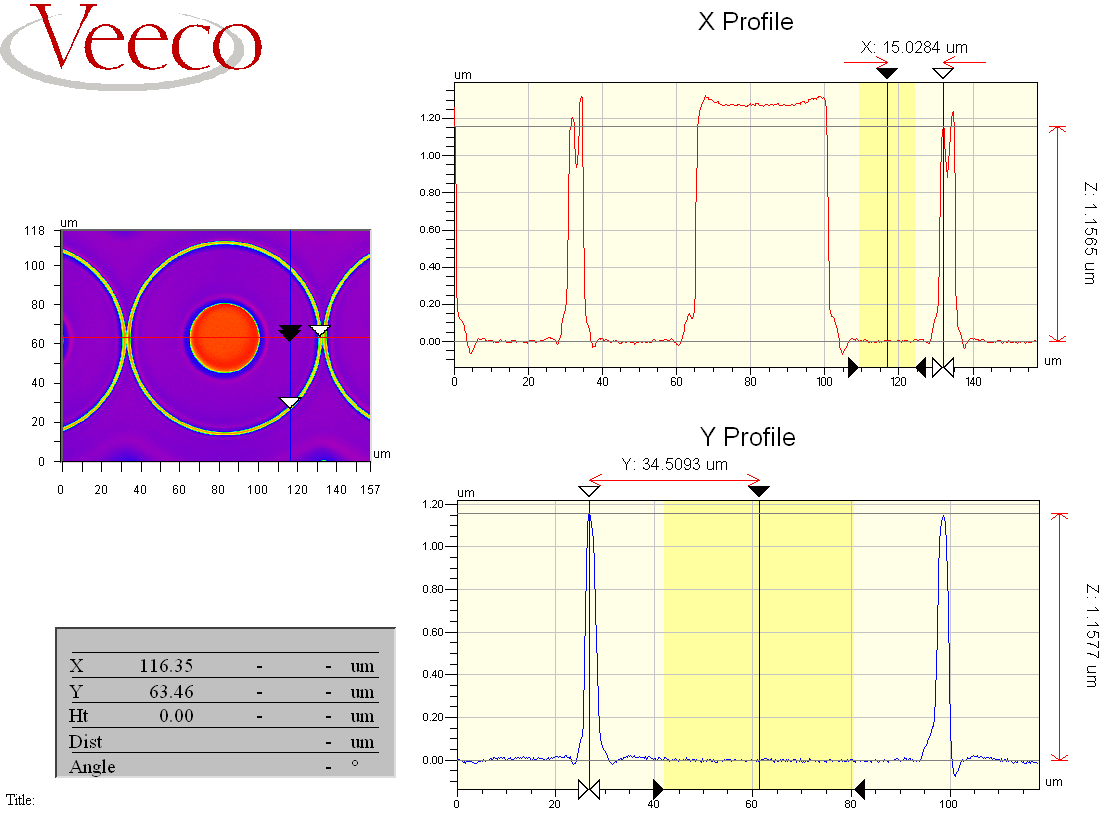

Figure 5-29: Interferometry height measurement of the type 2 CROW design on W6.

The gap between the waveguides in the coupling area was measured with the SEM. The average gap distance for each of the CROW structures can be found in Table 5-10. The frequency of non-developed gaps between ring waveguides was higher for the $300\ nm$ mask gap structures than the other two. Furthermore, only one gap between a straight and a ring waveguide was fully developed (see Figure 5-30).

Table 5-10: Average gap measurements for CROW mask design Type 2 for photoresist thickness of $1\ \mu m$.

1 UM CROW TYPE 2			
MASK GAP	Nr 1	Nr 2	Nr 3
300 NM	0.72	0.68	0.63
400 NM	0.82	0.85	0.79
500 NM	0.89	0.94	0.89

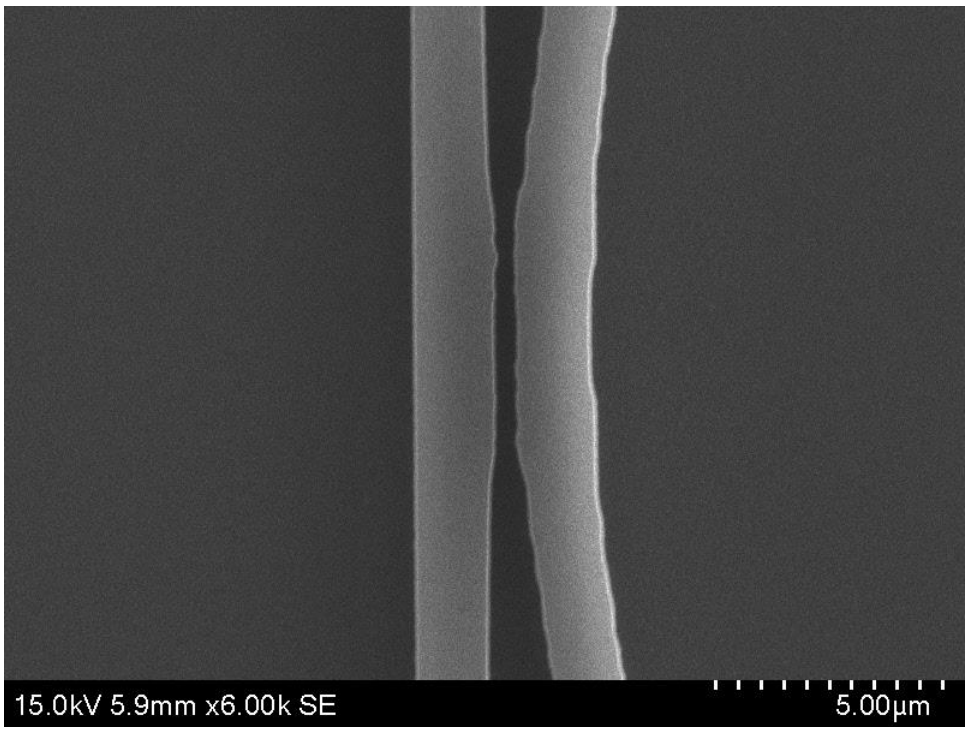

Figure 5-30: The only coupling gap on W6 to be fully developed.

5.2.3.2 Wafer 7

The average height off the Type 2 CROW design waveguides on W7 was $0.527\ \mu m$. In a similar way to W6, the left hand waveguide in the coupling area was higher, at $0.538\ \mu m$, than the right hand waveguide which had an average height of $0.527\ \mu m$, while both of them were taller than remaining the ring waveguide which had an average height of $0.517\ \mu m$.

The ring waveguides did not seem to have a smooth circular profile as can be seen in Figure 5-31, and the gap dimensions measured with the SEM were significantly larger than the mask dimensions. The average gap distance for each CROW structure is recorded in Table 5-11.

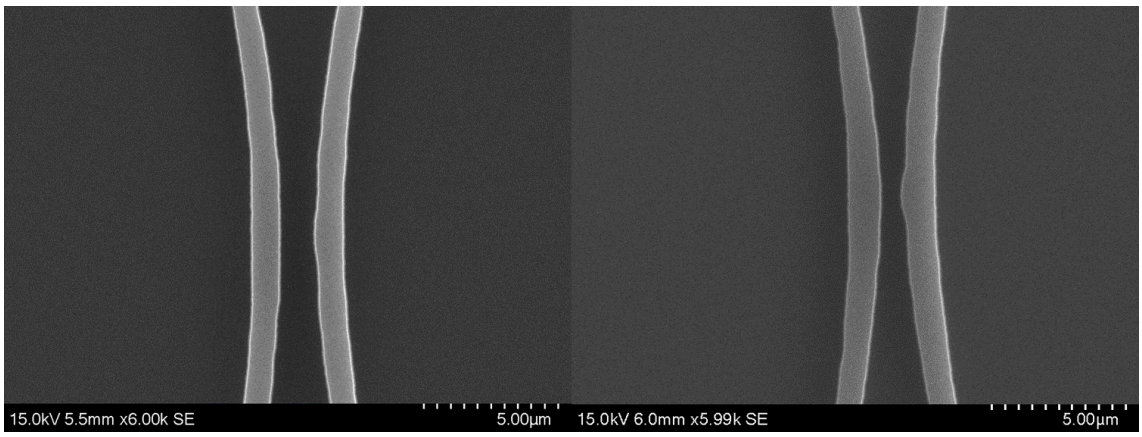

Figure 5-31: The gap between the ring waveguides in the left images is larger than the width of the waveguides themselves. The waveguides in the right image has an uneven waveguide profile.

Table 5-11: Average gap measurements for the CROW mask design Type 2 with a photoresist thickness of 250 *nm.*

	CROW TYPE 2		
MASK GAP	Nr 1	Nr 2	Nr 3
300 NM	0.91	0.80	0.83
400 NM	1.12	1.07	1.07
500 NM	1.26	1.25	1.23

6 Discussion

6.1 Simulation and computation

There is bound to be some discrepancy between the MATLAB results and the COMSOL results, considering that the MATLAB script operates with a zero-boundary condition, while the COMSOL simulation operates with PEC by default and due to the different numerical methods used. Although it is possible to apply a zero-boundary condition in COMSOL, it only impacts either the electric field or the magnetic field which is a limitation of COMSOL 5.5.

At most, the difference in n_{eff} between MATLAB and COMSOL for the step-index fibre for P. Lüsse et al. was 4.13×10^{-6}. The analytical solution given by P. Lüsse et al corresponds exactly with COMSOL result. Both the MATLAB and the COMSOL mode plot seem to indicate a TE like mode. However, the mode plots do not seem to correspond with Figure 4 in the paper by P. Lüsse et al [16]. Although, P. Lüsse et al. write about the fundamental mode, it seems that they have plotted a higher order mode.

However, for the rib waveguide analysis the x and y components of the electric field and magnetic field seems to mirror each other in Figure 5-4 and Figure 5-5. The COMSOL mode plot appears to correspond exactly with Figure 6 in [16]. Unfortunately, P. Lüsse et al. do not show any other field than the H_x and H_y field. This could indicate that there is a mistake in the MATLAB script, but nothing has been debugged yet.

This reoccurs for some of the waveguide cross-section, where the MATLAB and COMSOL computations give n_{eff} that are very close in value but the two have different seem to have different transverse field.

The MATLAB mode plot in Figure 5-9, is the x-polarisation of the fundamental mode. Plotting the mode for the second n_{eff} gives an identical result to Figure 3. (c) in the paper by Z. Zhu and T. G. Brown [14].

The MATLAB scripts are limited in that they define the cross-section of the waveguide with the computation mesh. This transforms any curved interface to a step approximation. To implement the improved index averaging proposed by S. Guo et al, it would be necessary to also apply a sub-cell mesh to define the geometry [13]. This would come at the cost of increased computation time.

Nevertheless, the results from the PML computations are in the same order of magnitude to the results from COMSOL and S. Guo et al. [13].

There was an inevitable discrepancy between the computed results given here and the results from S. Guo et al., since Guo et al. only state the thickness and the mode power of the conductivity profile for their PML, but do not give any value for the reflection coefficient. The reflection coefficient used was $R = 10^{-8}$ which is the same as that used by C. -P. Yu and H.-C. Chang [15].

To date, using COMSOL Multiphysics 5.5, there is still not an option to mirror the mesh from one part of the geometry to the next. This means that the mesh in COMSOL is not entirely cylindrically symmetrical which could explain the mode profiles in Figure 5-13 and Figure 5-10.

COMSOL released COMSOL Multiphysics 5.6 on November 11. 2020, which came with an application file (Application ID: 88741) that simulates the PCF in S. Guo et al. [17], [18].

The ring resonator transmittance plot (see Figure 5-16) show resonance wavelengths that correspond closely to the theoretical resonance wavelengths. There is a slight shift that is probably due to the change in n_{eff} as a result of the change in wavelengths. The 2D simulation however is limited in that 3D structures that might carry a single mode, does not translate well to the 2D slab.

6.2 Fabrication

First of all, the SOI wafer used in this fabrication is not suitable for the fabrication of optical waveguides. The wafer was chosen among a selection of the SOI wafers the IMST lab at USN and was the option closest to photonic wafers. None of the waveguides fabricated would be single mode waveguide.

The destruction of the $1\ \mu m$ straight waveguide on W2 is the reason no other wafer had the photoresist removed with the ultrasound bath.

When exporting the mask from L-Edit to a GDSII file format, the mask is created based on the manufacturing grid and not the grid used to design the mask. Wafers W1 – W4 had a manufacturing gird of $250\ nm$. This manufacturing grid is the reason for the step shapes in the taper on W1 and W4 and the polygon shape of the ring waveguides on W3.

The manufacturing grid was changed to $1\ nm$ for W5 and was kept constant for the remaining wafers. Thus, the mask was no longer the resolution limiting factor of the fabrication process.

It is not unexpected that only the $500\ nm$ coupling gap on W5 was fully developed. This is because W5 was exposed with the medium spot size resolution which is $450\ nm$. For this reason, new exposure recipes had to be created on the PicoMaster for W6 and W7. Nevertheless, Figure 5-27 shows that the waveguides closer to the edge were overdeveloped, since the waveguides closer to the centre were almost exactly $2\ \mu m$ wide. This is due to movement of the wafer in the developer solution. In the development of W5, the wafer was gently rotated back and forth around its central axis. This means that structures close to the wafer edge had a higher speed than the structures closer to the centre. The higher speed resulted in a higher flow of developer and so a higher developing reaction. For wafer W6 and W7, the wafers were gently moved in such a way that the flow of the developer solution would be uniform across the wafer surface.

In conjunction with Figure 5-26, the two figures indicate an issue with aspect-ratio. Meaning that the larger areas, in this case the clearance areas, are quickly developed. While smaller areas, in this case the coupling gap, take longer to develop. This results in an overdevelopment of the larger areas when the small areas are fully developed, and an underdevelopment of the smaller areas when the larger areas are fully developed. Considering that the ratio between the clearance areas and the coupling gap is 100, it is possible that no degree of process optimisation would resolve this issue.

The high aspect-ratio issue is also reflected in the measurement of W6 and W7. The measured gap distances are at least twice the size of the mask gap, yet on W6 only one of the gaps between the straight and the ring waveguide was fully developed. It is also worth noting the unevenness of the ring waveguide in Figure 5-31. As stated in 2.1.3, the dominant loss in ring waveguides is scattering due to sidewall roughness. The CROWs fabricated on W6 and W7 would be able to provide low loss and so are unsuitable for gyroscope sensing. Due to the overdevelopment, it is not possible to say whether the unevenness is a result of the overdevelopment or step approximation by the PicoMaster during exposure.

The decision to use a thinner photoresist was due to the depth of focus of the high-resolution spot size. Nevertheless, the thickness of the photoresist does not seem to have

influenced the lateral dimensions of the waveguides. The thickness of the photoresist does however affect the ease with which the coupling gap is developed and may have contributed to only one of the coupling gaps between the straight and the ring waveguide being developed. Nevertheless, the overdevelopment of the $250\ nm$ photoresist is so severe, that it is impossible to make any conclusion. Any future fabrication with the diluted photoresist should start with an even shorter development time to prevent any overdevelopment.

The thickness of the $250\ nm$ photoresist was only measured once after one test fabrication and no other dilution combinations were tried. It was assumed that the thickness would remain consistent across the wafer surface and between wafers. This is however, not guaranteed.

For any fabrication process optimisation, it would be necessary to verify this assumption and investigate other photoresist dilutions.

The height and gap dimensions were not measured for the Type 1 CROW design. As seen in Figure 5-28, the uniformity of the waveguide height is influenced by the etch depth and the etch depth is proportional to the etching area. The quality of the waveguide is dependent of the waveguide height and so the type 1 design was determined unsuitable for future designs.

To summarise, the fabrication process presented in this thesis provides more a proof of concept and requires several adjustments and optimisations before it can be considered a viable method of waveguide fabrication.

6.3 Sources of error

The waveguide width was measured in the SEM between the high contrast lines (see Figure 5-22). This might, however, be a systematic error if the actual waveguide width is the entire region. Nevertheless, it would not counter the case for the waveguides being overdeveloped.

Yet another source of error is the VSI interferometer. As seen with W4, the interferometer was unable to measure the hight of the waveguides, leading to the assumption that they had been destroyed during the removal of the photoresist. Inspection with the SEM proved this to be false. The reason the waveguide did not register on the interferometer, is because the waveguide width was smaller than the

optical resolution of the interferometer, which according to the interferometer manual is $535\ nm$ [19].

6.4 Future work

Future work on the VMS-ZB MATLAB script should include debugging and investigating of the script to determine the source of the mode plot variations. It would also be beneficial to develop the script further to allow for PEC and PMC boundary conditions.
Any future work on the VMS-PML script should include the addition of a sub-cell mesh to improve the index averaging, which should improve the accuracy of the computed imaginary part of n_{eff}. The script should also be tested on other waveguide cross-section to verify test its accuracy and limitations.
Improving the COMSOL Mode solver application would include the option for the user to add a PML boundary, define mesh size, and other complex waveguide cross-sections like MOF and PFC.
Future work with the ring resonator would be to simulate a CROW with a rotating mesh to investigate the simulation possibility of CROW gryoscopes.

The photoresist chosen for this fabrication was S1813 positive photoresist. The two main factors contributing to this choice were the ease with which the photoresist could be removed after dry-etching, and lesser fumes as opposed to the alternative negative photoresist. However, future work should investigate the waveguide fabrication with negative photoresist.
Firstly, there would not be the need to create a clearance area around the waveguide.
Secondly, there would be less chance of issues with the high aspect-ratio between the largest and smallest features. However, the potential effect of over-development to fully develop the coupling gap should still be looked at with the negative photoresist.
Thirdly, since the laser only exposes the waveguide, it might be possible to achieve high quality waveguides using the medium spot size resolution with a small step size.
Further testing of the $50/50$ photoresist solution and running a dilution series could prove useful in the optimisation of the fabrication process.

It might also be worth looking into a different fabrication process. A. Griffith et al. were able to fabricate high quality factor silicon ring resonators using a thermal oxidation process [20].

As an example, if one must use positive photoresist, lift-off process is on possible method to improve the waveguide fabrication.

1. Coat the wafer with a sacrificial layer of positive photoresist.
2. Expose the photoresist with the laser writer with a mask in the shape of the waveguide.
3. Develop the photoresist to create a cavity in the shape of the waveguide.
4. Deposit amorphous silicon $(a - Si)$ using chemical vapour deposition (CVD) or another deposition method.
5. Remove the sacrificial layer of photoresist and the unwanted $a - Si$ to reveal the waveguides.

The fabrication of optical waveguides with a lift-off process is not new and might yield higher quality waveguides.

Another method would be to fabricate single-mode waveguide using in house grown layer structure of low refractive index contrast such as SiO_2/SiN with a Plasma Enhanced Chemical vapour deposition (PECVD) reactor. This will relax the dimension requirements for the waveguide and ease the fabrication. Unfortunately, those capabilities are not in the IMST lab at USN.

Future work should also include testing the power transmission and the frequency response of the ring resonator and the CROW. This will require coupling between the laser source, the waveguide and the power meter. Since the dicing saw produces sever chipping along the cutting edge (see Figure 5-18), the coupling between waveguide and fibre would have to be achieved either by replacing the taper with a grating coupler or acquiring some other means to dice the wafer, such as scribing.

7 Conclusion

In conclusion, the simulation tools proposed in this thesis in terms of the COMSOL Mode Solver application and the three MATLAB scripts produce results that are comparable with results from the literature and each other. The MATLAB scripts and the COMSOL Mode Solver application have the advantage that they can be run without the user having to purchase or learn to use COMSOL. The MATLAB scripts, however, can compute more complex waveguide cross-sections.

The fabrication carried indicates the possibility of fabricating waveguide structures with maskless photolithography. Nevertheless, the subtractive process using S1813 positive photoresist is unsuitable for the fabrication of ring resonators and CORWs due to the problem of high aspect-ratio. It is unlikely that any process optimization will resolve this issue. The subtractive process with the use of negative photoresist or an additive process with positive photoresist should be investigated in the future. Due to the severe cases of overdevelopment, it is not possible to conclude whether the maskless photolithographic fabrication will yield structures with ring loss suitable for CROW gyroscopes.

The work that forms the basis of this thesis can contribution to the development of a micro optical gyroscope by providing computing models for determining the propagation mode, propagation constant and leakage loss.

References

[1] J. Nayak and P. D. Pinnoji, 'Advanced optical gyroscopes', in *Workshop on Recent Advances in Photonics (WRAP)*, New Delhi, Dec. 2013, pp. 1–2, doi: 10.1109/WRAP.2013.6917717.

[2] V. M. N. Passaro, A. Cuccovillo, L. Vaiani, M. De Carlo, and C. E. Campanella, 'Gyroscope Technology and Applications: A Review in the Industrial Perspective', *Sensors*, vol. 17, no. 10, p. 2284, Oct. 2017, doi: 10.3390/s17102284.

[3] H. C. Lefèvre, *The Fiber-Optic Gyroscope*. Norwood, Massachusetts, USA: Artech House, INC, 1993.

[4] C. Sorrentino, J. R. E. Toland, and C. P. Search, 'Ultra-sensitive chip scale Sagnac gyroscope based on periodically modulated coupling of a coupled resonator optical waveguide', *Opt. Express*, vol. 20, no. 1, p. 354, Jan. 2012, doi: 10.1364/OE.20.000354.

[5] C. Ciminelli, C. E. Campanella, F. Dell'Olio, C. M. Campanella, and M. N. Armenise, 'Multiple ring resonators in optical gyroscopes', in *2012 14th International Conference on Transparent Optical Networks (ICTON)*, Coventry, United Kingdom, Jul. 2012, pp. 1–4, doi: 10.1109/ICTON.2012.6253759.

[6] D. Kalantarov and C. P. Search, 'Effect of resonator losses on the sensitivity of coupled resonator optical waveguide gyroscopes', *Opt. Lett.*, vol. 39, no. 4, p. 985, Feb. 2014, doi: 10.1364/OL.39.000985.

[7] O. Solgaard, *Photonic Microsystems: Micro and Nanotechnology Applied to Optical Devices and Systems*, 1st edition. Springer Science & Business Media, LLC, 2010.

[8] C. R. Pollock, *Fundamentals of optoelectronics*. Chicago: Irwin, 1995.

[9] A. K. Ghatak and K. Thyagarajan, *An introduction to fiber optics*. Cambridge; New York: Cambridge University Press, 1998.

[10] D. G. Rabus, Ed., 'Ring Resonators: Theory and Modeling', in *Integrated Ring Resonators: The Compendium*, Berlin, Heidelberg: Springer, 2007, pp. 3–40.

[11] 'Optical Ring Resonator Notch Filter', *COMSOL*. https://www.comsol.no/model/optical-ring-resonator-notch-filter-22221 (accessed Nov. 14, 2020).

[12] J.-P. Berenger, 'A perfectly matched layer for the absorption of electromagnetic waves', *J. Comput. Phys.*, vol. 114, no. 2, pp. 185–200, Oct. 1994, doi: 10.1006/jcph.1994.1159.

[13] S. Guo, F. Wu, S. Albin, H. Tai, and R. S. Rogowski, 'Loss and dispersion analysis of microstructured fibers by finite-difference method', *Opt. Express*, vol. 12, no. 15, p. 3341, 2004, doi: 10.1364/OPEX.12.003341.

[14] Z. Zhu and T. Brown, 'Full-vectorial finite-difference analysis of microstructured optical fibers', *Opt. Express*, vol. 10, no. 17, p. 853, Aug. 2002, doi: 10.1364/OE.10.000853.

[15] C.-P. Yu and H.-C. Chang, 'Yee-mesh-based finite difference eigenmode solver with PML absorbing boundary conditions for optical waveguides and photonic crystal fibers', *Opt. Express*, vol. 12, no. 25, p. 6165, 2004, doi: 10.1364/OPEX.12.006165.

[16] P. Lusse, P. Stuwe, J. Schule, and H.-G. Unger, 'Analysis of vectorial mode fields in optical waveguides by a new finite difference method', *J. Light. Technol.*, vol. 12, no. 3, pp. 487–494, Mar. 1994, doi: 10.1109/50.285331.

[17] 'Release History'. https://www.comsol.com/release-history (accessed Nov. 17, 2020).

[18] ‘Leaky Modes in a Microstructured Optical Fiber’. COMSOL, Accessed: Nov. 17, 2020. [Online]. Available: https://www.comsol.com/model/download/840941/models.woptics.microstructured_optical_fiber.pdf.
[19] Veeco Instruments Inc., ‘Wyko NT9100 Setup and Operation Guide’. 2008, Accessed: Nov. 18, 2020. [Online]. Available: http://utw10193.utweb.utexas.edu/InstrumentManuals/Wyko%20NT9100%20Setup%20and%20Operation%20Guide.pdf.
[20] A. Griffith, J. Cardenas, and C. B. Poitras, ‘High quality factor and high confinement silicon resonators using etchless process’, p. 5, 2012.

List of tables and charts

Appendix 1: Fabrication process of waveguides on SOI.

The following is a general description of the fabrication steps used to fabricate waveguides on SOI wafers. The wafers used was a $100mm$ BSOI OKMETIC (100) wafer with a Si substrate thickness of $525\ \mu m$, a SiO_2 layer $1\ \mu m$ thick, with a top Si layer 4 μm thick.

1. The wafer was cleaned using an Acetone, Isopropanol and DI water wash over a beaker to remove any organic contaminants. The wafer is then blow dried with Nitrogen (N) gas.
2. Once the wafer is dry it was soft baked on a hotplate at $115\ °C$ for $5\ min$ to evaporate any residual moisture.
3. Positive photoresist was then spin coated onto the wafer using a SPIN150 wafer spinner with a 2 step spin program seen in Table 0-1. The amount of photoresist poured onto the wafer before staring the spin program was roughly $2\ cm$ in diameter.

Table 0-1: Spin coating program parameters.

STEP	SPEED	TIME	ACCELERATION
1	500 rpm	5 s	800 rpm/s
2	2500 rpm	30 s	800 rpm/s

4. The wafers were pre-exposure heated for $90\ s$ on a hotplate at $115\ °C$.
5. Photoresist exposure was done using the PicoMaster 150PM laser writer. the wafer dimension, recipe, step size and focus must be chosen and calibrated before the exposure can start.
6. After exposure, the photoresist was immersion developed in MF-319 photoresist developer for $20\ s$. The wafers were inspected under an optical microscope to ensure that all the areas were fully developed.
7. The wafers were then dry etched using a four-cycle Bosch process in a PlasmaPro 100 Estrelas DRIE machine. The etching parameters can be found in Table 0-2.
8. The remaining photoresist was then exposed with UV light before being removed with AID wash and plasma cleaning with the Alpha Plasma AL 18.

Table 0-2: Process parameters for the Bosch DRIE process.

Wafer	ICP power (D)	ICP power (B)	ICP power (E)	HF power (B) W	Pressure (D) (mT)	Pressure (B)	Pressure (E) (mT)	C4F8 (D) (sccm)	C4F8 (B) (sccm)	C4F8 (E) (sccm)	SF6 (D) (sccm)	SF6 (B)	SF6 (E) (sccm)	Time (D) (Sec)	Time (B) (Sec)	Time (E) (Sec)	Cycle (Sec)	Stage cycles	Stage time (min)	He Torr/sccm	Table Temp (ºC)	I_spacer (A)	Total Cycles	Process time (min)
W1	1750	1750	3000	70	50	25	60	200	10	10	10	200	600	0,75	0,65	1	2,4	4	0,16	10	20	0	2	2,17
W2	1750	1750	3000	70	50	25	60	200	10	10	10	200	600	0,75	0,65	1	2,4	4	0,16	10	20	0	2	2,17
W3	1750	1750	3000	70	50	25	60	200	10	10	10	200	600	0,75	0,65	1	2,4	4	0,16	10	20	0	2	2,17
W4	1750	1750	3000	70	50	25	60	200	10	10	10	200	600	0,75	0,65	1	2,4	4	0,16	10	20	0	2	2,17
W5	1750	1750	3000	70	50	25	60	200	10	10	10	200	600	0,75	0,65	1	2,4	4	0,16	10	20	0	2	2,17
W6	1750	1750	3000	70	50	25	60	200	10	10	10	200	600	0,75	0,65	1	2,4	4	0,16	10	20	0	2	2,17
W7	1750	1750	3000	70	50	25	60	200	10	10	10	200	600	0,75	0,65	1	2,4	2	0,08	10	20	0	2	2,17

Appendix 2: Vectoral mode solver MATLAB script with Zero Boundary Condition

The MATLAB script presented here is the one used for the computation of the MOF presented by Z. Zhu and T. G. Brown. to compute other cross-sections, the relevant parameters and the geometry definition loop has to be modified.

```
%Vectoral mode solver Z. Zhu & T. G. Brown
clear all;
format longg; %To get more than 4 decimal places

%% Structure defining variables
%---Physical definitions---%
lda0 = 1.5e-6; %Wavelength
n_core = 1.45; %Core refractive index
n_clad = 1.42; %Cladding refractive index
n_air = 1; %Refractive index of air holes

%---Geometrical definitions---%
r0 = 2e-6; %Core radius
h = 2*r0; %Core diameter
ra = 2e-6;
Delta = 5e-6;

%---Variable definitions---%
Num = 4; %Number of modes we are looking for
mode_nr = 2; %Mode number to investigate
Dom = 3.5*Delta; %Simulation window
M = 300; %Matrix size

%% Dependent variables and independent definitions
%---Physical variables ---%
k0 = 2*pi/lda0; %Wavenumber

%---Simulation variables---%
dx = Dom/M; %Delta x
dy = dx; %Delta y
x = [0 (Dom*1e+6)]; %X-axis for image plot
y = x; %Y-axis image plot
guess_beta = n_core*k0;  %beta value guess for eigs-
function

%---Matrix Definitions---%
n = ones(M); %Refractive index matrix
ep = ones(M); %Dielectric constant matrix
```

```
%---Counter variables---%
con = 0;
ii=0;

%% Circular structure creation
%---Define the structure in terms of n and ep---%
for ll = 1:M
    for jj = 1:M

    if (((jj-1)*dx-0.5*Dom)^2 + ((ll-1)*dy-0.5*Dom)^2)
<= r0^2
        n(jj,ll) = n_core;
        ep(jj,ll) = n_core^2;

    elseif (((jj-1)*dx - (0.5*Dom))^2 + ((ll-1)*dy -
(0.5*Dom-Delta))^2) <= ra^2
        n(jj,ll) = n_air;
        ep(jj,ll) = n_air^2;

    elseif (((jj-1)*dx - (0.5*Dom))^2 + ((ll-1)*dy -
(0.5*Dom+Delta))^2) <= ra^2
        n(jj,ll) = n_air;
        ep(jj,ll) = n_air^2;

    elseif (((jj-1)*dx -
(0.5*Dom+sqrt(0.75*Delta^2)))^2 + ((ll-1)*dy -
(0.5*Dom+0.5*Delta))^2) <= ra^2
        n(jj,ll) = n_air;
        ep(jj,ll) = n_air^2;

    elseif (((jj-1)*dx -
(0.5*Dom+sqrt(0.75*Delta^2)))^2 + ((ll-1)*dy -
(0.5*Dom-0.5*Delta))^2) <= ra^2
        n(jj,ll) = n_air;
        ep(jj,ll) = n_air^2;

     elseif (((jj-1)*dx - (0.5*Dom-
sqrt(0.75*Delta^2)))^2 + ((ll-1)*dy -
(0.5*Dom+0.5*Delta))^2) <= ra^2
        n(jj,ll) = n_air;
        ep(jj,ll) = n_air^2;

    elseif (((jj-1)*dx - (0.5*Dom-
sqrt(0.75*Delta^2)))^2 + ((ll-1)*dy - (0.5*Dom-
0.5*Delta))^2) <= ra^2
        n(jj,ll) = n_air;
        ep(jj,ll) = n_air^2;
```

```
    else
        n(jj,ll)= n_clad;
        ep(jj,ll) = n_clad^2;
    end

    end
end

%% Eigenvalue Problem calculation
%---Defining the U, V and I matricies---%
one = ones(M^2,1);
Mat1 = spdiags([-one one], 0:1, M^2, M^2);
Mat2 = spdiags([-one one], [0, M], M^2, M^2);

Ux = 1/dx *Mat1;
Uy = 1/dy *Mat2;
Vx = 1/dx *(-Mat1.');
Vy = 1/dx *(-Mat2.');

I = speye(M^2); %The identity matrix

%---Allocating Matrix space---%
ep_rx = sparse(M^2);
ep_ry = sparse(M^2);
ep_rz = sparse(M^2);

%---Defining the value for ep_r---%
for ll = 1:M
    for jj = 1:M
        con = con+1;

        if ll>1
            ep_rx(con,con) = 0.5*(ep(jj,ll) +
ep(jj,ll-1));
        else
            ep_rx(con,con) = ep(jj,ll);
        end

        if jj>1
            ep_ry(con,con) = (ep(jj,ll) + ep(jj-
1,ll))/2;
        else
            ep_ry(con,con) = ep(jj,ll);
        end

        if (ll>1 && jj>1)
           ep_rz(con,con) = 0.25*(ep(jj,ll) + ep(jj-
1,ll-1) + ep(jj,ll-1) + ep(jj-1,ll));
        else
```

```
            ep_rz(con,con) = ep(jj,ll);
        end

    end
end

Eprx = spdiags(diag(ep_rx).^(-1),0,M^2,M^2); %The
inverse of ep_rx to be used in calculaions;
Epry = spdiags(diag(ep_ry).^(-1),0,M^2,M^2); %The
inverse of ep_ry to be used in calculaions;
Eprz = spdiags(diag(ep_rz).^(-1),0,M^2,M^2); %The
inverse of ep_rz to be used in calculaions;

%---Calculation of the sub matricies of the Q matrix--
-%
Qxx = -k0^(-2)*Vx*Uy*Ux*Eprz*Vy + (ep_ry + k0^(-
2)*Vx*Ux)*(k0^2*I + Uy*Eprz*Vy);
Qyy = -k0^(-2)*Vy*Ux*Uy*Eprz*Vx + (ep_rx + k0^(-
2)*Vy*Uy)*(k0^2*I + Ux*Eprz*Vx);
Qxy = -(ep_ry + k0^(-2)*Vx*Ux)*Uy*Eprz*Vx + k0^(-
2)*Vx*Uy*(k0^2*I + Ux*Eprz*Vx);
Qyx = -(ep_rx + k0^(-2)*Vy*Uy)*Ux*Eprz*Vy + k0^(-
2)*Vy*Ux*(k0^2*I + Uy*Eprz*Vy);

Q = [Qxx, Qxy; Qyx, Qyy]; %The Q matrix

%---Calculations using the Q matrix---%
[Q_V,Q_D,Q_flags] = eigs(Q,Num,guess_beta^2); %Finds
the number of modes defined earlier

Q_beta = sqrt(diag(Q_D));  %The eigenvalues are on the
diagonal of the Q_D matrix
Q_neff = Q_beta/k0; %Calculate the effective index for
the modes

%% Field calculations
Hxx = Q_V(1:M^2,mode_nr);
Hyy = Q_V(M^2+1:2*M^2,mode_nr);

tmp1= k0^2*I+(Ux*Epry*Vx+Uy*Eprx*Vy);
tmp2=1i*Q_beta(mode_nr)*(Ux*Epry*Hxx+Uy*Eprx*Hyy);

Hzz = tmp1\tmp2;

Exx = 1i/k0*Eprx*(-1i*Q_beta(mode_nr)*Hyy+Vy*Hzz);
Eyy = 1i/k0*Epry*(1i*Q_beta(mode_nr)*Hxx-Vx*Hzz);
Ezz = 1i/k0*Eprz*(-Vy*Hxx+Vx*Hyy);

Hx=zeros(M);
```

```
Hy=Hx;
Hz=Hx;
Ex=Hx;
Ey=Hx;
Ez=Hx;

for ll=1:M
   for jj=1:M

      Hx(jj,ll) = Hxx(jj+ii,1);

      Hy(jj,ll) = Hyy(jj+ii,1);

      Hz(jj,ll) = Hzz(jj+ii,1);

      Ex(jj,ll) = Exx(jj+ii,1);

      Ey(jj,ll)=Eyy(jj+ii,1);

      Ez(jj,ll)=Ezz(jj+ii,1);

   end
 ii=ii+M;
end


%% Plotting the structural cross-section
figure(1)
imagesc(x,y,real(n));
axis image;
colormap gray;
c = colorbar;
c.Label.String = 'Refractive index';
set(gca,'YDir','normal');
xlabel('\mum');
ylabel('\mum');

%% Printing the effective index
disp(Q_neff(mode_nr)); %Display the first effective
index in command window

%% Plotting the field distribution
figure(2);
tiledlayout(3,2);

nexttile(1)
imagesc(x,y,abs(Hy)); xlabel('x-axis \mum');
ylabel('y-axis \mum'); title('Hy');
set(gca,'YDir','normal');
```

```
axis image;
colorbar;

nexttile(3)
imagesc(x,y,abs(Hx)); xlabel('x-axis \mum');
ylabel('y-axis \mum'); title('Hx');
set(gca,'YDir','normal');
axis image;
colorbar;

nexttile(5)
imagesc(x,y,abs(Hz)); xlabel('x-axis \mum');
ylabel('y-axis \mum'); title('Hz');
set(gca,'YDir','normal');
axis image;
colorbar;

nexttile(2)
imagesc(y,x,abs(Ey)); xlabel('x-axis \mum');ylabel('y-
axis \mum'); title('Ey');
set(gca,'YDir','normal');
axis image;
colorbar;

nexttile(4)
imagesc(x,y,abs(Ex)); xlabel('x-axis \mum');ylabel('y-
axis \mum'); title('Ex');
set(gca,'YDir','normal');
axis image;
colorbar;

nexttile(6)
imagesc(x,y,abs(Ez)); xlabel('x-axis \mum');ylabel('y-
axis \mum'); title('Ez');
set(gca,'YDir','normal');
axis image;
colorbar;
```

Appendix 3: Vectoral Mode Solver MATLAB script with PML

The MATLAB script presented here is the one used for the computation of the MOF presented by S. Guo et al. To compute other cross-sections, the relevant parameters and the geometry definition loop has to be modified.

```
%Vectoral mode solver with PML
clear all;
format longg; %To get more than 4 decimal places

%% Structure defining variables
%---Physical definitions---%
lda0 = 1.45e-6; %Wavelength
n_clad = 1.45; %Cladding refractive index
n_air = 1; %Refractive index of air holes

%---Geometrical definitions---%
ra = 2.5e-6;
Delta = 6.75e-6;

%---Variable definitions---%
Num = 4; %Number of modes we are looking for
mode_nr = 1; %Mode number to investigate
Dom = 3*Delta; %Simulation window
PML_d = 0.1*Dom; %Thickness of PML layer
m = 2; %Conductivity power-mode
R = 1e-8; %Reflection coefficient
Dom_PML = Dom + 2*PML_d; %Simulation pluss PML region
M = 300; %Matrix size

%% Dependent variables and independent definitions
%---Physical variables ---%
k0 = 2*pi/lda0; %Wavenumber
ep_0 = 8.8541878128e-12; %Permittivity of free space
mu_0 = 1.25663706212e-6; %Permeability of free space
omega = sqrt(k0^2 /(ep_0*mu_0)); %Angular frequency
c = 299792458; %Speed of light

%---Simulation variables---%
dx = Dom_PML/M; %Delta x
dy = dx; %Delta y
x = [0 (Dom_PML*1e+6)]; %X-axis for image plot
y = x; %Y-axis image plot
```

```
guess_beta = 1.445*k0;  % start guess around which to
search the eigenmode

%-----Matrix Definitions-----%
n = ones(M);
ep = ones(M);
sig = ones(M);

%---Counter variables---%
con = 0;
ii=0;

%% Circular structure creation
%---Define the structure in terms of n and ep---%
for ll = 1:M
    for jj = 1:M


    if (((jj-1)*dx - (0.5*Dom_PML))^2 + ((ll-1)*dy -
(0.5*Dom_PML-Delta))^2) <= ra^2
        n(jj,ll) = n_air;
        ep(jj,ll) = n_air^2;

    elseif (((jj-1)*dx - (0.5*Dom_PML))^2 + ((ll-1)*dy
- (0.5*Dom_PML+Delta))^2) <= ra^2
        n(jj,ll) = n_air;
        ep(jj,ll) = n_air^2;

    elseif (((jj-1)*dx -
(0.5*Dom_PML+sqrt(0.75*Delta^2)))^2 + ((ll-1)*dy -
(0.5*Dom_PML+0.5*Delta))^2) <= ra^2
        n(jj,ll) = n_air;
        ep(jj,ll) = n_air^2;

    elseif (((jj-1)*dx -
(0.5*Dom_PML+sqrt(0.75*Delta^2)))^2 + ((ll-1)*dy -
(0.5*Dom_PML-0.5*Delta))^2) <= ra^2
        n(jj,ll) = n_air;
        ep(jj,ll) = n_air^2;

     elseif (((jj-1)*dx - (0.5*Dom_PML-
sqrt(0.75*Delta^2)))^2 + ((ll-1)*dy -
(0.5*Dom_PML+0.5*Delta))^2) <= ra^2
        n(jj,ll) = n_air;
        ep(jj,ll) = n_air^2;

    elseif (((jj-1)*dx - (0.5*Dom_PML-
sqrt(0.75*Delta^2)))^2 + ((ll-1)*dy - (0.5*Dom_PML-
0.5*Delta))^2) <= ra^2
```

```
        n(jj,ll) = n_air;
        ep(jj,ll) = n_air^2;

    else
        n(jj,ll)= n_clad;
        ep(jj,ll) = n_clad^2;
    end

    end
end

%% Eigenvalue Problem calculation
%---Defining the U and V matrices---%
one = ones(M^2,1);
Mat1 = spdiags([-one one], 0:1, M^2, M^2);
Mat2 = spdiags([-one one], [0, M], M^2, M^2);

Ux = 1/dx *Mat1;
Uy = 1/dy *Mat2;
Vx = 1/dx *(-Mat1.');
Vy = 1/dx *(-Mat2.');

I = speye(M^2); %The identity matrix

%---Allocating Matrix space---%
mu_r = speye(M^2);

ep_rx_d = sparse(M^2);
ep_ry_d = sparse(M^2);
ep_rz_d = sparse(M^2);

mu_rx_d = sparse(M^2);
mu_ry_d = sparse(M^2);
mu_rz_d = sparse(M^2);

sigx = ones(M);
sigy = ones(M);

sx = sparse(M);
sy = sparse(M);

for ll = 1:M
    for jj = 1:M

    %---Defining SIGMA_y---%
    if  ((jj*dx) <= PML_d)
        sigy(jj,ll) =
((m+1)*ep_0*c*n(jj,ll)*log(1/R)*(PML_d-dx*(jj-
1))^m)/(2*PML_d^(m+1));
```

```
    elseif (((jj-1)*dx) >= (Dom_PML-PML_d))
        sigy(jj,ll) =
((m+1)*ep_0*c*n(jj,ll)*log(1/R)*(dx*jj - (Dom_PML-
PML_d))^m)/(2*PML_d^(m+1));
    else
        sigy(jj,ll) = 0;
    end

    %---Defining SIGMA_x---%
    if ((ll*dy) <= PML_d)
        sigx(jj,ll) =
((m+1)*ep_0*c*n(jj,ll)*log(1/R)*(PML_d-dx*(ll-
1))^m)/(2*PML_d^(m+1));

    elseif (((ll-1)*dy) >= (Dom_PML-PML_d))
        sigx(jj,ll) =
((m+1)*ep_0*c*n(jj,ll)*log(1/R)*(dx*ll - (Dom_PML-
PML_d))^m)/(2*PML_d^(m+1));
    else
        sigx(jj,ll) = 0;
    end

    %---Defining the Sx and Sy values---%
    sx(jj,ll) = 1 - sigx(jj,ll)/(1j*omega*ep_0);
    sy(jj,ll) = 1 - sigy(jj,ll)/(1j*omega*ep_0);

    end
end

%---Defining the value for ep_r---%
for ll = 1:M
    for jj = 1:M
        con = con+1;

        mu_rx_d(con,con) =
(sy(jj,ll)/sx(jj,ll))*mu_r(con,con);
        mu_ry_d(con,con) =
(sx(jj,ll)/sy(jj,ll))*mu_r(con,con);
        mu_rz_d(con,con) =
(sx(jj,ll)*sy(jj,ll))*mu_r(con,con);

        if ll>1
            ep_rx_d(con,con) =
(sy(jj,ll)/sx(jj,ll))*(0.5*(ep(jj,ll) + ep(jj,ll-1)));
        else
            ep_rx_d(con,con) =
(sy(jj,ll)/sx(jj,ll))*ep(jj,ll);
        end
```

```
        if jj>1
            ep_ry_d(con,con) =
(sx(jj,ll)/sy(jj,ll))*(0.5*(ep(jj,ll) + ep(jj-1,ll)));
        else
            ep_ry_d(con,con) =
(sx(jj,ll)/sy(jj,ll))*ep(jj,ll);
        end

        if (ll>1 && jj>1)
           ep_rz_d(con,con) =
(sx(jj,ll)*sy(jj,ll))*(0.25*(ep(jj,ll) + ep(jj-1,ll-1)
+ ep(jj,ll-1) + ep(jj-1,ll)));
        else
           ep_rz_d(con,con) =
(sx(jj,ll)*sy(jj,ll))*ep(jj,ll);
        end

    end
end

Eprx_d = spdiags((diag(ep_rx_d)).^(-1),0,M^2,M^2);
Epry_d = spdiags((diag(ep_ry_d)).^(-1),0,M^2,M^2);
Eprz_d = spdiags((diag(ep_rz_d)).^(-1),0,M^2,M^2);

Murx_d = spdiags((diag(mu_rx_d)).^(-1),0,M^2,M^2);
Mury_d = spdiags((diag(mu_ry_d)).^(-1),0,M^2,M^2);
Murz_d = spdiags((diag(mu_rz_d)).^(-1),0,M^2,M^2);

%-----Calculation of the sub matricies of the Q
Matrix-----%
Qxx = ep_ry_d*Uy*Eprz_d*Vy + Vx*Murz_d*Ux*mu_rx_d +
k0^2 *ep_ry_d*mu_rx_d + k0^(-2)*Vx*Murz_d*(Ux*Uy-
Uy*Ux)*Eprz_d*Vy;
Qyy = ep_rx_d*Ux*Eprz_d*Vx + Vy*Murz_d*Uy*mu_ry_d +
k0^2 *ep_rx_d*mu_ry_d + k0^(-2)*Vy*Murz_d*(Uy*Ux-
Ux*Uy)*Eprz_d*Vx;
Qxy = -ep_ry_d*Uy*Eprz_d*Vx + Vx*Murz_d*Uy*mu_ry_d +
k0^(-2) *Vx*Murz_d*(Uy*Ux - Ux*Uy)*Eprz_d*Vx;
Qyx = -ep_rx_d*Ux*Eprz_d*Vy + Vy*Murz_d*Ux*mu_rx_d +
k0^(-2) *Vy*Murz_d*(Ux*Uy - Uy*Ux)*Eprz_d*Vy;

Q = [Qxx, Qxy; Qyx, Qyy];

%---Calculations using the Q matrix---%
[Q_V,Q_D,Q_flags] = eigs(Q,Num,guess_beta^2); %Finds
the number of modes defined earlier
```

```
Q_beta = sqrt(diag(Q_D));  %The eigen values are on
the diagonal of the Q_D matrix
Q_neff = Q_beta/k0; %Calculate the effective index for
the modes

%% Field calculations
Hxx = Q_V(1:M^2,mode_nr);
Hyy = Q_V(M^2+1:2*M^2,mode_nr);

tmp1= k0^2*Murz_d+(Ux*Epry_d*Vx+Uy*Eprx_d*Vy);
tmp2=1i*Q_beta(mode_nr)*(Ux*Epry_d*Hxx +
Uy*Eprx_d*Hyy);

Hzz = tmp1\tmp2;

Exx = 1i/k0*Eprx_d*(-1i*Q_beta(mode_nr)*Hyy+Vy*Hzz);
Eyy = 1i/k0*Epry_d*(1i*Q_beta(mode_nr)*Hxx-Vx*Hzz);
Ezz = 1i/k0*Eprz_d*(-Vy*Hxx+Vx*Hyy);

Hx=zeros(M);
Hy=Hx;
Hz=Hx;
Ex=Hx;
Ey=Hx;
Ez=Hx;

for ll=1:M
   for jj=1:M

      Hx(jj,ll) = Hxx(jj+ii,1);

      Hy(jj,ll) = Hyy(jj+ii,1);

      Hz(jj,ll) = Hzz(jj+ii,1);

      Ex(jj,ll) = Exx(jj+ii,1);

      Ey(jj,ll)=Eyy(jj+ii,1);

      Ez(jj,ll)=Ezz(jj+ii,1);

   end
 ii=ii+M;
end

%% Plotting the structural cross-section
figure(1)
imagesc(x,y,real(n));
axis image;
```

```
colormap gray;
c1 = colorbar;
set(gca,'YDir','normal');
c1.Label.String = 'Refractive index';
xlabel('\mum');
ylabel('\mum');

figure(2)
imagesc(real(ep));
axis image;
colormap autumn;
colorbar;

figure(3)
imagesc(sigy);
axis image;
colormap gray;
colorbar;

figure(4)
imagesc(sigx);
axis image;
colormap gray;
colorbar;

%% Printing the effective index
disp(Q_neff(1)); %Display the first effective index in
command window

%% Plotting the field distribution
figure(5);
tiledlayout(3,2);

nexttile(1)
imagesc(x,y,abs(Hy)); xlabel('x-axis \mum');
ylabel('y-axis \mum'); title('Hy');
set(gca,'YDir','normal');
axis image;
colorbar;

nexttile(3)
imagesc(x,y,abs(Hx)); xlabel('x-axis \mum');
ylabel('y-axis \mum'); title('Hx');
set(gca,'YDir','normal');
axis image;
colorbar;

nexttile(5)
```

```
imagesc(x,y,abs(Hz)); xlabel('x-axis \mum');
ylabel('y-axis \mum'); title('Hz');
set(gca,'YDir','normal');
axis image;
colorbar;

nexttile(2)
imagesc(y,x,abs(Ey)); xlabel('x-axis \mum');ylabel('y-
axis \mum'); title('Ey');
set(gca,'YDir','normal');
axis image;
colorbar;

nexttile(4)
imagesc(x,y,abs(Ex)); xlabel('x-axis \mum');ylabel('y-
axis \mum'); title('Ex');
set(gca,'YDir','normal');
axis image;
colorbar;

nexttile(6)
imagesc(x,y,abs(Ez)); xlabel('x-axis \mum');ylabel('y-
axis \mum'); title('Ez');
set(gca,'YDir','normal');
axis image;
colorbar;
```

Appendix 4: Vectoral Mode Solver with Anisotropic Material

```
%Vectoral mode solver Lüsse et al.
clear all;
format longg; %To get more than 4 decimal places

%% Structure defining variables
%---Physical definitions---%
lda0 = 1.3e-6; %Wavelength
n_core = 3.41477; %Core refractive index
n_clad = 3.16589; %Cladding refractive index

%---Geometrical definitions---%
r = 4.5e-6; %Core radius
h = 2*r; %Core diameter

%---Variable definitions---%
Num = 4; %Number of modes we are looking for
mode_nr = 1; %Mode number to investigate
Dom = 20e-6; %Simulation window
M = 300; %Matrix size

%% Dependent variables and independent definitions
%---Physical variables ---%
k0 = 2*pi/lda0; %Wavenumber

%---Simulation variables---%
dx = Dom/M; %Delta x
dy = dx; %Delta y
x = [0 (Dom*1e+6)]; %X-axis for image plot
y = x; %Y-axis image plot
guess_beta = n_core*k0;  %beta value guess for eigs-
function

%---Matrix Definitions---%
n = ones(M); %Refractive index matrix
ep = ones(M); %Dielectric constant matrix
ep_y = ep;
%---Counter variables---%
con = 0;
ii=0;

%% Circular structure creation
%---Define the structure in terms of n and ep---%
for ll = 1:M
    for jj = 1:M
```

```
    if (((jj-1)*dx-0.5*Dom)^2 + ((ll-1)*dy-0.5*Dom)^2)
<= r^2
        n(jj,ll) = n_core;
        ep(jj,ll) = n_core^2;
        ep_y(jj,ll) = ep(jj,ll)*0.98;
    else
        n(jj,ll)= n_clad;
        ep(jj,ll) = n_clad^2;
        ep_y(jj,ll) = ep(jj,ll);
    end

    end
end

%% Eigenvalue Problem calculation
%---Defining the U, V and I matricies---%
one = ones(M^2,1);
Mat1 = spdiags([-one one], 0:1, M^2, M^2);
Mat2 = spdiags([-one one], [0, M], M^2, M^2);

Ux = 1/dx *Mat1;
Uy = 1/dy *Mat2;
Vx = 1/dx *(-Mat1.');
Vy = 1/dx *(-Mat2.');

I = speye(M^2); %The identity matrix

%---Allocating Matrix space---%
ep_rx = sparse(M^2);
ep_ry = sparse(M^2);
ep_rz = sparse(M^2);

%---Defining the value for ep_r---%
for ll = 1:M
    for jj = 1:M
        con = con+1;

        if ll>1
            ep_rx(con,con) = 0.5*(ep(jj,ll) +
ep(jj,ll-1));
        else
            ep_rx(con,con) = ep(jj,ll);
        end

        if jj>1
            ep_ry(con,con) = (ep_y(jj,ll) + ep_y(jj-
1,ll))/2;
        else
```

```
            ep_ry(con,con) = ep_y(jj,ll);
        end

        if (ll>1 && jj>1)
           ep_rz(con,con) = 0.25*(ep(jj,ll) + ep(jj-
1,ll-1) + ep(jj,ll-1) + ep(jj-1,ll));
        else
           ep_rz(con,con) = ep(jj,ll);
        end

    end
end

Eprx = spdiags(diag(ep_rx).^(-1),0,M^2,M^2); %The
inverse of ep_rx to be used in calculaions;
Epry = spdiags(diag(ep_ry).^(-1),0,M^2,M^2); %The
inverse of ep_ry to be used in calculaions;
Eprz = spdiags(diag(ep_rz).^(-1),0,M^2,M^2); %The
inverse of ep_rz to be used in calculaions;

%---Calculation of the sub matricies of the Q matrix--
-%
Qxx = -k0^(-2)*Vx*Uy*Ux*Eprz*Vy + (ep_ry + k0^(-
2)*Vx*Ux)*(k0^2*I + Uy*Eprz*Vy);
Qyy = -k0^(-2)*Vy*Ux*Uy*Eprz*Vx + (ep_rx + k0^(-
2)*Vy*Uy)*(k0^2*I + Ux*Eprz*Vx);
Qxy = -(ep_ry + k0^(-2)*Vx*Ux)*Uy*Eprz*Vx + k0^(-
2)*Vx*Uy*(k0^2*I + Ux*Eprz*Vx);
Qyx = -(ep_rx + k0^(-2)*Vy*Uy)*Ux*Eprz*Vy + k0^(-
2)*Vy*Ux*(k0^2*I + Uy*Eprz*Vy);

Q = [Qxx, Qxy; Qyx, Qyy]; %The Q matrix

%---Calculations using the Q matrix---%
[Q_V,Q_D,Q_flags] = eigs(Q,Num,guess_beta^2); %Finds
the number of modes defined earlier

Q_beta = sqrt(diag(Q_D));  %The eigenvalues are on the
diagonal of the Q_D matrix
Q_neff = Q_beta/k0; %Calculate the effective index for
the modes

%% Field calculations
Hxx = Q_V(1:M^2,mode_nr);
Hyy = Q_V(M^2+1:2*M^2,mode_nr);

tmp1= k0^2*I+(Ux*Epry*Vx+Uy*Eprx*Vy);
tmp2=1i*Q_beta(mode_nr)*(Ux*Epry*Hxx+Uy*Eprx*Hyy);
```

```
Hzz = tmp1\tmp2;

Exx = 1i/k0*Eprx*(-1i*Q_beta(mode_nr)*Hyy+Vy*Hzz);
Eyy = 1i/k0*Epry*(1i*Q_beta(mode_nr)*Hxx-Vx*Hzz);
Ezz = 1i/k0*Eprz*(-Vy*Hxx+Vx*Hyy);

Hx=zeros(M);
Hy=Hx;
Hz=Hx;
Ex=Hx;
Ey=Hx;
Ez=Hx;

for ll=1:M
   for jj=1:M

      Hx(jj,ll) = Hxx(jj+ii,1);

      Hy(jj,ll) = Hyy(jj+ii,1);

      Hz(jj,ll) = Hzz(jj+ii,1);

      Ex(jj,ll) = Exx(jj+ii,1);

      Ey(jj,ll)=Eyy(jj+ii,1);

      Ez(jj,ll)=Ezz(jj+ii,1);

   end
 ii=ii+M;
end

%% Plotting the structural cross-section
figure(1)
imagesc(x,y,real(n));
axis image;
colormap gray;
c = colorbar;
c.Label.String = 'Refractive index';
set(gca,'YDir','normal');
xlabel('\mum');
ylabel('\mum');

%% Printing the effective index
disp(Q_neff(mode_nr)); %Display the first effective
index in command window

%% Plotting the field distribution
figure(2);
```

```
tiledlayout(3,2);

nexttile(1)
imagesc(x,y,abs(Hy)); xlabel('x-axis \mum');
ylabel('y-axis \mum'); title('Hy');
set(gca,'YDir','normal');
axis image;
colorbar;

nexttile(3)
imagesc(x,y,abs(Hx)); xlabel('x-axis \mum');
ylabel('y-axis \mum'); title('Hx');
set(gca,'YDir','normal');
axis image;
colorbar;

nexttile(5)
imagesc(x,y,abs(Hz)); xlabel('x-axis \mum');
ylabel('y-axis \mum'); title('Hz');
set(gca,'YDir','normal');
axis image;
colorbar;

nexttile(2)
imagesc(y,x,abs(Ey)); xlabel('x-axis \mum');ylabel('y-
axis \mum'); title('Ey');
set(gca,'YDir','normal');
axis image;
colorbar;

nexttile(4)
imagesc(x,y,abs(Ex)); xlabel('x-axis \mum');ylabel('y-
axis \mum'); title('Ex');
set(gca,'YDir','normal');
axis image;
colorbar;

nexttile(6)
imagesc(x,y,abs(Ez)); xlabel('x-axis \mum');ylabel('y-
axis \mum'); title('Ez');
set(gca,'YDir','normal');
axis image;
colorbar;
```